Negative thermal expansion of cold-rolled Ti-Nb over a wide temperature range

A thesis submitted for the degree of Doctor of Philosophy at

Faculty of Science and Engineering

University of Nottingham Malaysia

by

Daniel Lai Kuok Zheng

Under the supervision of

Dr. Lim Chin Seong

Dr. How Ho Cheng

Prof. Sun Zhenzhong

Dr. Wang Haoliang

2024

Acknowledgements

This journey was arduous and tumultuous, especially with the events of COVID-19, remote cooperative work with DGUT, and much interpersonal turmoil. I would like to thank my family, especially my mom for supporting me. It has not been easy as I watch you grow old but I'm still here studying and regretting my choices. Much thanks to Dr. Lim Chin Seong for giving me this opportunity and for the help you have given within your constraints. Thanks to Dr. How Ho Cheng for the lengthy discussions into the evenings and giving advice as best you could to deal with sticky interpersonal situations. Thank you to Ms. Asyiqin from the Faculty of Science and Engineering for patiently dealing with my drawn-out processes as I struggle with motivation. Thank you to the academics and staff that have taught me skills, techniques, and knowledge along the way. It was truly enjoyable to learn things I had not known before. Thanks to Elaine for muscling through the first year together. Thank you to Lim Ziyian for being an older brother I never had. To my past and future selves, sorry. Thank you to DGUT for the collaboration and guidance under the DGUT-UoN Joint Doctoral Training Programme Scholarship.

In soil rich, a seed was sown,
Amidst whispered vows, in silence known.
Nurtured with promises, never to fade,
Yet beneath false care, its essence betrayed.

Each petal unfurls, a delicate veneer,
Yet unseen shadows loom, drawing near.
Harvested blooms, petals softly torn,
A tender heart aches, silently worn.

Though sunlight bathes, its form so frail,
Promised sustenance turns hollow, pale.
In whispered breezes, a melancholy sigh,
A flower's dreams wither, though it tries.

Through veils of doubt, it struggles on,
In the quiet dusk, its resilience drawn.
For in its essence, a quiet grace,
A beauty enduring, despite the embrace.

Abstract

Anisotropic negative thermal expansion (NTE) of martensitic β-isomorphous Ti-alloys has been discovered to be one of the largest in magnitude among other NTE materials. Exhibition of macroscale NTE was shown to be achievable through texturing, but studies reporting on this behaviour have been conservative and have only reported within the purely martensitic region. Studies have not yet revealed the effects of phase transformation and thermomechanical property changes on the textured material when heated above the martensitic region. This work aims to study the NTE thermal stability, phase transformation sequence, and resulting mechanical properties of a cold-rolled Ti-22Nb (at.%) elevated to temperatures outside the purely martensitic region. The evolution of macroscale thermal expansion of cold-rolled Ti-22Nb was uncovered by thermal cycling to 150, 250, 350, 450, 550 °C. The magnitude of contraction along the rolling direction increased with temperature until a maximum contraction was achieved at 320 °C. Expansion was observed beyond that temperature and the specimen retained NTE at 150-250 °C, zero thermal expansion at 350 °C, and positive thermal expansion at 450-550 °C. Long-term NTE thermal stability of cold-rolled Ti-22Nb was investigated through isothermally aging the specimen at 150, 250 °C for 10, 100, 1000 hours. In both cases, the NTE of the sample decreased with duration. Diffusional rejection of Nb was behind the minimal loss of NTE after 1000h at 150 °C, while zero thermal expansion was achieved after 1000h at 250 °C. An unusual destruction and precipitation of ω phase was detected while aging at 150 °C. The phase transformations leading to the deterioration of NTE when heating to 350-550 °C was studied and sequenced according to the occurring temperatures. The non-linear nature of macroscale NTE was reasoned to stem from direct translation of the lattice NTE. Diffusional rejection of Nb was the main mechanism leading to loss of NTE and eventually leading to a duplex α+β microstructure. An unusual occurrence of the same diffusion occurring at staggered temperatures was observed was reasoned to be due to the cold-work nature of the specimen.

Symbols and abbreviations

List of symbols

Symbol	Explanation	Unit
a_α, c_α	Lattice parameters of the hexagonal α Ti phase	Å
$a_{\alpha''}$, $b_{\alpha''}$, $c_{\alpha''}$	Lattice parameters of the orthorhombic α'' Ti phase	Å
a_β	Lattice parameters of the bcc β Ti phase	Å
a_M, b_M, c_M	Lattice parameters of martensite	Å
a_A	Lattice parameter of austenite	Å
a_ω, c_ω	Lattice parameters of the hexagonal ω Ti phase	Å
A_s, A_f	Austenite start and finish temperature	°C or K
M_s, M_f	Martensite start and finish temperature	°C or K
$T_{transus}$	Transus temperature between two phases	°C or K
$[Mo]_{eq}$	Molybdenum equivalent	-
T_0	Temperature where the Gibbs free enthalpy of two phases are equal	°C or K
ε_M^i	Martensitic transformation strain	-
CV_n (n=1, 2, …)	Martensite variant n	-
G	Gibbs free enthalpy	J/mol
H	Enthalpy	J/mol
T	Temperature	°C or K
s	Entropy	J/mol
U	Internal energy	J/mol
P	Pressure	Pa
V	Volume	m^3
C_P	Specific heat capacity	J/kg.K
T^M	Melting temperature	°C or K
$\Delta G_{nucleation}$	Gibbs free enthalpy required for nucleation	J/mol
ΔG_{mix}	Latent heat of mixing	J/mol
Δs_{mix}	Entropy of mixing	J/mol
ΔH_{mix}	Enthalpy of mixing	J/mol
μ_A^β	Chemical potential of element A in phase β	-
X_n	Annotated composition n	at.% or wt.%
G^0	Point where free enthalpy of two phases are equal	J/mol
D	Diffusion coefficient	m^2/s
D_0	Diffusion frequency factor or diffusivity	m^2/s
R	Universal gas constant	J/K.mol
E	Young's modulus	GPa
ε	Strain	-

$\varepsilon_0, \varepsilon_T$	Strain at 0 °C and strain at specific temperature T	-
$K\alpha_1$, $K\alpha_2$	Kα wavelength used in XRD	nm
$[uvw], (hkl)$	Specific crystallographic direction and plane	-
$\langle uvw \rangle, \{hkl\}$	Family of crystallographically equivalent directions and planes	-
α_{TE}	Average thermal expansion between 0-100 °C	ppm/°C
Bo	Bond order	-
Md	Energy level of the d-orbital in metal atoms	-

List of abbreviations

Abbreviation	Explanation
α"	Orthorhombic α" phase
α'	Hexagonal α' phase
α''_{iso}	α" phase formed under isothermal conditions
α''_{rich}, α''_{lean}	α" phase consisting of a rich or lean Nb content relative to the reference state
β	Body centered cubic β phase
ω	Hexagonal ω
ω_{ath}, ω_{iso}	Athermally and isothermally formed ω
hcp	Hexagonal close packed
bcc	Body centered cubic
TE	Thermal expansion
NTE	Negative thermal expansion
PTE	Positive thermal expansion
ZTE	Zero thermal expansion
CTE	Coefficient of thermal expansion
RD, TD, ND	Rolling, transverse and normal direction
SIM	Stress induced martensite
TMA	Thermomechanical analysis
XRD	X-ray diffraction
EDX	Electron dispersive X-ray
SEM	Scanning electron microscopy
(HR)TEM	(High resolution) Transmission electron microscopy
BF, DF	Bright field, dark field
HAADF	High angular annular dark field
SAED	Selective area electron diffraction
FFT/IFFT	Fourier transform/Inverse Fourier transform
EBSD	Electron backscatter diffraction
EDM	Electron discharge machining
RT	Room temperature
CR	Cold rolled
WQ	Water quenched
CSRO	Chemical short-range order

List of figures

Figure	Caption	Page
Fig. 2.1	Classification of phase diagrams within the binary Ti alloy system. Examples of actual phase diagrams taken for (a) Ti-Zr [34] (b) Ti-V [35] (c) Ti-Cr [36] (d) Ti-Al [37] (e) Ti-N [38]	11
Fig. 2.2	The Ti-Nb system phase diagram by Zhang er al. including stable phases (solid lines) and metastable phases (dotted lines) [39]	12
Fig. 2.3	Schematic diagram of obtainable metastable phases upon quenching from the single β phase at various β stabilizer content in a Ti-Nb system. Adapted from [13, 29] .	15
Fig. 2.4	Unit cells of (a) hcp-α (b) orthorhombic α" (c) bcc-β, with their lattice parameters illustrated.	18
Fig. 2.5	Micrograph examples of (a) lathe martensite [63] . (b-c) Variants of martensite forming in a lathe morphology [64] . (d-e) Martensite forming in the plate morphology and the twin variants forming within the plates [65] .	19
Fig. 2.6	(a) The β structure before forming ω, with an ABCABC… sequence along $\langle 111 \rangle_\beta$. The coloured planes are to collapse to form ω. (b) The collapsed B and C planes to form $(0002)_\omega$. (c) The β structure showing the β unit cell and the $(111)_\beta$ plane that is parallel to the ω basal plane. (d) The ω structure viewed parallel to $[1\bar{2}10]_\omega$ as seen in most TEM micrographs.	21
Fig. 2.7	HAADF-STEM images of a β matrix alongside a ω precipitate. (b-d) Illustrations of the ω phase plane collapse formation process. (e) Another HAADF-STEM micrograph showing a further collapsed ω structure.	22
Fig. 2.8	(a) Illustrations of the variation of internal energy, H, and free enthalpy, G, with temperature. (b) The free enthalpy curve of two competing phases in a system, where the phase of lowest enthalpy forms.	24
Fig. 2.9	The variation of free enthalpy, entropy, enthalpy, and volume in a system of (a-c) a system exhibiting first order transformation, (d-f) a second order transformation. Adapted from [72].	25
Fig. 2.10	Illustration of a free enthalpy curve when accounting for nucleation energy required for precipitation of a new phase. The example shown is of a liquid-solid transition but is generally applicable for any nucleation process.	26
Fig. 2.11	The free enthalpy vs composition curve of a system with two competing phases. (a) The system is at inequilibrium with two phases of unequal chemical free energy and do not share a common tangent. (b) The composition of the two phases change to balance the chemical free energy and share a common tangent to achieve equilibrium.	28

Fig. 2.12	Classification of first order phase transformations adapted from Banerjee [13].	29
Fig. 2.13	(a) A system with a composition at the G0 point where the free enthalpies of both phases are equal. However, this does not mean that no separation of phases will occur, since the chemical free energies are not equal. (b) The system quenched to a temperature where the composition lies to the right of the G0 point and the system lowers its free energy through solute partitioning. (c) The system quenched to a temperature where the composition lies to the left of the G0 point and displacive transformation is available from point 1 to 2.	32
Fig. 2.14	The shear transformation undergone by (a) a cubic unit cell towards (b) a tetragonal unit cell then towards an (c) orthorhombic unit cell. The orthorhombic unit cell then undergoes a shuffle of atoms in the $(002)_{\alpha"}$ plane.	33
Fig. 2.15	(a) The free enthalpy curve showing the nucleation of martensite from austenite. (b) A schematic example of a calorimetric experimental result measuring the As, Af, Ms, Mf temperatures of the martensitic transformation and martensitic reversion.	34
Fig. 2.16	The stress-strain curve of a Ti alloy undergoing stress induced martensitic (SIM) transformation. Region I is elastic deformation. Region II is the start of SIM transformation. Region III is continued SIM transformation and strain hardening. Region IV is yield plastic deformation.	35
Fig. 2.17	Diffusivity of Nb in Ti at various Nb compositions. Adapted from [42] .	36
Fig. 2.18	(a) A schematic example of molar free enthalpy curves of a two-phase material with a spinodal region. (b) Compositional fluctuations within the spinodal region allows for lowering of free energy by decomposing into solute rich and lean regions. (c) The precipitation process of a system undergoing spinodal decomposition showing the amplification of initial composition fluctuations in a waveform. (d) Illustration of a system outside the spinodal region unable to amplify compositional fluctuations to lower free energy. (e) The process of nucleation and growth must occur in a system composition outside the spinodal. Distinct precipitates with X1 and X2 are immediately formed and then grows to expand. (f) The illustration of the spinodal free enthalpy curve of α" between α and β in Ti-Nb as suggested by Davis [87] .	38
Fig. 2.19	Compilation of As temperatures of various literatures.	44
Fig. 3.1	Process diagram for the synthesis of cold-rolled Ti-22Nb sample for the use of thermal expansion studies.	46
Fig. 3.2	Workflow of experiments done on Ti-22Nb in this study.	48
Fig. 3.3	In-situ XRD set-up with a heating-cooling stage and vacuum shroud.	53

Fig. 4.1	Wide range XRD scan of Ti-22Nb (a) WQ and (b) CR sample with indexed peaks. (c) The in-situ XRD pattern of the boxed area from (b) heated from 0 °C to 150 °C.	57
Fig. 4.2	(a) Profile fitted full range XRD pattern of CR Ti-22Nb. The inset shows the refined lattice parameters using the available peaks with uncertainty in parentheses. (b) The difference between the position of profile fitted peaks against the position of peaks calculated by refined lattice parameters.	59
Fig. 4.3	Macroscale NTE response along RD of Ti-22Nb alloys of three cold-roll thickness reductions (30%, 50%, 70%).	61
Fig. 4.4	(a) The macroscale thermal expansion response of WQ and CR samples along all directions from 0-100 °C. (b) Macroscale thermal expansion of WQ from 0-550 °C with points deviating from the gradient marked. (c) The NTE response of the CR sample over a wide temperature range from 0-(100n + 50) °C for n = 1-5.	62
Fig. 4.5	(a) EBSD and (b) EDS images of the CR sample showing uniform $\langle 010 \rangle_{\alpha"}$ and fully martensitic composition.	65
Fig. 4.6	DF TEM image of an area captured using two separate ω diffraction spots obtaining different ω morphologies in the CR sample. (a) Acicular and (b) globular ω precipitates are seen.	65
Fig. 5.1	(a) TMA measurements along RD for 150 °C aged samples and CR. (b) The calculated average CTE along RD between 0-100 °C of each sample.	68
Fig. 5.2	(a-c) Wide range XRD scans of 150 °C aged samples at room temperature. (d-f) Enlarged area showing in-situ diffraction of peaks $(020)_{\alpha"}$, $(002)_{\alpha"}$ and $(111)_{\alpha"}$ from 0 °C to 150 °C. (g) Lattice NTE response of $(020)_{\alpha"}$ of all three aging conditions and CR, then visualized in (h). Stacked room temperature ex-situ XRD of (i) $(020)_{\alpha"}$, (j) $(002)_{\alpha"}$ and $(111)_{\alpha"}$ peaks together with CR.	70
Fig. 5.3	DF	71
Fig. 5.4	DF TEM of ω captured using the circled SAED diffraction spot in the inset after aging for 10h at 150 °C. ω is seen (a) concentrated in a lath form similar to lath seen in Fig. 4.6 and (b) dispersed in the surrounding matrix.	72
Fig. 5.5	(a) DF TEM of ω and the captured SAED pattern in the inset showing uniformly dispersed particles. (b) HRTEM of said area and the FFT inset that matches the SAED pattern captured. Several areas of clear lattice fringes are circled in white and two are selected to be enlarged in (c) and (d). Intensity profiles of the lattice fringes were measured along the dashed lines in (e) and their respective directions labelled with respect to the ω and β lattice shown in (f).	73
Fig. 5.6	(a) DF TEM image of ω imaged using the circled SAED diffraction spot in the inset. (b) A peculiar SAED pattern captured in only certain areas of the	75

	sample showing extra circular diffraction streaks marked with red arrows. The two ω variants are circled and labelled to for discussion. (c) HRTEM image of with circled areas of clear lattice fringes and the respective FFT shown in (d). Inverse FFT was performed using the extra circular diffraction streaks and shown in (e). A selected area is enlarged and presented in (f) to show the lattice spacings measured.	
Fig. 5.7	(a) BF TEM image of an area in the 150 °C 1000h aged sample containing fine precipitates. Fig. 5.6b shows the SAED pattern of this area. These precipitates are related to the thin diffraction streak marked in red arrows in (b) between the ω and α" spots. (c-d) HRTEM was performed in the area and clear disc-like precipitates similar to the BF image were found. (e) Inverse FFT was performed by selecting the diffraction streaks marked in (c) and a disc-like shape similar in width and length was found. (f) Enlarged area of the disc-like precipitate to measure lattice spacings identical to those in Fig. 5.5c and Fig. 5.6f.	76
Fig. 5.8	(a) Tensile test and (b) Vicker's hardness and Young's modulus of the 150 °C aged and CR samples.	77
Fig. 5.9	(a) TMA measurements along RD for 250 °C aged samples and CR. (b) The calculated average CTE along RD between 0-100 °C of each sample.	78
Fig. 5.10	Wide range XRD scans of 250 °C aged samples. (d-f) Enlarged area showing in-situ diffraction of peaks $(020)_{\alpha"}$, $(002)_{\alpha"}$ and $(111)_{\alpha"}$ from 0 °C to 250 °C. (g) Lattice NTE response of $(020)_{\alpha"}$ of all three aging conditions and CR, then visualized in (h). Stacked room temperature ex-situ XRD of (i) $(020)_{\alpha"}$, (j) $(002)_{\alpha"}$ and $(111)_{\alpha"}$ peaks together with CR.	79
Fig. 5.11	DF TEM images of ω in samples aged at 250 °C for (a) 10h, (b) 100h, (c) 1000h and their respective SAED patterns (d-f).	81
Fig. 5.12	(a) DF TEM of α" and the (b) captured SAED pattern in the sample aged at 250 °C for 100h. Short basket-weave acicular structures were seen.	82
Fig. 5.13	(a) DF TEM of α" in the sample aged at 250 °C for 1000h and the captured (b) SAED pattern. (c) HAADF-STEM image of the sample showing a wide-range basket-weave acicular structure and (d) EDS mode under HAADF-STEM that shows zones of lean Nb correlating to the acicular structures.	83
Fig. 5.14	(a) Tensile test response and (b) Vicker's hardness and Young's modulus of the 250 °C aged samples.	83
Fig. 5.15	(a) The calculated positions of peaks $(020)_{\alpha"}$, $(002)_{\alpha"}$ and $(111)_{\alpha"}$ in Ti-Nb from 19 at.% to 22 at.% Nb.	86
Fig. 5.16	(a) The evolution of peaks $(020)_{\alpha"}$, $(002)_{\alpha"}$ and $(111)_{\alpha"}$ between 36.5° and 39.5° from the CR state at 250 °C throughout aging for 10, 100, 1000h.	89
Fig. 5.17	The $\overline{Bo} - \overline{Md}$ figure by Morinaga [147] and adapted by Bignon [149] shows the starting point of pure Ti, and their position on the figure with	92

	increasing β-isomorphous stabilizer concentration.	
Fig. 5.18	Evolution of the ω phase throughout aging at 150 °C from the CR state.	95
Fig. 5.19	Comparison of the (a) Young's modulus and (b) specific modulus against average CTE of aged Ti-22Nb alloys against commercial alloys.	97
Fig. 6.1	(a) Macroscale thermal strain of CR Ti-22Nb along RD heated to maximum cycle temperatures of 350 °C, 450 °C, 550 °C and cooled down at temperature change rate of 3 °C/min. (b) Macroscale thermal strain of the thermal cycled samples. Individual thermal strain and thermal stability within eight thermal cycles heated to 300 °C of (c) 350HT and (d) 450HT. (e) Comparison of thermal strain along RD and TD of a CR Ti-22Nb.	100
Fig. 6.2	In-situ XRD of CR Ti-22Nb heated from 0-550 °C from 2θ between 34-42.5°. The intensity is represented with the colour bar.	102
Fig. 6.3	Comparison of CR Ti-22Nb at (a) 350 °C, (b) 450 °C, (c) 550 °C and each respective HT state at RT. (d) Lattice thermal expansion of $(020)_{\alpha''}$ in 350HT, 450HT and 550HT compared with the 250 °C aged states from Chapter 5.	104
Fig. 6.4	SEM micrographs of CR Ti-22Nb heated to (a) 250 °C, (b) 300 °C, (c) 350 °C and cooled to RT.	105
Fig. 6.5	(a) Enlarged micrograph showing precipitates in 350HT state. (b) Phase map of 350HT. (c) EBSD grain orientation map. EDX showing (d) majority element distribution, (e) Ti distribution, (f) Nb distribution.	106
Fig. 6.6	STEM micrograph of 450HT showing (a) intersecting acicular structures and (b) parallel structures and grain boundary precipitates. EDX was performed on the same area as (b) and found the (c) Ti distribution to be fairly even while (d) Nb distribution shows a lean area corresponding to the grain boundary precipitates. (e) DF TEM of the 450HT sample using the selected ω diffraction spot in (f) showed two morphologies, ellipsoidal and globular side-by-side.	107
Fig. 6.7	SEM micrograph of 550HT sample (a) at a lower magnification showing grain boundary precipitates, intersecting acicular precipitates marked by white arrow, and parallel precipitates marked by red arrow. (b) Magnified area of an area with parallel precipitates.	109
Fig. 6.8	(a) Tensile properties, (b) Young's modulus and Vickers hardness of the thermally cycled samples.	109
Fig. 6.9	The atomic volume of α/α', α" and β with respect to Nb concentration adopted from [178]	111
Fig. 6.10	Heating thermal strain and second derivative of the thermal strain up to 350 °C for (a) the RD and (b) TD directions.	113

Fig. 6.11	Overlapped comparison showing the similarity between $(020)_{\alpha''}$ lattice strain and thermal strain along RD in CR sample from 0-300 °C.	113
Fig. 6.12	Ex-situ XRD pattern of 450HT sample at RT with profile fitted peaks with calculated α, α" and β peak positions.	115
Fig. 6.13	In-situ XRD showing the onset of formation of dual α peaks between 500-550 °C.	116
Fig. 6.14	In-situ XRD of the heating of CR sample from 0-550 °C, overlayed with sequence of phase transformations from Table 6.2.	117
Fig. 6.15	Thermal strain along RD of a CR Ti-22Nb heated to 350 °C with the dotted line depicting the thermal strain during cooling without diffusion.	119
Fig. 6.16	(a) Wide angle ex-situ XRD pattern of a CR Ti-22Nb with individual profile fitted peaks. The middle figure below shows the trend line of the profile fitted FWHM of every individual peak. The bottom figure shows the Williamson-Hall plot in an attempt to calculate the residual stress within the sample. (b), (c), (d) shows the magnified areas in (a) with their calculated FWHM attached below.	123
Fig. 6.17	(a) The Young's modulus and average CTE of WQ, CR and heat-treated Ti-22Nb samples in comparison to other commonly used commercial alloys adapted from [163]. (b) The specific modulus was calculated by using the average densities of commercial alloys from [164].	127

List of tables

Table	Caption	Page
Table 2.1	Crystallographic information of Ti and Nb in the Ti-Nb system	16
Table 2.2	Compilation of lattice thermal expansion of Ti-Nb based alloys.	41
Table 2.3	Compilation of lattice thermal expansion of the equilibrium phases in Ti systems.	43
Table 3.1	Dimensions of samples used in this study as sectioned by EDM.	50
Table 4.1	Measured values of CR samples after undergoing single cycle heating and cooling to various temperatures.	64
Table 5.1	Measured comparison of lattice scale and macroscale NTE for the 150 °C aged states.	87
Table 5.2	Summary of the average macro NTE, lattice NTE and TEM observations of the aged samples in this chapter.	96
Table 6.1	Table of A_s and A_f temperatures from literature for solution treated, water quenched Ti-Nb alloys around 22 at. %.	110
Table 6.2	Phase transformation sequence and occuring temperatures during heating in a CR Ti-22Nb sample.	120

Table of Contents

Acknowledgements i

Abstract ii

List of symbols iii

List of abbreviations v

List of figures vi

List of tables xii

Table of Contents xiii

1. Introduction 1

1.1. Motivation and objectives 1

1.2. Rationale 3

1.3. Outline 4

2. Literature review 6

2.1. Recent developments in NTE materials and where Ti-Nb stands 6

2.2. Classification of phase diagrams of Ti-X alloys 8

2.3. Phase diagram of Ti-Nb system 12

2.4. Crystallography of phases within the Ti-Nb system 15

2.4.1. Equilibrium phases 15

2.4.2. Martensitic phase 16

2.4.3. ω phase 19

2.5. Phase transformations within the Ti-Nb system 22

2.5.1. Thermodynamics of phase transformations 22
2.5.2. Phase transformation mechanisms 29
2.5.3. Martensitic formation 31
2.5.4. Stress induced α" phase 34
2.5.5. Diffusion in the Ti-Nb system/ Spinodal decomposition 35
2.6. Thermal expansion of phases within Ti-Nb 39
2.6.1. Thermal expansion of α" phase 39
2.6.2. Thermal expansion of α, β and ω phase 42
2.7. Thermal stability of α" phase 43
3. Experimental details 46
3.1. Experimental aim and procedures 46
3.2. Material synthesis 47
3.3. Experiment workflow 48
3.4. Isothermal aging 49
3.5. Thermomechanical Analysis (TMA) 50
3.6. Tensile testing 51
3.7. Young's modulus characterization 51
3.8. Vickers Hardness 51
3.9. Microstructural characterization 52
3.9.1. SEM/EBSD 52
3.9.2. TEM 52
3.10. Ex-situ, in-situ XRD 53
4. Behaviour of macroscale NTE of cold-rolled Ti-22Nb alloy through heating 55

4.1. Introduction 55
4.2. Results 55
4.2.1. X-ray diffraction 55
4.2.2. Analysis method of XRD patterns 57
4.2.3. In-situ XRD 59
4.2.4. Macroscale thermal expansion 60
4.2.1. Microstructural characterization 65
4.3. Summary 66
5. NTE thermal stability and mechanical behaviour of cold-rolled Ti-22Nb under long-term aging 67
5.1. Introduction 67
5.2. Results 67
5.2.1. Aging at 150°C 68
5.2.2. Aging at 250°C 78
5.3. Discussion 84
5.3.1. Lattice and macroscale thermal expansion after 150 °C aging 84
5.3.2. Precipitation of α''_{iso} during 250 °C aging 88
5.3.3. Lattice and macroscale thermal expansion after 250 °C aging 89
5.3.4. Microstructural and mechanical behaviour after aging at 150 °C 90
5.3.5. Microstructural and mechanical behaviour after aging at 250 °C 95
5.3.6. NTE performance of aged CR Ti-22Nb alloys 97
5.4. Summary 97
6. Evolution of macroscale NTE in a cold-rolled Ti-Nb alloy through thermal cycling 99

6.1. Introduction 99

6.2. Results 100

6.2.1. Macroscale thermal expansion 100

6.2.2. X-ray diffraction 102

6.2.3. Microstructural characterization. 105

6.2.4. Mechanical strength 109

6.3. Discussion 110

6.3.1. Phase transformation sequence in a cold-rolled Ti-22Nb alloy 110

6.3.2. Increased reverse martensitic transformation temperature range 120

6.3.3. Staggered diffusional process 123

6.3.4. Mechanical properties of heat-treated Ti-22Nb 125

6.3.5. Performance of heat treated cold-rolled Ti-22Nb as a low thermal expansion material 126

6.4. Summary 128

7. Conclusions and outlook 129

7.1. Conclusions 129

7.2. Outlook 130

8. Reference 133

1. Introduction

1.1. Motivation and objectives

Recent progression of innovations and technologies have progressively moved toward higher power consumption while simultaneously trying to minimize space consumption. As such, the thermal expansion of materials become a prominent property to consider when the generated thermal stresses of higher power consumption could jeopardize the precision needed for intricate parts to work as intended.

For decades, titanium has been known for its unique functional properties such as superelasticity and shape memory effect, but recent investigations on the thermal expansion of β-isomorphous Ti alloys have also revealed large anisotropic thermal expansion of martensite unit cell. Among the principal directions of the martensitic unit cell, the largest NTE reported was as large as -93.1 ppm/°C, while another principal direction exhibited an even larger PTE of up to 124.9 ppm/°C [1, 2]. Ti-Nb alloys possess the potential to be in the category of "colossal" CTE materials where lattice thermal expansion coefficients of magnitudes above 100 ppm/°C were achieved. Within the domain of common NTE materials, thermal expansion coefficients of single digits and up to several tens ppm/°C are commonly seen while colossal NTE materials are far and few between. The exhibition of anisotropic lattice thermal expansion of β-isomorphous Ti alloys was found to be easily translatable to the macro scale through simple thermomechanical treatment [3-5]. The introduction of β-isomorphous Ti alloys into this functional category of materials challenges the possibility of utilizing these alloys to combat conventional thermal strain induced in regular thermal expansion materials. Currently, within commonly known NTE materials such as (anti-)perovskites, silicates, zirconium tungstates, cyanides, iron-nickel alloys, and composites, some common innate disadvantages hinder the employability of these materials such as: thermal hysteresis, thermal conductivity, challenging synthesis conditions, chemical instability, non-linearity, brittleness, lack of tuneability and more [6-11] .

β-isomorphous Ti alloys have been ubiquitously known to be lightweight and strong, with easily tuneable stiffness through a combination of composition tuning and heat treatment. The material of

choice from this system of Ti alloys is Ti-Nb, as it is one of the most prototyped β-isomorphous Ti alloy. This alloy is one of the earliest and most reported Ti alloys for its NTE capability and further lends to proper comparability between studies. One of Ti-Nb alloys' greatest potential lie in the tuneability of its CTE through tailoring simple thermomechanical processes, allowing the possibility of a lightweight, strong, and low thermal expansion capable multifunctional alloy. The combination of the tuneability and capacity for large NTE allows for the alloy to be potentially paired with a wide range of materials acting as counter-strains to achieve a low or even zero thermal expansion.

The current work aims to reveal key properties surrounding the NTE performance and stability of Ti-Nb alloys. Studies on the NTE behaviour of Ti-Nb alloys have often reported the performance within the fully martensitic range where NTE is largely linear. Non-linearity is common in most, if not all, materials across an extended spectrum of temperatures and is one of the major concerns when combining different materials of dissimilar thermal strain response. These non-linear thermal strain responses can originate innately or as a result of volume change stemming from phase transformations. Documentation of the behaviour and evolution of NTE over a wide range of temperatures beyond the point of decomposition is crucial in enabling prediction of behaviour and lifetime of an employed material. Phase transformations, depending on surrounding parameters such as temperature, heating rate and time, could affect the long- or short-term thermal stability of NTE materials. However, laborious amounts of effort and time have not been invested into the investigation of the long- and short-term stability of NTE materials. Full comprehension of the NTE behaviour beyond the martensitic decomposition temperature also enables the possibility of alloy design around these metastable transformations to achieve a desired NTE behaviour, while furthermore strengthen our understanding of the complex metastable pathways of Ti-Nb alloys. In summary, the topics included in this work are:

i. **To characterize the thermal expansion behaviour of Ti-22Nb (at.%) alloy over a wide temperature range above the martensitic decomposition temperature. Ti-22Nb**.
ii. **To investigate the effects of long-term aging on the NTE, microstructure, and mechanical properties of cold-rolled Ti-22Nb (at.%) alloy.**

iii. **To study the evolution of NTE and sequence of phase transformations in cold-rolled Ti-22Nb (at.%) over a wide temperature range**.

The objectives for these aims were achieved mainly using ex- and in-situ X-ray diffraction methods for the determination of change in phase composition, lattice thermal expansion and occurring phase transformations. The obtained results were further supported microstructural observation techniques and mechanical properties tests for validation of the phases and precipitates formed.

1.2. Rationale

Titanium alloys are usually classified by the degree of stabilization of the equilibrium phases (α and β), and hence the retained phase(s) at room temperature. The classifications are usually α alloys, α+β alloys, and β alloys. Some may also classify near-α and near-β alloys which have compositions near the α/(α+β) or (α+β)/β phase boundaries.

α alloys are doped with "simple metal" α stabilizers such as aluminium, gallium, tin, and more. These alloys have good strength, toughness, creep resistance and weldability. The lack of a ductile-to-brittle transition positions these alloys to be suitable for cryogenic applications, while the β alloys lack such a property [12]. α alloys are employed in applications where strength is not a priority and corrosion resistance is prioritized [13, 14]. α+β alloys provide a range of achievable combinations of strength, toughness and high temperature properties through the adjustment of the alloy's phase constitution through heat treatment [14]. These alloys have good fabricability, exhibit high strength at ambient temperatures and moderate strength at high temperatures [12]. β alloys are doped with transition metals such as vanadium, niobium, tantalum, and more. These alloys have extremely good fabricability but prone to the ductile-to-brittle transition, making them inadequate for low temperature applications. Two subclasses of β alloys exist, β-isomorphous and β-eutectoid [12].

Non-β-isomorphous systems were not considered for the study. Even though NTE studies of some common established commercial compositions such as Ti-6Al-4V, Ti–5Al–5Mo–5V–3Cr–1Zr, Ti–10V–2Fe–3Al exist, lattice NTE magnitudes are often not reported. Besides that, the possible occurrence of intermetallic components and the occurrence of further decomposition of the β phase in

non-β-isomorphous systems was determined to possibly complicate the analysis process as more transformation pathways that could result in a change in NTE would have to be analysed. In addition, the reported macro NTE capability of these commercial Ti alloys is not as large as the reported value of binary Ti-Nb. A larger NTE magnitude such as the one provided by Ti-Nb helps distinguish changes in composition easier. Ti-Nb is the most commonly prototyped binary Ti alloy used to study the property of NTE in the martensitic phase, both in the lattice and macro scale. This ensures comparability for the reader between the many studies on the NTE of martensitic Ti-Nb. Comparatively, while lattice thermal expansion of other binary β-isomorphous Ti alloys exist for the equilibrium phases, lattice NTE studies on the martensitic of these binary Ti alloys are almost non-existent to the author's knowledge. Demakov et al. had published an in-situ heating study on the lattice parameters of a martensitic binary Ti-Mo alloy [15], but no lattice NTE values were reported. Hence, Ti-Nb was chosen for the availability and comparability of data for the readers.

1.3. Outline

The structure of this thesis is presented in the following order.

- Chapter 1 introduces the general trend of NTE materials and β-isomorphous Ti alloys which serves as a basis for the motivation and reasoning behind the need for this work. Major aims for this study were founded based on the trends and gaps in knowledge identified.
- Chapter 2 provides the reader with foundational knowledge of phase transformations and metallurgy of the β-isomorphous Ti system. This chapter also acts as a review of recent studies of NTE in Ti-Nb and Ti-Nb based materials.
- Chapter 3 describes the experimental methods used in this study. This chapter details the overall experiment workflow, relevant experimental conditions, apparatus, characterization techniques used in this study.
- Chapter 4 studies the macroscale thermal expansion behaviour of Ti-Nb alloys and serves as the foundation for Chapters 5 and 6. The macroscale thermal expansion of water quenched and cold-rolled Ti-Nb alloy was studied. The behaviour of the cold-rolled sample along RD was segmented into temperature regions of retained thermal expansion behaviour.

Temperature regions of retained NTE were studied in Chapter 5 for thermal stability. Temperatures above the retained NTE were studied in Chapter 6 to study the phase transformations occurring in the sample.

- Chapter 5 studies the long-term thermal stability of cold-rolled Ti-Nb held at temperatures above the martensitic decomposition temperature. The specimen were held at specific temperature intervals where NTE was retained after heating to study the change in NTE over 10-1000 hours.
- Chapter 6 studies the phase transformations behind the evolution and deterioration of NTE in cold-rolled Ti-Nb at high temperatures. A combination of diffraction and microscopy techniques were used to examine changes in phase composition and mechanical properties of the alloy to obtain a picture of the phase transformations that took place in the specimen.
- Chapter 7 summarizes the conclusions from the previous chapters while providing insight and suggestions on future directions that could be built upon the findings of this study.

2. Literature review

2.1. Recent developments in NTE materials and where Ti-Nb stands

Currently, there are few mechanisms that dominate commonly studied and used NTE materials [6, 10, 16]:

- Flexible network (conventional/structural type)
- Phase transition
- Magnetic transition
- Ferroelectric transition
- Charge-transfer transition
- Metal-insulator transition

Within the flexible network classification, NTE has been found in ceramic materials owing to the combined microstructural effect of the anisotropic thermal expansion of the ceramic crystal grain and the pores. [17-19] The thermal deformation of the crystal grains fills up the volumes occupied by pores and consequently result in NTE. Recently, this phenomenon was shown to exhibit large NTE in β-eucryptite, Ca_2RuO_4, Ti_2O_3, and $Ca_2Ru_{0.92}Fe_{0.08}O_4$ [20, 21]. There is also a constant effort to attempt to create composites using NTE materials as composite fillers or matrices as to control thermal expansion [22-24]. However, compared to common fillers, giant NTE materials face a problem of exhibiting high chemical reactivity with the matrix. Another difficulty of NTE filler materials is that they are usually produced as fine particles, hence introducing difficulty in controlling the crystallinity and specific microstructure requirements for these NTE materials to achieve their respective maximum potential.

Among the abovementioned mechanisms, Ti-Nb would be closest to the structural transition as it relies on a specific crystal structure to exhibit NTE. However, Ti-Nb does not depend on a combination of soft and rigid linkages that thermally expand to consume open spaces in the crystal lattice like the term flexible network suggests. Common NTE materials in this class are oxides such as: β-eucryptite [20], cordierite [25]. Materials that exhibit NTE through flexible networks usually lose

their NTE ability if the structural characteristics are lost. This facet of flexible network NTE materials is similar to Ti-Nb as Ti-Nb requires the martensite phase to exhibit NTE. The soft linkages in these crystal structures are often low in thermal conductivity and stiffness [26]. In contrast, Ti-Nb does not share these problems and shows great linear expansion coefficient, albeit anisotropic, and also possesses great thermal conductivity and stiffness.

Control of the shape and orientation of crystal grains in ceramics is desired to obtain desired NTE properties, but manipulation of these factors have proven to be difficult in ceramics. On the contrary, the shape and orientation of crystal grains in Ti-Nb have been shown to be easily manipulable as its NTE is tied directly to the unit cell. NTE that is exhibited through crystallographic unit cells is said to be extremely limited [16], but due to the NTE of Ti-Nb being directly related to the crystallography of the unit cell, it is much easier to manipulate the material to exhibit NTE through alteration of the overall microstructure. Currently, few studies have been manipulating the NTE of Ti-Nb through tensile stress, cold wire drawing, and cold-rolling. Regarding one of the key requirements for the performance of NTE materials, it is emphasized by Takenaka [16] that thermal expansion materials should exhibit stable microstructure and stable, reproducible NTE against thermal cycling. If a microstructure is temporary and destroyed in one thermal cycle in cases such as large porous volumes left due to poor sintering in the case of ceramics, then the material is highly undesirable. Ti-Nb has great potential to exhibit stability against thermal cycling as long as the martensitic reversion temperature is not reached and if diffusion does not occur or occurs slowly.

In 2014, Mohamed Abdel-Hady Gepreel [27] first reported that a cold-worked β-isomorphous titanium alloys of composition $Ti_{76}Nb_{17}Ta_6O_1$ exhibited macroscale NTE and could achieve ZTE through varying degrees of cold work and thermal processing history. Monroe et al. [1] reported in 2016 that one of the many martensitic shape memory alloys that exhibited NTE was Ti-Nb and could be achieved and tailored through cold-working alone. Wu Xiangwei then concurred that texturing was the reason for the NTE in textured Ti-Nb alloys [5]. Other than cold-rolling, alternative texturing methods have also been shown to allow macroscopic NTE. Wu demonstrated that texturing through

drawn Ti-Nb wires could also exhibit NTE along the axial direction of the wire [28]. Pre-straining also allows NTE to be exhibited along the tensile axial direction [3].

These studies have remained largely within the martensitic temperature range. While NTE is inherent to the martensitic phase, the phase transformations for the martensitic phase were not thoroughly studied until Bönisch [2, 29-31]. These phase transformations can give insight to the potential phase transformation pathways occurring in a cold-rolled Ti-Nb, but the effects of these martensitic phase transformation on the NTE and the mechanical properties in a cold-rolled Ti-Nb alloy is currently unexplored.

2.2. Classification of phase diagrams of Ti-X alloys

Elemental Ti consists of two equilibrium phases and exists as a hcp-α phase of space group ($P6_3/mmc$) at atmospheric pressure below 882 °C and goes through an allotropic transformation to the bcc-β phase with space group ($Im\bar{3}m$) which exists between 882 °C and below 1668 °C, above which melting occurs to the liquid state. Alloying of the Ti system alters the stability of the two equilibrium phases by increasing or lowering the β-transus temperature $T_{transus}^{\alpha/\beta}$ and allows for the existence of metastable phases α'/α" and ω under the right conditions.

A simple categorization of alloying elements in the Ti-X system, where X is the alloying element, was suggested by Molchanova [32]. Alloying elements can be qualitatively classified by their effect on the stability of the two equilibrium phases and consequently on $T_{transus}^{\alpha/\beta}$. Elements that increase the stability of β lowers $T_{transus}^{\alpha/\beta}$ and are known as β-stabilizing elements, while the opposite are known as α-stabilizing elements. Within the subgroup of β-stabilizing elements, further subdivision can be performed according to their solubility in the two equilibrium phases:

(a) Elements that are completely soluble in both equilibrium phases give rise to α-β isomorphous systems. Such elements include Hf and Zr. Fig. 2.1a presents the phase diagram of Ti-Zr. At

lower temperatures, the region of equilibrium α phase extends across the entire concentration range. At higher temperatures, the same is seen for the β phase.

(b) Elements exhibiting complete solubility in the β-phase but only a limited solubility in the α phase results in β-isomorphous systems. Elements such as V, Nb, Mo, Ta, W belong to this category. Fig. 2.1b presents the phase diagram of Ti-V as an example. The solubility limit of V in the α phase is reached at extremely lean compositions, while the solubility in the β-phase extends across almost the entire concentration range across a wide temperature range above ambient. In the particular case of the β-isomorphous systems where Ti-Nb alloys belong to, some elements produce an isomorphous phase diagram featuring a miscibility gap as seen in Fig. 2.1b, where the equilibrium phase composition between 676.57 °C and 844.5 °C is solid solution mixture of solute lean and rich compositions of β. Certain elements that give rise to β-isomorphous systems such as Ta do not feature a miscibility gap [41, 42].

(c) Elements that exhibit partial solubility in the β-phase and decomposes eutectoidally, where a high temperature phase decomposes into two distinct phases that does not consist of the original phase, usually into α-phase and an intermetallic Ti_mX_n (where *m* and *n* are of fixed ratios for specific intermetallic compounds) when cooled. A wide variety of elements give rise to these β-eutectoid systems which include but not limited to: Cr, Mn, Fe, Co, Ni, Cu, Pd, Ag, Pt, Au etc. Ti-Cr is taken as an example of a phase diagram from this system as presented in Fig. 2.1c.

In contrast, elements that enhances the stability of the α-phase are known as α-stabilizing elements. In this group, the subcategorization of elements depends on the degree of α-stabilization instead of solubility.

(a) Elements that exhibit “partial” α-stabilization result in peritectic reactions between the α phase and a mixture of β phase and intermetallics. Such elements include, but not limited to: B, Sc, Ga, Ca, Al, C etc. An example of this system is shown in Fig. 2.1d.

(b) Elements that exhibit "complete" α-stabilization which allows the α phase to be in equilibrium with the liquid phase in certain compositions. These elements include N and O. An example of this system is shown in Fig. 2.1e.

The natural next step after qualitative description of the effects of alloying elements on the Ti-X phase diagram is the quantification of the effect of alloying elements on the Ti-X system. The quantification method first follows the qualitative classification in which elements are categorized into α or β stabilizers. For β stabilizers, a common way of quantifying the degree of β stabilization is the molybdenum equivalent ($[Mo]_{eq}$) obtained by summing the individual contribution of every alloying element towards β stability and normalized with respect to the stabilization strength of molybdenum in wt.%. The widely known equation for $[Mo]_{eq}$ is given as [12, 33]:

$$\begin{aligned}[Mo]_{eq} = {} & 1.0(wt.\%\,\boldsymbol{Mo}) + 0.67(wt.\%\,\boldsymbol{V}) + 0.44(wt.\%\,\boldsymbol{W}) + 0.28(wt.\%\,\boldsymbol{Nb}) \\ & + 0.22(wt.\%\,\boldsymbol{Ta}) + 2.9(wt.\%\,\boldsymbol{Fe}) + 1.6(wt.\%\,\boldsymbol{Cr}) + 1.25(wt.\%\,\boldsymbol{Ni}) \\ & + 1.7(wt.\%\,\boldsymbol{Mn}) + 1.7(wt.\%\,\boldsymbol{Co}) - 1.0(wt.\%\,\boldsymbol{Al})\end{aligned} \tag{2.1}$$

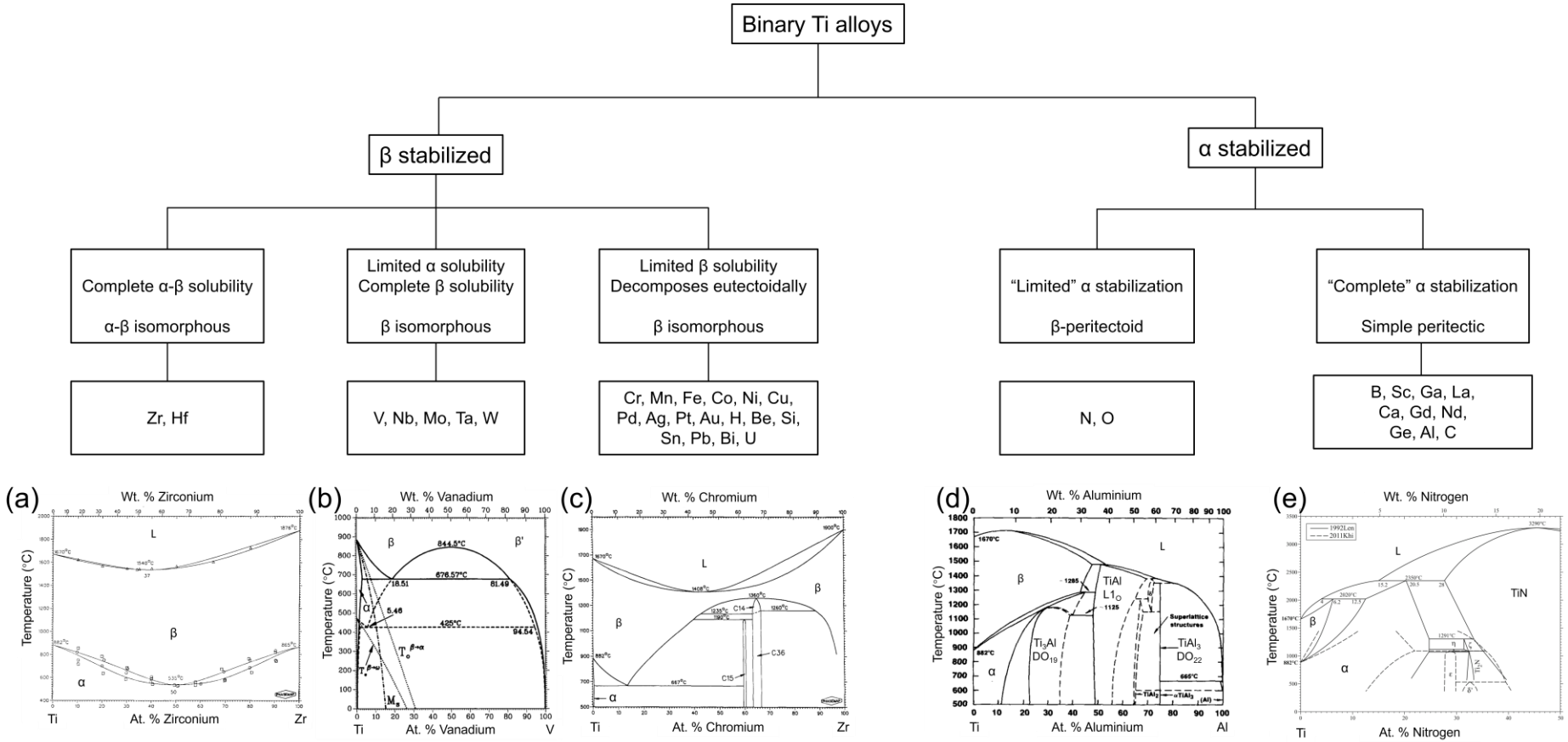

Fig. 2.1. Classification of phase diagrams within the binary Ti alloy system. Examples of actual phase diagrams taken for (a) Ti-Zr [34] (b) Ti-V [35] (c) Ti-Cr [36] (d) Ti-Al [37] (e) Ti-N [38]

The respective constants in front of individual weight percentage of elements is the weight ratio of that element to molybdenum needed to observe a stable β phase at room temperature. For example, 10 wt.% V is required to obtain a stable β phase in the Ti-V system, compared to 15 wt.% Mo in a Ti-Mo system. Hence the ratio of $\frac{10}{15} = 0.67$ is obtained for V. Notice that there is a sole subtraction term for aluminium at the end of the equation. This ties into the quantification of α stabilization, where the sum of contribution of α stabilization is normalized with respect to aluminium and given as the following [33]:

$$[Al]_{eq} = 1.0(wt.\%\,\boldsymbol{Al}) + 0.17(wt.\%\,\boldsymbol{Zr}) + 0.33(wt.\%\,\boldsymbol{Sn}) + 10(wt.\%\,\boldsymbol{O} + wt.\%\,\boldsymbol{N}) \quad (2.2)$$

These equations, however, are not all encompassing as both the molybdenum and aluminium equivalent does not include an exhaustive list of all elements that give rise to α and β stability but only includes the most commonly used elements alloyed with Ti.

2.3. Phase diagram of Ti-Nb system

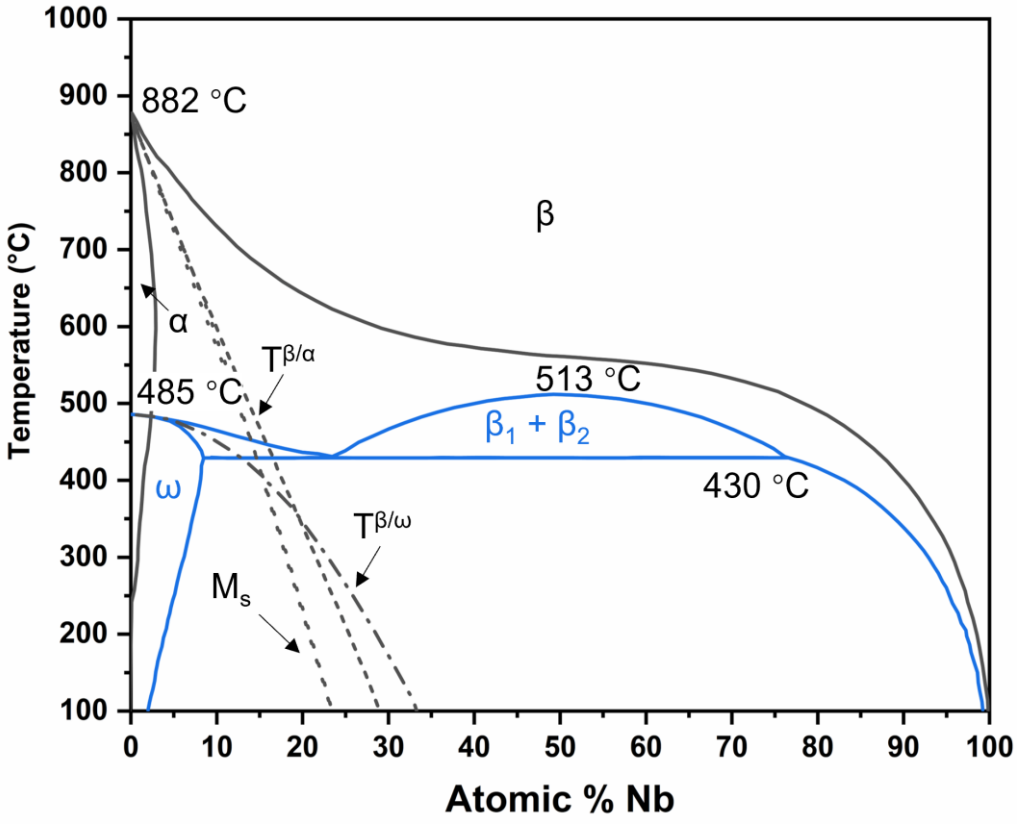

Fig. 2.2. The Ti-Nb system phase diagram by Zhang er al. including stable phases (solid lines) and metastable phases (dotted lines) [39]

Fig. 2.2 shows the Ti-Nb binary phase diagram calculated by Zhang et al. in 2001 [39] which features the stable α-β underlying a superimposed metastable β-ω phase diagram. A more recent Ti-Nb phase diagram was calculated by Bönisch et al. [40] features a stable equilibrium miscibility gap seen in β-isomorphous systems like Ti-V, but the authors had reflected that the calculated phase diagram was still speculative and requires experimental validation. The main differences between these two calculated phase diagrams could lie in the availability of more recent experimental data and also the deviation from the regular solution model used earlier by Zhang et al. Earlier works by Bönisch also confirmed the reliability of the phase diagram calculated by Zhang et al., hence this phase diagram was chosen to be representative of the Ti-Nb binary system at the time of writing. As mentioned before, the β-isomorphous system features limited solubility of the alloying element in α but is completely soluble in β. This solubility limit of Nb in α can be observed in the phase diagram to be approximately 2-3 at.% Nb [39, 41, 42]. The characteristic metastable reactions observable from the phase diagram include:

(a) The reaction occurring within the miscibility gap between 430-513 °C at composition of 50 at.% Nb between the single composition β phase and two separate compositions (lean and rich) of β [39].

(b) The allotropic reaction between β and ω at 485 °C at 0 at.% Nb [39].

(c) The monotectoid reaction at 430 °C with composition of 23.3 at.% Nb decomposing $\beta \rightarrow \beta + \omega$ [39].

When rapidly quenched from the high temperature β phase to below the T_0 lines ($T^{\beta/\omega}$, $T^{\beta/\alpha}$) and the martensitic start temperature line (M_s), both of which are shown as dashed lines in Fig. 2.2, metastable phases can be precipitated instead of the equilibrium phases. The T_0 line represents the temperature and composition where the Gibbs free energies of the two phases in consideration are equal. A metastable phase can be precipitated as a result of insufficient time or temperature (energy) to overcome the energy barrier for the process to achieve equilibrium to take place. Details of the thermodynamics will be discussed in later in Section 2.5. In the Ti-Nb system, the stable α and β, and

the metastable ω, α', and α" are all considered disordered phases. Within disordered phases, atoms have no preferred lattice sites and the probability of finding an atom of a specific element is proportional to the molar fraction of that element in the solution at any lattice sites. Among the metastable phases, ω is formed from a mixed mode diffusional and displacive reaction, while the martensitic phases α' and α" are formed only by displacive reactions.

Metastable phases observable upon quenching is highly dependent on the quenched temperature and overall alloy composition. Although there is a general range of compositions for the precipitation of these phases upon quenching, the range is not absolute as composition is not the sole determinant for the occurrence of the phases. Fig. 2.3 shows the schematic composition range for the metastable phases obtainable upon quenching to near room temperature. At low solute concentrations up to the "boundary" of α'/α" of ~7-11 at.% [30, 42], a mixture of α'+α" is known to form martensitically when cooled from the single β phase to below the $M_s^{\alpha'/\alpha''}$ temperature at high cooling rates. Beyond 11 at.%, single phase α" can be retained upon quenching to around 24 at.% [30, 42]. Above 24 at.%, a mixture of metastable β+α" is obtained as a result of the incomplete martensitic transformation [30, 42] when the final quenched temperature is below $M_s^{\alpha''}$ but above $M_f^{\alpha''}$. At concentrations above 24 at.%, the fraction of α" then decreases with Nb concentration up to a limit of ~30 at.% when single phase β is retained upon quenching. The composition range to form athermal ω upon quenching is shared with the other metastable phases due to an extensive T_0 range that reaches to elemental Ti, with observations being made at concentrations as low as 6.7 at.% up to around 40-45 at.% [31, 42]. ω requires β as a parent phase to form and is known to compete with other phases such as α' and/or α" for formation [43-45]. Hence, at lower concentrations where the martensitic phases are more stable ω might struggle to form and only a trace amount might be present in the final quenched alloy. At intermediately higher concentrations where β does not fully transform to martensite ($M_s < T < M_f$), the formed martensite has lower stability and the remaining β can form ω with relative ease. This results in a peak in mechanical strength within certain intervals in near-β Ti alloys which is contributed by the ω phase [12, 46, 47]. The precipitation of ω and both martensitic phases α'/α" are affected by external factors such as cooling rate and impurities. Both these phases require intermediate to fast

cooling rate from the single β phase to precipitate, in the case of ω specifically the athermal ω forms. Impurities such as oxygen are known to suppress the formation of the martensitic phases and promote the formation of athermal ω phase [48-52]. Other than these two factors during quenching, the isothermal ω can also form during heating of a metastable β Ti alloy. At higher solute concentrations, β is fully stabilized and metastable/stable β is preferably retained upon quenching.

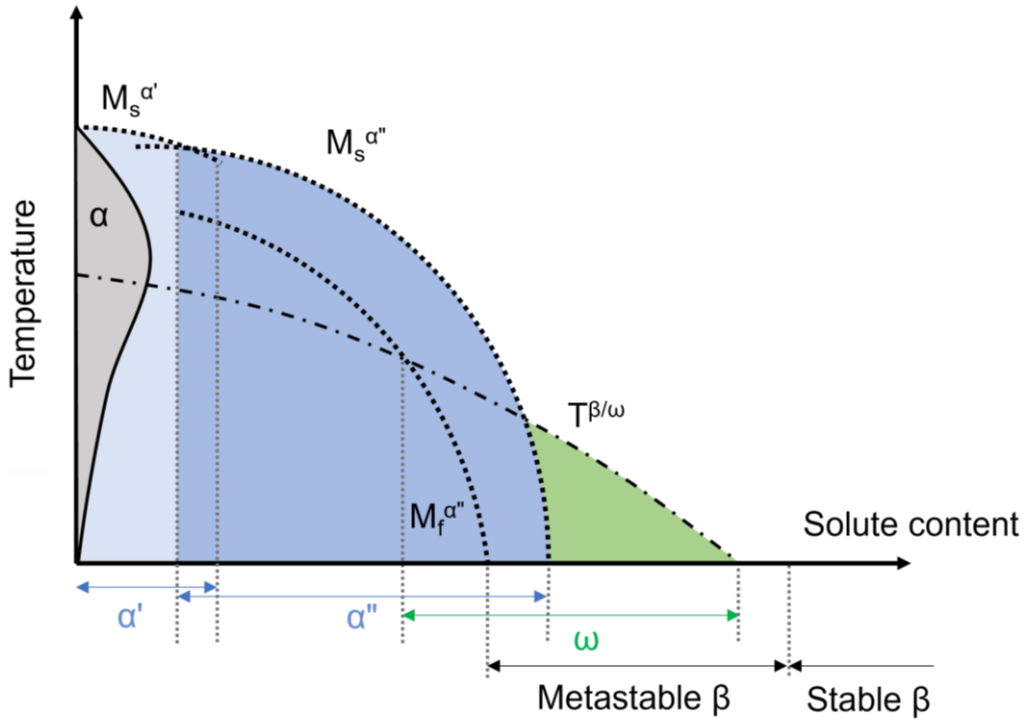

Fig. 2.3. Schematic diagram of obtainable metastable phases upon quenching from the single β phase at various β stabilizer content in a Ti-Nb system. Adapted from [13, 29] .

2.4. Crystallography of phases within the Ti-Nb system

2.4.1. Equilibrium phases

As mentioned before, the α phase has a hcp structure with a space group of ($P6_3/mmc$) and the β phase has a structure of bcc with space group ($Im\bar{3}m$). The lattice parameters of hcp α-Ti and bcc β-Nb are given in Table 2.1. Lattice parameters of α and β in Ti alloys do not differ much from their pure elements. The crystal structure information including the Wyckoff letter, site multiplicities and

fractional coordinates of describing the four phases in β-isomorphous Ti alloys were compiled in Ref [29]. The orientation relationship between the α and β phase was first established by Burgers in the study of the β → α transition in Zr alloys [53]. This relationship also applicable to Ti alloys and graphically presented in Fig. 2.4 is given by:

$$\{110\}_\beta \parallel \{0001\}_\alpha \quad (2.3)$$

$$\langle \bar{1}11 \rangle_\beta \parallel \langle 11\bar{2}0 \rangle_\alpha \quad (2.4)$$

Table 2.1. Crystallographic information of Ti and Nb in the Ti-Nb system

Element	Crystal structure	Lattice parameters (Å)			Ref
		a	b	c	
α-Ti	hcp	2.9506		4.686	[54]
		2.9511		4.6843	[55]
		2.9508		4.6855	[56]
		3.3063			[57]
β-Nb	bcc	3.30041			[58]
		3.300208			[59]

2.4.2. Martensitic phase

Upon cooling from the high temperature single β phase with a high cooling rate, two forms of martensite, α' and α'', can form depending on the solute concentration. The solute lean α' phase has a hexagonal structure identical to α with space group ($P6_3/mmc$) [29] and thus the Burgers relation between β and α can be applied to β and α' as well. The relatively solute rich α'' phase has an orthorhombic structure with space group ($Cmcm$). The martensitic transformation is formed through the cooperative movement of atoms along a shear front, later discussed as an athermal displacive transformation in Section 2.5 that is characterized by a discreet change in volume when transformed from the parent β phase. The distortion required to deform the parent β lattice with lattice parameter

a_A to an orthorhombic lattice with lattice parameters a_M, b_M, c_M is described as the lattice distortion matrix, *T* [60]:

$$T = \begin{bmatrix} \frac{a_M}{a_A} & 0 & 0 \\ 0 & \frac{b_M + c_M}{2\sqrt{2}a_A} & \frac{b_M - c_M}{2\sqrt{2}a_A} \\ 0 & \frac{b_M - c_M}{2\sqrt{2}a_A} & \frac{b_M + c_M}{2\sqrt{2}a_A} \end{bmatrix} \quad (2.5)$$

The transformed cubic unit cell, now orthorhombic, can then be related to the parent phase by quantifying the strain required for the martensitic transformation. The martensitic transformation strain, ε_M^i, required to transform a cubic unit cell to orthorhombic is calculated as the difference between the unit cells described as [60]:

$$\varepsilon_M^i = \frac{|x_M| - |x_A|}{|x_A|} \quad (2.6)$$

Where x_A and x_M are the lattice parameters of the parent cubic phase and orthorhombic phase respectively, and $x'=Tx$. As seen in Equation (2.6, the transformation strain is based on the difference in lattice parameters between the two phases. The martensitic transformation strain in Ti-Nb alloys was reported to be composition dependent by Kim and Miyazaki [60] and smallest when the overall alloy composition is solute rich. This is because the lattice parameters of α" varies largely with Nb content and the orthorhombic unit cell gains increasing resemblance to the parent β phase with increasing Nb content. The lattice parameters of α" are not largely invariable like the stable α and β phases but changes drastically with Nb content. The change in lattice parameters per at.% change in Nb has been reported by Kim and Miyazaki [60] to be: $\Delta a = 1.364 \times 10^{-3}$ nm/at.% Nb, $\Delta b = -1.546 \times 10^{-3}$ nm/at.% Nb, $\Delta c = 0.238 \times 10^{-3}$ nm/at.% Nb. The orientation relationship between α" and β can be roughly equated as:

$$[010]_{\alpha''} \parallel \langle 110 \rangle_\beta \quad (2.7)$$

$$[100]_{\alpha''} \parallel \langle 00\bar{1} \rangle_\beta \quad (2.8)$$

$$[001]_{\alpha''} \parallel \langle \bar{1}10 \rangle_{\beta} \tag{2.9}$$

This is because the principal directions $[100]_{\alpha''}$ and $[010]_{\alpha''}$ have been reported to be rotated 2-3° from $\langle 00\bar{1} \rangle_{\beta}$ and $\langle 110 \rangle_{\beta}$ respectively. The graphical representation of this orientation relationship shown in Fig. 2.4. The entire $Cmcm$ α" unit cell cannot be fully described by the lattice parameters of α" as the 2 atoms per unit cell in the $(002)_{\alpha''}$ plane requires the use of a fractional coordinate *y* to fully describe the atoms in the $(002)_{\alpha''}$ plane along the $\langle 010 \rangle_{\alpha''}$ direction [61]. Another recently proposed method of describing the same atoms in the $(002)_{\alpha''}$ plane was proposed by Demakov, where the atoms in this plane were envisioned as the base of a tetrahedral, but this method of describing the unit cell has not been widely adopted yet [62].

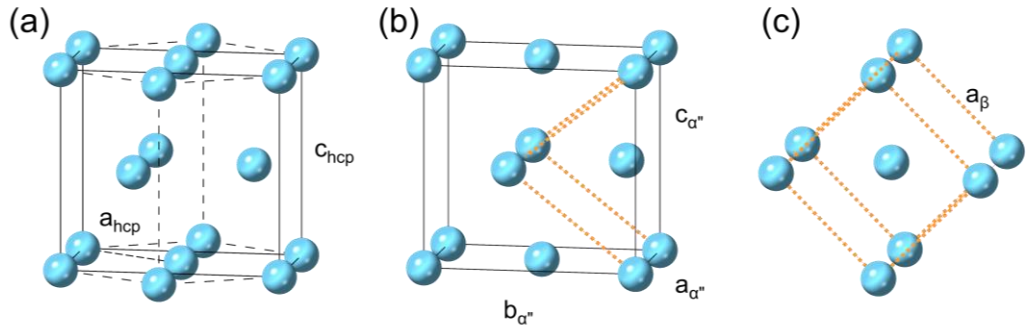

Fig. 2.4. Unit cells of (a) hcp-α (b) orthorhombic α" (c) bcc-β, with their lattice parameters illustrated.

Two commonly observed martensite morphologies in Ti alloys are the "plate" and the "lathe" morphology as described by Banerjee [13]. Although many authors use these two terms interchangeably, the consistencies in the following descriptions of morphologies will be attempted. In plate morphologies, different variants of martensite, exactly six for the orthorhombic α", can form with equal probability. The sequence of formation of these martensites are named "generations" with the earliest forming being the first generation, and subsequent being second and so forth. The earlier generations of martensite plates divide the parent grain and subsequent generations form within the divided parent grain, occupying lesser and lesser volume with successive generations. The formation of martensites is accompanied by an elastic strain field evidently due to the difference in crystallography and volume with its surrounding parent phase. Hence the formation of subsequent

martensites aim to reduce the overall strain energy in the parent grain. The elastic strain field of a cluster of martensite can "couple" to reduce overall strain energy. This is known as self-accommodation. A micrograph of self-accommodated martensite in Ti alloys are shown in Fig. 2.5a-c where martensite plates of three different variants form a cluster within a bigger cluster of two plates [63, 64]. Martensite can also assume the morphology in a lathe form. Lathe martensites usually form in parallel groups and they can have the same orientation. Twins commonly form within these lathes dividing the lathe in the minor axes. Observed micrographs of martensitic lathes can be seen in Fig. 2.5d-e where CV1 and CV3 are the twin related martensite within a single lathe [65]. In general, solute lean alloys with high M_s temperatures above 923K are usually associated with the lathe morphology [13].

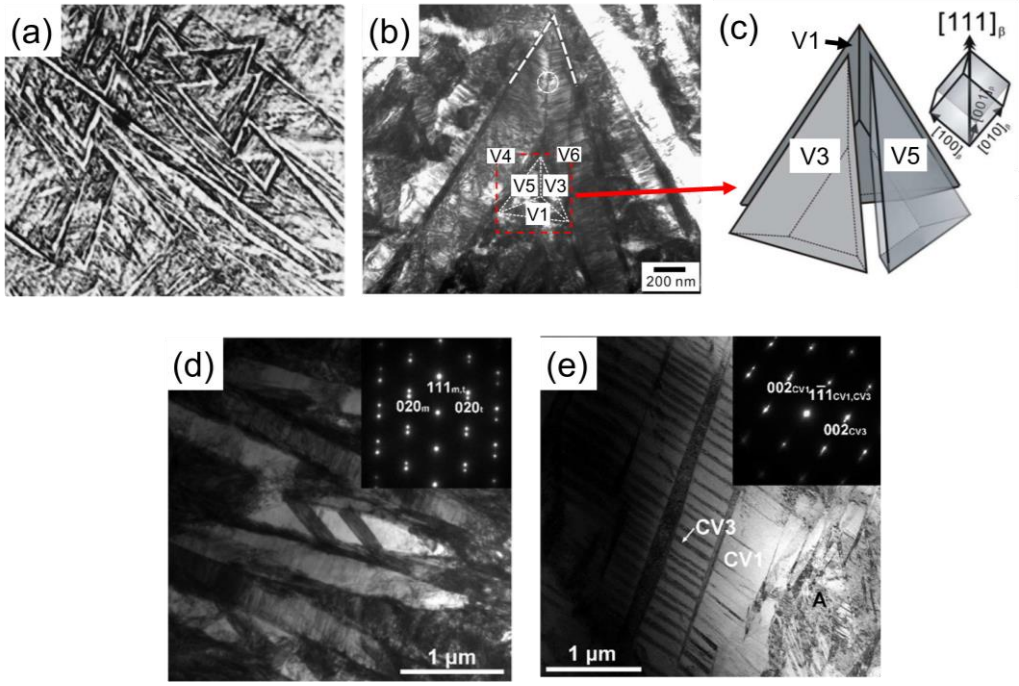

Fig. 2.5. Micrograph examples of (a) lathe martensite [63] . (b-c) Variants of martensite forming in a lathe morphology [64] . (d-e) Martensite forming in the plate morphology and the twin variants forming within the plates [65] .

2.4.3. ω phase

The ω phase can have a hexagonal, but not close packed, unit cell of space group $P6/mmm$, or a trigonal unit cell of $P\bar{3}m1$. Both structures originate from the same parent β phase, but the extent of the formation mechanism determines the unit cell structure. The ω phase can be formed from β

athermally or isothermally through the collapse of specific planes of atoms in the β unit cell. Athermally formed ω forms in a purely displacive way, while isothermally formed ω forms through a mixed-mode diffusive and displacive transformation that involves the rejection of β stabilizer atoms. A complete collapse of the specific β planes results in a hexagonal unit cell, while an incomplete collapse results in the trigonal unit cell. The orientation relationship between β and ω can be described as:

$$\{111\}_\beta \parallel (0001)_\omega \tag{2.10}$$

$$\langle 1\bar{1}0\rangle_\beta \parallel \langle 11\bar{2}0\rangle_\omega \tag{2.11}$$

Where the $\{111\}_\beta$ act as the basal plane for the hexagonal ω unit cell as shown in Fig. 2.6c. The plane collapse mechanism is illustrated in Fig. 2.6a where the stacking sequence of $(222)_\beta$ planes of the β unit cell can be seen in an ABCABC... pattern. The planes B and C collapse into an intermediate position between the two planes in a displacement similar to a sinusoidal wave [13] forming the $(0002)_\omega$ plane in Fig. 2.6b. Geometrically, the magnitude of displacement of atoms in planes B and C for a complete collapse of atoms can be calculated to be $\frac{1}{2}(222)_\beta$ [66]. This can be described in terms of the lattice parameter of β, a_β, to be $\frac{a_\beta}{4\sqrt{3}}$ for a complete collapse. A completely collapsed bcc structure gives rise to a sixfold symmetry hexagonal structure, while a displacement magnitude less than this results in an incomplete collapse giving rise to a trigonal structure with a threefold symmetry.

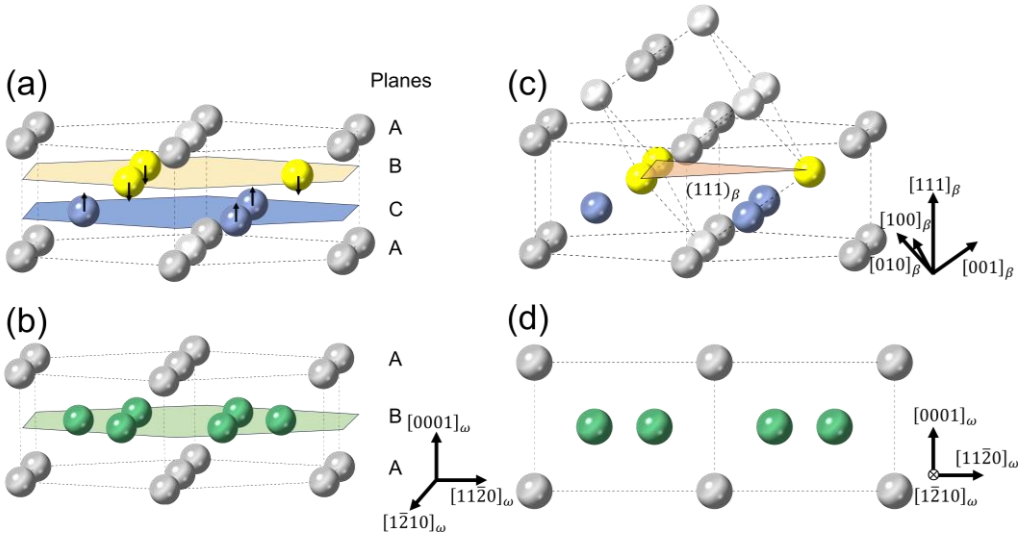

Fig. 2.6. (a) The β structure before forming ω, with an ABCABC… sequence along $\langle 111 \rangle_\beta$. The coloured planes are to collapse to form ω. (b) The collapsed B and C planes to form $(0002)_\omega$. (c) The β structure showing the β unit cell and the $(111)_\beta$ plane that is parallel to the ω basal plane. (d) The ω structure viewed parallel to $[1\bar{2}10]_\omega$ as seen in most TEM micrographs.

The extent of the collapse has been largely attributed to the composition of the alloy. In solute rich β stabilized Ti alloys, quenching produces an incompletely collapsed trigonal ω_{ath} [67, 68]. It is estimated that Ti-Nb alloys with Nb concentration of less than 35 at.% produces a completely collapsed hexagonal ω_{ath}. The extent of collapse and concentration was found to be closely related and recently been elucidated to not be a purely displacive process, but a mixed displacive-diffusional process [69-71]. The magnitude of collapse is thought to vary with Nb concentration, hence in isothermal conditions when Nb is diffusively rejected from the ω phase, the trigonal structure slowly transforms to a hexagonal structure. The collapse of two planes in the $\langle 111 \rangle_\beta$ direction into an intermediate position in an isothermally formed ω_{iso} results in a detectable volume contraction of up to 15% [13]. The collapse along the $\langle 111 \rangle_\beta$ direction can be observed through microscopy techniques such as HAADF-STEM as seen in Fig. 2.7a, e whereas Fig. 2.7b-d represents a schematic of the collapse mechanism. In this figure, an ω embryo was observed alongside the surrounding β matrix, both of which were differentiated by collapse of the B and C planes along the $\langle 111 \rangle_\beta$ direction.

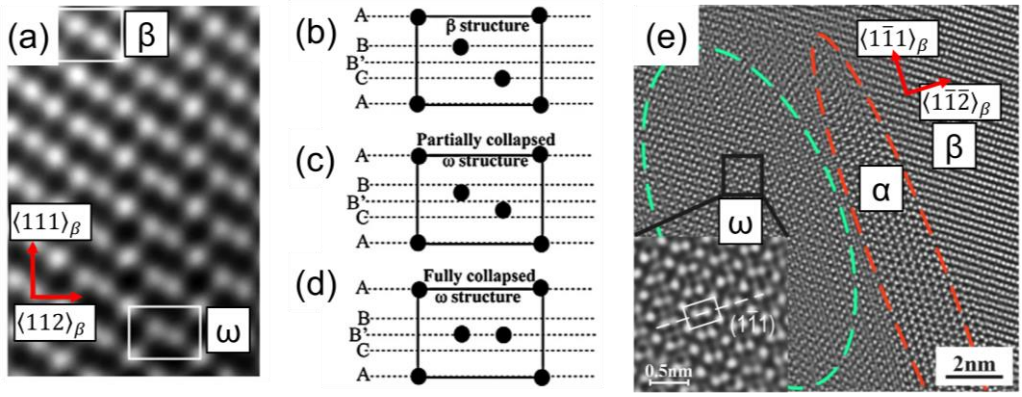

Fig. 2.7. HAADF-STEM images of a β matrix alongside a ω precipitate. (b-d) Illustrations of the ω phase plane collapse formation process. (e) Another HAADF-STEM micrograph showing a further collapsed ω structure.

Geometrically, lattice parameters a and c can be related to the β phase with the relationship: $a_\omega = a_\beta\sqrt{2}$, $c_\omega = \frac{\sqrt{3}}{2}a_\beta$. The microstructure of athermally formed ω_{ath} is often globular with radius of several to tens of nanometers. Under favourable isothermal conditions, globular ω precipitates can grow to ellipsoidal particles up to several hundreds of nanometers along the major axis, or as cuboidal precipitates [44].

2.5. Phase transformations within the Ti-Nb system

2.5.1. Thermodynamics of phase transformations

Thermodynamically, phase transformations aim to decrease the free energy, or free enthalpy, of a system. The Gibbs free energy, *G*, of a phase within the system can be expressed by the equation:

$$G = H - Ts \tag{2.12}$$

Where H is the enthalpy, T is the absolute temperature, and s is the entropy. The enthalpy, H, is a measure of the total heat energy of the system and can be further expanded into:

$$H = U + PV \tag{2.13}$$

Where *U* is the internal energy, *P* is the pressure and *V* is the volume. The internal energy of the phase comprises of the kinetic and potential energy of all atoms in the system. The change in enthalpy, *H*, at constant pressure can be measured by the specific heat capacity, C_p, by definition:

$$\left(\frac{\partial H}{\partial T}\right)_P = C_P \tag{2.14}$$

With these definitions in place, the change in free enthalpy, G, with varying temperature and pressure can be expressed as:

$$dG = -sdT + VdP \tag{2.15}$$

Under the assumption of constant pressure, the change in pressure, *dP* can be taken as zero to obtain the slope of free enthalpy, *dG*:

$$dG = -sdT \tag{2.16}$$

Utilizing the established equations, the plots of enthalpy and free enthalpy of a single component system at constant pressure can be plotted in Fig. 2.8a. At any point, the system would prefer to have a phase with the lower free enthalpy. Illustrated in Fig. 2.8b, the free enthalpy curves of the liquid and solid phase are drawn schematically. The melting temperature, T^M, can be defined as the temperature where the free enthalpy of the two phases is equal. Below T^M, the solid phase is the preferred phase with lower enthalpy while beyond the melting temperature, the liquid phase is preferred.

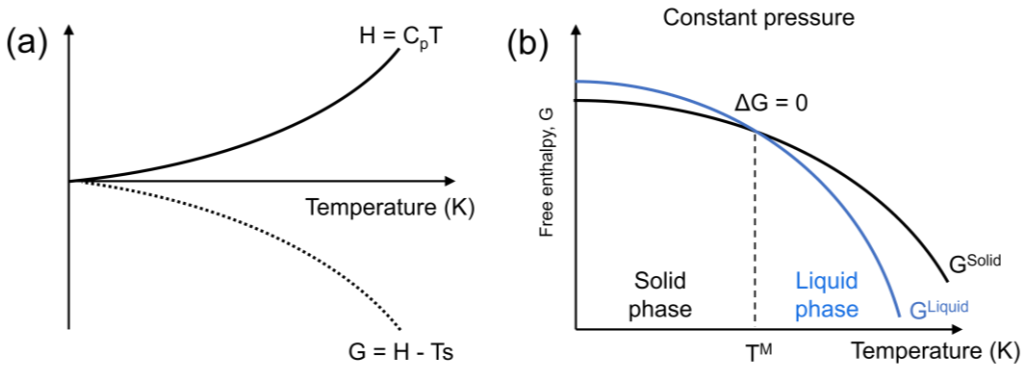

Fig. 2.8. (a) Illustrations of the variation of internal energy, H, and free enthalpy, G, with temperature. (b) The free enthalpy curve of two competing phases in a system, where the phase of lowest enthalpy forms.

At this point, phase transformations can be classified based on the derivative of the free enthalpy in Equation (2.12. The first derivative of *G* is given by:

$$\frac{\partial G}{\partial T} = -s \tag{2.17}$$

$$\frac{\partial G}{\partial P} = V \tag{2.18}$$

A first order transformation can be defined as a discontinuity in the first derivatives of the free enthalpy, namely the volume and entropy, at the equilibrium transformation point where the free enthalpies are equal (ΔG=0). Discontinuity in the enthalpy can be inferred from Equation (2.13 as a consequence of discontinuity in volume. Conversely, a second order transformation refers to a discontinuity in the second derivative of the Gibbs free energy. From classical thermodynamics, the specific heat can be related to the entropy at constant pressure as shown in Equation (2.19 and related to the second derivative of Gibbs free energy. Thus, a discontinuity in the specific heat would be observed in systems where second order transformation occurs. The discontinuity in volume, enthalpy, and entropy in first order transformations and discontinuity in specific heat in second order transformations are depicted in Fig. 2.9. Certain transformations such as ferroelectric or ferromagnetic transformations are classified as a mixed order transition that features finite discontinuous jumps of the thermodynamic properties enthalpy, entropy and volume [13].

$$\frac{C_P}{T} = \left(\frac{\partial s}{\partial T}\right)_P = \left(\frac{\partial^2 G}{\partial T^2}\right)_P \tag{2.19}$$

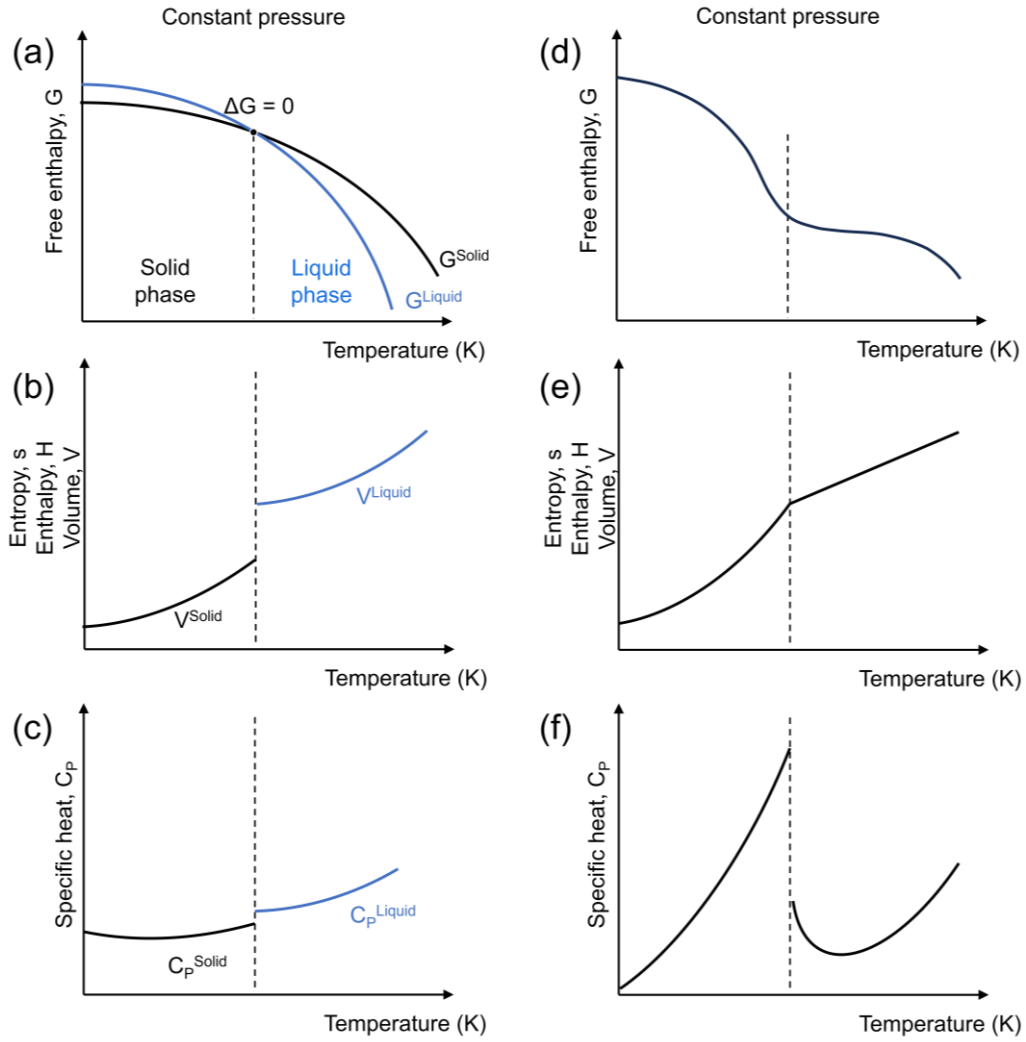

Fig. 2.9. The variation of free enthalpy, entropy, enthalpy, and volume in a system of (a-c) a system exhibiting first order transformation, (d-f) a second order transformation. Adapted from [72].

However, in actual phase transitions, precipitates do not immediately form at ΔG=0, rather some extra driving force, represented by the free enthalpy of nucleation, is required for the transformation to proceed. Taking solidification as an example, the extra driving force is represented in Fig. 2.10 as $\Delta G_{nucleation}$ for the nucleation energy of the solid phase. Depending on the nature of the nucleation, the nucleation energy differs depending on which restraining forces need to be overcome. For example, in solidification, the solid-liquid interfacial energy and the volume free energy need to be overcome. In another case of homogeneous diffusional nucleation within a solid solution, additional strain energy

has to be overcome if the transformation is of first-order nature and the product phase has a different volume to the parent phase.

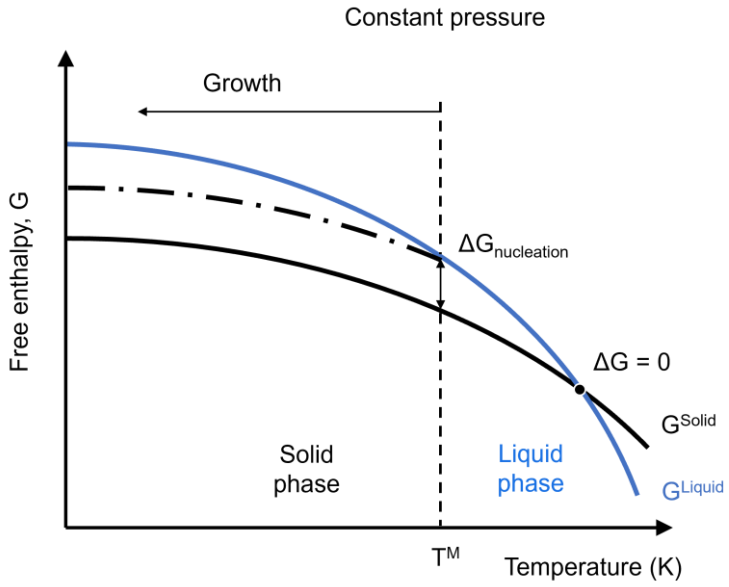

Fig. 2.10. Illustration of a free enthalpy curve when accounting for nucleation energy required for precipitation of a new phase. The example shown is of a liquid-solid transition but is generally applicable for any nucleation process.

In a binary solution system such as an alloy with molar fractions X_A and X_B for the element A and B with Gibbs free energy of G_A and G_B respectively, the expression of free enthalpy of such a system, G_{AB}, can be altered from Equation (2.12 to include the latent heat of mixing, ΔG_{mix}:

$$G_{AB} = X_A G_A + X_B G_B + \Delta G_{mix} \tag{2.20}$$

$$\Delta G_{mix} = \Delta H_{mix} - T\Delta s_{mix} \tag{2.21}$$

The latent heat of mixing includes two terms, ΔH_{mix} and $-T\Delta s_{mix}$, namely the enthalpy of mixing and entropy caused by mixing. The enthalpy of mixing describes the attraction between the two elements, in which an atom A would prefer to be surrounded by B, or the reverse where an atom A would prefer to be surrounded by similar atoms. The entropy of mixing describes the entropy arising from the different atom configurations that are possible. In an ideal solution where the two types of atoms in the binary solution would not attract nor repel each other, ΔH_{mix} would be zero, and thus $\Delta G_{mix} = -T\Delta s_{mix}$. In a regular solution model, ΔH_{mix} would be a non-zero term. When the two types of atoms

interact favourably, the ΔH_{mix} is a negative term, vice versa. The two terms in the latent heat of mixing can be described as:

$$\Delta H_{mix} = \Omega X_A X_B \tag{2.22}$$

$$\Delta s_{mix} = -R(X_A \ln X_A + X_B \ln X_B) \tag{2.23}$$

$$\Delta G_{mix} = \Omega X_A X_B + RT(X_A \ln X_A + X_B \ln X_B) \tag{2.24}$$

The term Ω describes the nature of the interaction between the two types of atoms. Attraction between the two types of atoms results in a negative value and hence a negative ΔH_{mix}, and vice versa for repulsion. Most phase diagrams calculated for the Ti-Nb system have employed the regular solution model [35, 73-75]. More recently, the enthalpy of mixing has been represented using the Redlich-Kister polynomial to calculate the phase diagram of the Ti-Nb system [40, 76].

In order to predict the likelihood of the occurrence of a phase transformation, the chemical potential can be looked towards as an indicator of equilibrium in a system. The Gibbs free energy curves of two phases, α and β, with a respective composition of X_1 and X_2 in a binary solution of two elements, A and B, with an overall composition between X_1 and X_2 at constant temperature and pressure can be represented with respect to concentration as shown in Fig. 2.11a. The intercept of the tangent at either end of the pure element is known as the chemical potential of that element within that specific phase within the solution. E.g. μ_A^β represents the chemical potential of element A in phase β. It can be observed in Fig. 2.11a that the chemical potentials of μ_A^α and μ_A^β are not equal on the side of pure A. The same is seen on the pure B side with μ_B^α and μ_B^β. This indicates that the system is not in equilibrium and a phase transformation is required to lower the Gibbs free energy of the system. The composition of the two phases can be changed through phase transformation to obtain Fig. 2.11b, where the final composition of α and β are X_3 and X_4 respectively. These two points share a common tangent as shown in Fig. 2.11b and the chemical potentials on each of the pure element side are equal, thus no phase transformation takes place, and the system is at equilibrium.

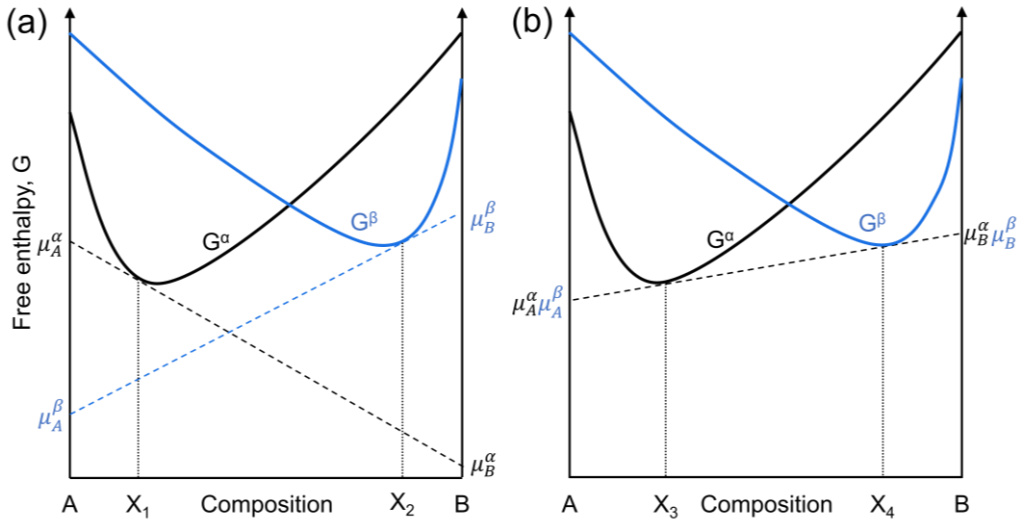

Fig. 2.11. The free enthalpy vs composition curve of a system with two competing phases. (a) The system is at inequilibrium with two phases of unequal chemical free energy and do not share a common tangent. (b) The composition of the two phases change to balance the chemical free energy and share a common tangent to achieve equilibrium.

2.5.2. Phase transformation mechanisms

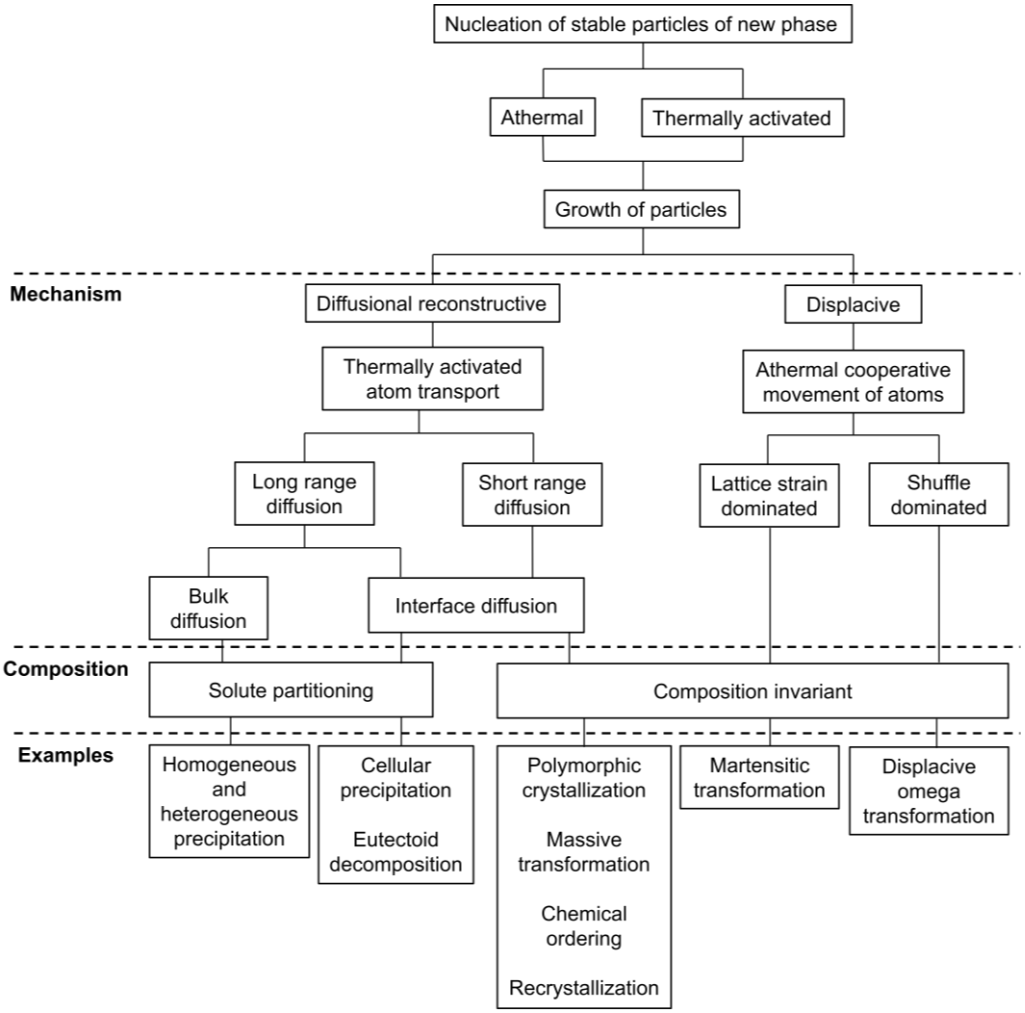

Fig. 2.12. Classification of first order phase transformations adapted from Banerjee [13].

Kinetically, phase transformations can be separated into thermally activated or athermal processes. While a lack of thermal energy can slow down or completely halt thermally activated processes from proceeding, athermal processes cannot be suppressed by quenching. Diffusional or reconstructive processes are unfailingly always thermally activated processes, while “true” displacive processes are athermal processes. Both the nucleation and growth of product phases can proceed through either one these classifications.

The step of nucleation and growth is exclusive to the previously mentioned first-order, or discrete transformations. Discontinuity in the specific volume at the transformation temperature results in distinct features following the nucleation of the first-order nature. The coexistence of the product and parent phase separated by clear phase boundaries observable under microscopy techniques are distinct

first-order transformation characteristics. The growth of the nucleated product phase occurs through the expense of the parent phase through the propagation of a transformation front. The mechanism in which this growth happens, however, is not exclusive to diffusive/reconstructive nor displacive and similarly, the composition between the parent and product phases can be invariant or otherwise. Most phase transformations in metallic systems are of the first-order nature. In second order, or continuous transformations, the product and parent phase are indistinguishable by phase boundaries or interfaces and transforms as a whole, rather than the propagation of a transformation front.

As mentioned previously diffusive/reconstructive transformations are always thermally activated. Long range atomic transport involves solute partitioning which ultimately results in the product phase not inheriting the composition of the parent phase. Examples of solute partitioning in Ti alloys include the decomposition of β into α+β through elevated thermal conditions [2, 77, 78]. Conversely, short range diffusion involves atomic transport of several atomic distances at most and are mostly composition invariant. Examples of composition invariant short-range diffusion include massive transformations where the transport of atoms occurs only at the transformation front. Displacive transformations operate by distortion of the parent lattice introduced by lattice strain. In such cases, lattice correspondence and chemical order, if present, is often inherited from the parent lattice. In some cases, a "shuffle" of atoms involving displacements confined within unit cells can be accompanied by the lattice distortion. The mechanics of displacive transformations are not mutually exclusive to one another, as the product phase can be obtained from the parent phase through homogeneous lattice distortion and/or a shuffling of atoms. For example, martensitic transformation in Ti alloys involves a homogeneous lattice shear of the β phase and a shuffle of atoms in the $(110)_\beta \parallel [010]_{\alpha''}$ plane. The transformation of β ↔ ω involves a shuffle of atoms in the $\{111\}_\beta \parallel (0001)_\omega$ plane.

In a quenching scenario, whether the mechanism be a displacive or diffusion transformation may be determined by the relative positions of the composition of the alloy and the Gibbs free energy of the phases in question. Fig. 2.13 shows the schematic free enthalpy diagrams of a two-phase solid solution with phases A and B, of a quenched alloy of composition X_0. G^0 can be defined as the

intersection where the free enthalpies of the competing phases are equal for a specific composition. T^0 is the temperature at which G^0 exists at composition X_0. When quenched from the high temperature single phase B to temperatures above T^0 (Fig. 2.13b), the available pathway to decrease the overall free enthalpy is only through solute partitioning into a two-phase mixture (B → A+B). When quenched to a temperature below T^0 (Fig. 2.13c), there exists two pathways to decrease the free enthalpy of the system. One is the diffusionless displacive pathway (B → A), the second is the previously mentioned solute partitioning. Provided that the activation energy required for solute partitioning is larger than the activation energy required for the displacive transformation, and the time allowed for solute partitioning is insufficient, the system will reduce its free enthalpy through the diffusionless displacive transformation.

2.5.3. Martensitic formation

Martensitic transformation in Ti-Nb alloys is a purely displacive transformation involving the shear of the parent austenitic bcc β phase into an orthorhombic α" structure. The individual steps of the shear components required for a cubic to orthorhombic transformation is described by Ren [79] and Li [80]. Two shear components are involved in this process: first the $\{110\}_A\langle 110\rangle_A$ that transforms the cubic unit cell to a tetragonal unit cell, then a $\{100\}_A\langle 010\rangle_A$ that transforms the tetragonal to an

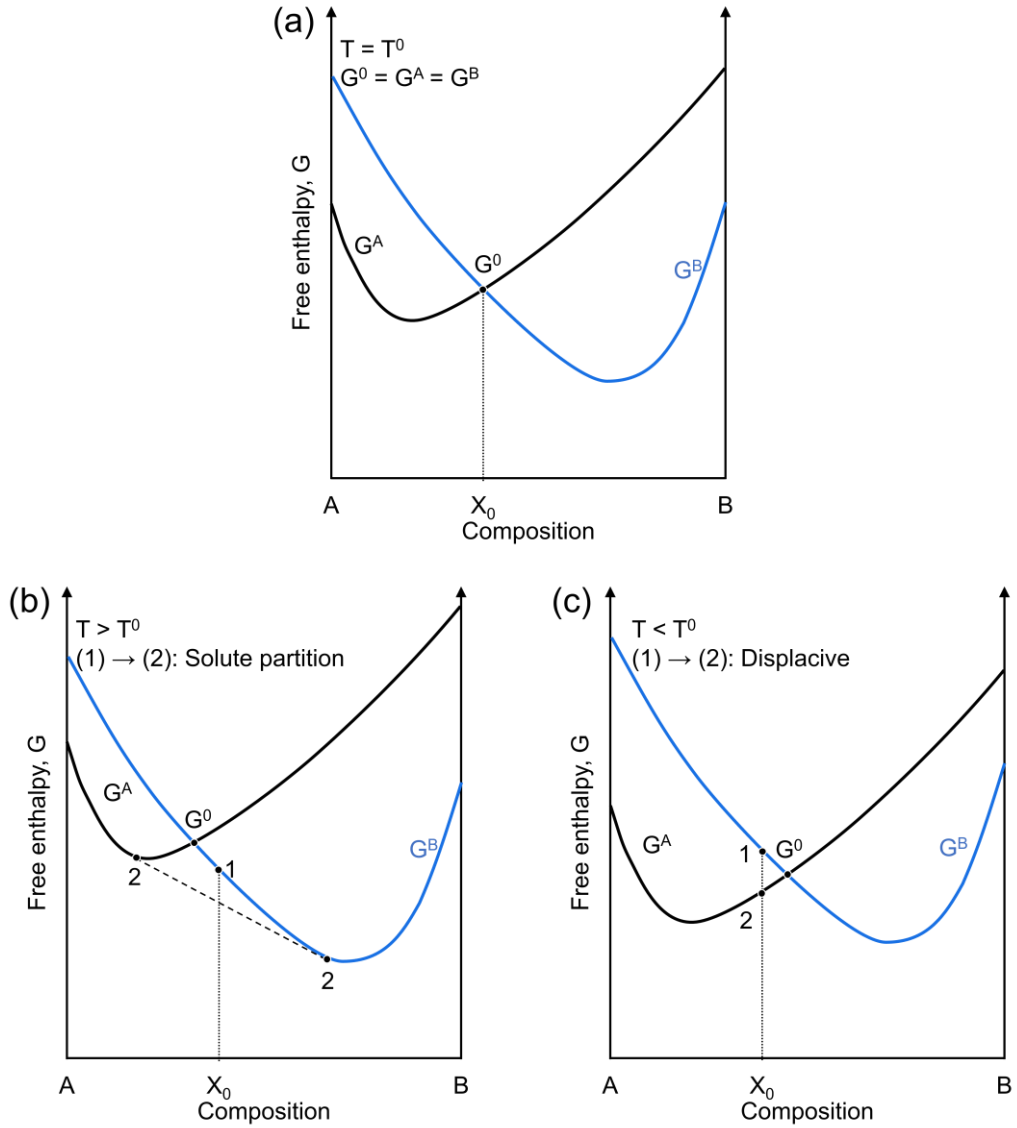

Fig. 2.13. (a) A system with a composition at the G^0 point where the free enthalpies of both phases are equal. However, this does not mean that no separation of phases will occur, since the chemical free energies are not equal. (b) The system quenched to a temperature where the composition lies to the right of the G^0 point and the system lowers its free energy through solute partitioning. (c) The system quenched to a temperature where the composition lies to the left of the G^0 point and displacive transformation is available from point 1 to 2.

orthorhombic unit cell. The *A* subscript refers to the austenite (cubic) reference axes. Since the transformation is purely displacive, the martensite inherits the composition of the parent austenite. Other than the shear of the lattice, atomic shuffles were also measured for the two atoms per unit cell in the $(002)_{\alpha''}$ plane along the $\langle 010 \rangle_{\alpha''}$ direction. This shuffle was measured to be dependent on the composition of the Ti-Nb alloy, with decreasing concentration leading to a larger shuffle distance [61].

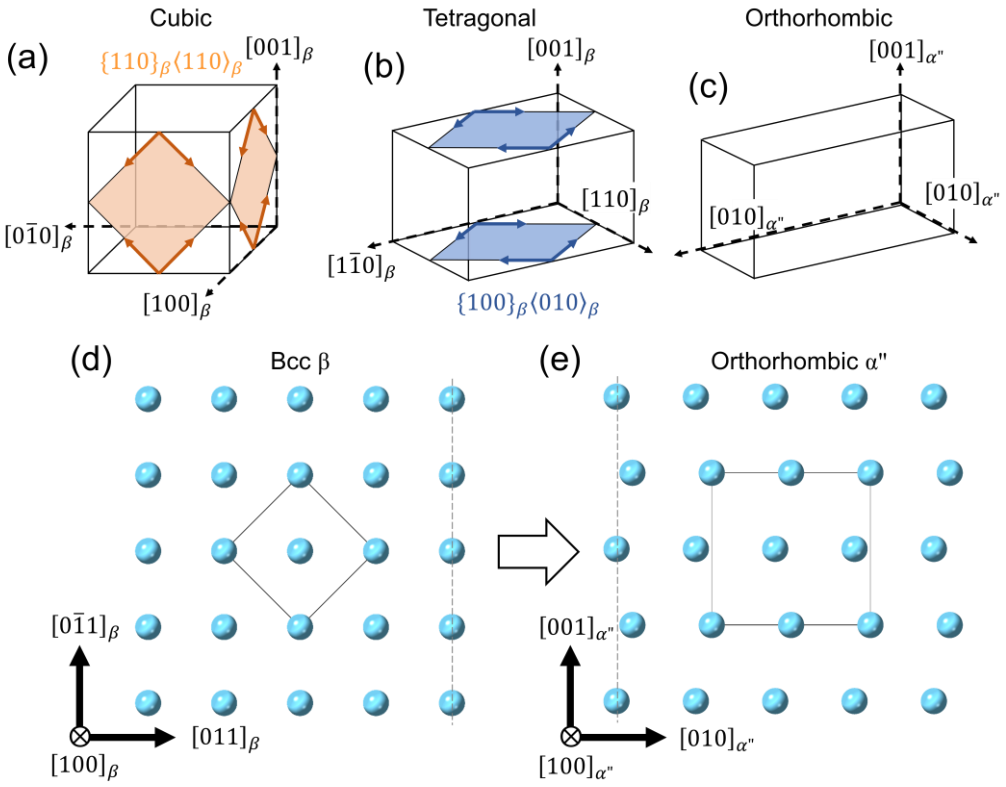

Fig. 2.14. The shear transformation undergone by (a) a cubic unit cell towards (b) a tetragonal unit cell then towards an (c) orthorhombic unit cell. The orthorhombic unit cell then undergoes a shuffle of atoms in the $(002)_{\alpha''}$ plane.

As mentioned previously, the nucleation process requires extra free enthalpy called nucleation energy to overcome the restraining factors for nucleation, the same applies for the martensitic transformation. The restraining factors in martensitic transformation involve the surface, elastic, and volume energy. Surface and volume energies are energies required to create a surface or volume of the product phase in the parent phase. The elastic energy is the energy required to distort the parent phase to allow for the formation and accommodation of the martensite with a different volume and structure. Illustrated in Fig. 2.15, these constraining energies can be provided by the difference in austenite and martensite free enthalpy obtained by undercooling the parent phase beyond the temperature where the temperature of equal enthalpy ($\Delta G^{A\rightarrow M}=0$). The temperature at which the nucleation energy is overcome and nucleation initiates is often known as the martensitic start temperature (M_s). Beyond the M_s temperature, β transforms to α" until the martensitic finish temperature (M_f) where martensitic transformation is halted. To many researchers, these characteristic transformation temperatures are often of interest, especially in Ti alloys capable of the shape memory effect. One of the methods to

measure the M_s temperature is through calorimetric measurements measuring the release/absorption of heat of the transformation. The entire process of martensitic transformation is an exothermic reaction where heat is released. The release of heat can be detected experimentally through DSC, where the start of the exothermic peak is marked as the M_s temperature, and the end of the transformation as the M_f, where the austenitic phase stops transforming into martensite. Similarly, the reversion of martensite back to austenite can be achieved through heating of the martensite past the characteristic austenite start (A_s) temperature. In an ideal thermoelastic martensitic transformation, the parent matrix is distorted elastically to accommodate the product phase, and the reverse transformation should not have a difference in temperature. However, the austenitic *start* temperature and martensitic *finish* temperature do not necessarily align due to frictional work spent on interfacial motion, energy spent on defects created during the transformation, and possibly plastic deformation for accommodation of the product phase [81].

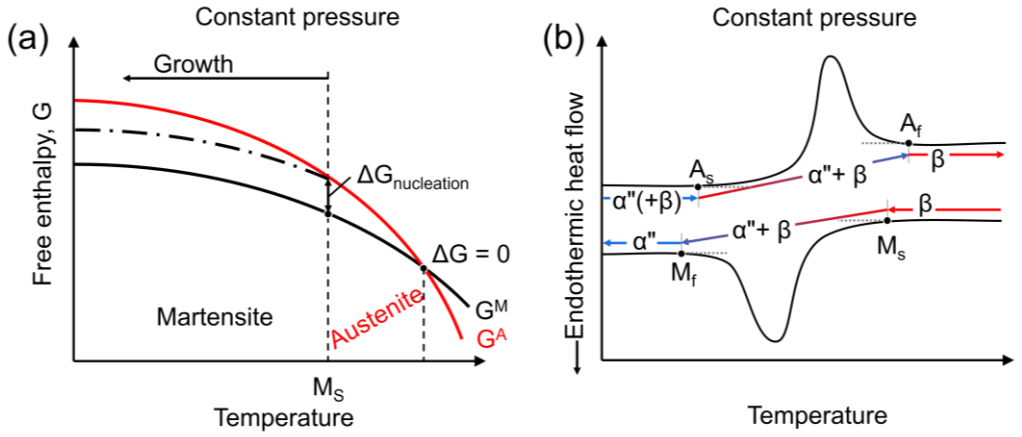

Fig. 2.15. (a) The free enthalpy curve showing the nucleation of martensite from austenite. (b) A schematic example of a calorimetric experimental result measuring the A_s, A_f, M_s, M_f temperatures of the martensitic transformation and martensitic reversion.

2.5.4. Stress induced α" phase

Other than quenching, the nucleation energy required to form martensite can be provided externally through applied stress. The application of tensile, compression, or cold-rolling leads to the deformation of the parent matrix to accommodate the externally applied stress, hence forming the stress induced martensite (SIM). Unlike the self-accommodated variants in quenching, the variant formed under stress is dependent on the variant that can accommodate the highest stress. Under

compression or tensile stress, it is common to see a "double yielding" phenomenon that is related to the formation of stress induced martensite. Fig. 2.16 shows a general schematic stress-strain curve involving the formation of SIM. Following the elastic deformation in Region I, the first yielding in Region II is seen at stress values lower than the yield strength, indicating the initiation of SIM from β. The triggering stress for SIM can be found by the intersection between the elastic deformation region and the plateau. This formation continues up to Region III where strain hardening occurs simultaneously with the continued formation of SIM. Beyond Region IV, a second yielding indicates the start plastic deformation of α"(+β). The ease of formation of SIM is said to highly depend on the β stability of the overall alloy and the grain size within the material [82-84]. As SIM is not encountered in this study, nor the composition of the alloy was varied, further details on the conditions of formation of SIM will not be discussed further.

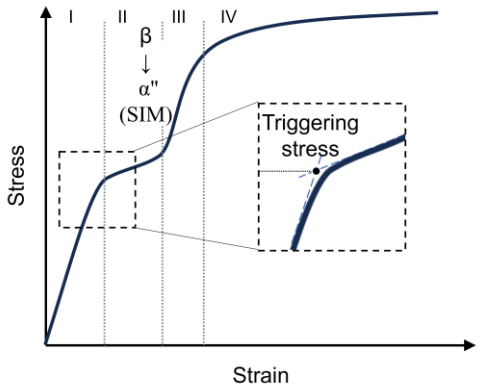

Fig. 2.16. The stress-strain curve of a Ti alloy undergoing stress induced martensitic (SIM) transformation. Region I is elastic deformation. Region II is the start of SIM transformation. Region III is continued SIM transformation and strain hardening. Region IV is yield plastic deformation.

2.5.5. Diffusion in the Ti-Nb system/ Spinodal decomposition

The high degree of metastability in β-isomorphous Ti alloys leads to multiple available precipitation pathways including both first and second (and higher) order transformations. The decomposition of metastable β occurs primarily through solute partitioning involving long range diffusional atom transport of β stabilizers and precipitation of α precipitates. The diffusion equation is commonly represented by:

$$D = D_0 \exp(-\frac{\Delta H}{RT}) \tag{2.25}$$

Where D is the diffusion coefficient, D_0 is the frequency factor (also called pre-exponential factor) and ΔH is the activation enthalpy for diffusion, T is the absolute temperature and R is the gas constant. Through Moffat's studies on the Ti-Nb system, the diffusion rates of Nb in Ti at various equilibrium compositions and temperatures have been compiled through various compiled tracer diffusion experimental data as reproduced in Fig. 2.17. It is evident that at constant temperature, the diffusion coefficient decreases with increasing Nb concentration. Unsurprisingly at constant composition, the diffusion coefficient increases, although the increase in diffusion coefficient is more rapid at lower Nb concentrations.

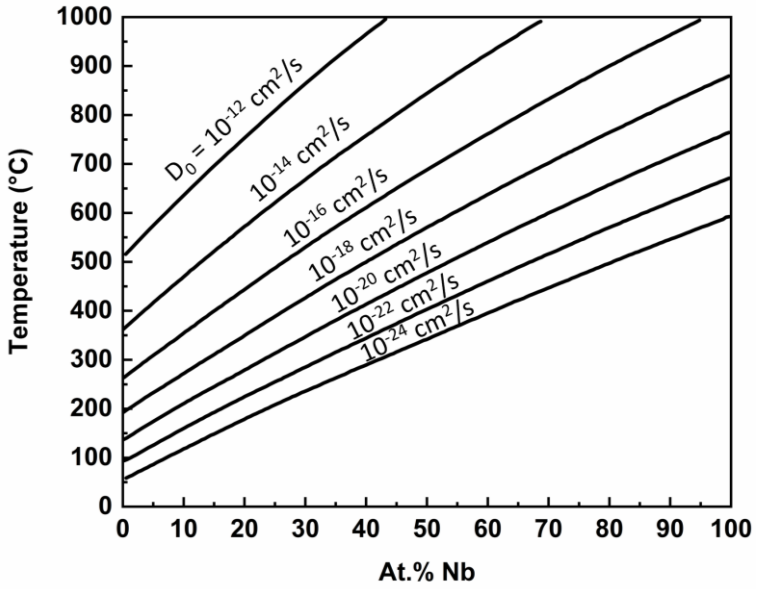

Fig. 2.17. Diffusivity of Nb in Ti at various Nb compositions. Adapted from [42] .

Other than solute partitioning, spinodal decomposition is another diffusion mechanism that is possible for metastable β-Ti alloys. A spinodal can be determined by a miscibility gap in the phase diagram, or by a spinodal free enthalpy curve as shown in Fig. 2.18a. The prominent feature of spinodal free enthalpy curves is the existence of two inflection points where the second derivative ($\frac{d^2G}{dX^2} = 0$) is zero, leading to a region of negative curvature ($\frac{d^2G}{dX^2} < 0$). When an alloy with a composition between the inflection points is quenched to room temperature, it can undergo spinodal decomposition. Spinodal decomposition has no nucleation barrier, hence, the rate of transformation is largely dictated by the

interdiffusion coefficient. An alloy within the spinodal region attempts to lower its free enthalpy by amplifying local fluctuations in composition. An example of the lowering of the free energy of an alloy with composition X_0 quenched within the spinodal region is shown in Fig. 2.18c. Within the region of negative curvature, local fluctuations marked $X_0 \pm \Delta X$ are able to form to reduce overall free enthalpy in a cascading form to eventually reach equilibrium. Precipitates formed in this matter gradually change their composition towards equilibrium composition X_1 and X_2 via diffusion in the form of a fixed wavelength as illustrated in Fig. 2.18d. On the contrary, composition fluctuations in alloy compositions outside the spinodal are unable to form this way as it would lead to an increase in overall free energy if fluctuations of $X_0 \pm \Delta X$ were formed as shown in Fig. 2.18e. Precipitates formed in alloys of this composition can only form through nucleation and growth, with precipitates having discreet X_1 and X_2 compositions as shown in Fig. 2.18f. The α" phase was described as an intermediate “compromise” low energy phase between β and α by Duerig [85] formed during the quenching process from the high temperature single β phase. Thermodynamically, the free energy curve of the α" phase was proposed to be a spinodal situated in between the α and β curves by Davis, Flower and West [86] as shown in Fig. 2.18b. This creates a scenario during the spinodal decomposition of the α" phase that the Nb lean precipitates follows a second-order transformation of continuous volume change as Nb lean precipitates gradually transform to α/α', while the Nb rich side follows a first-order transformation to β.

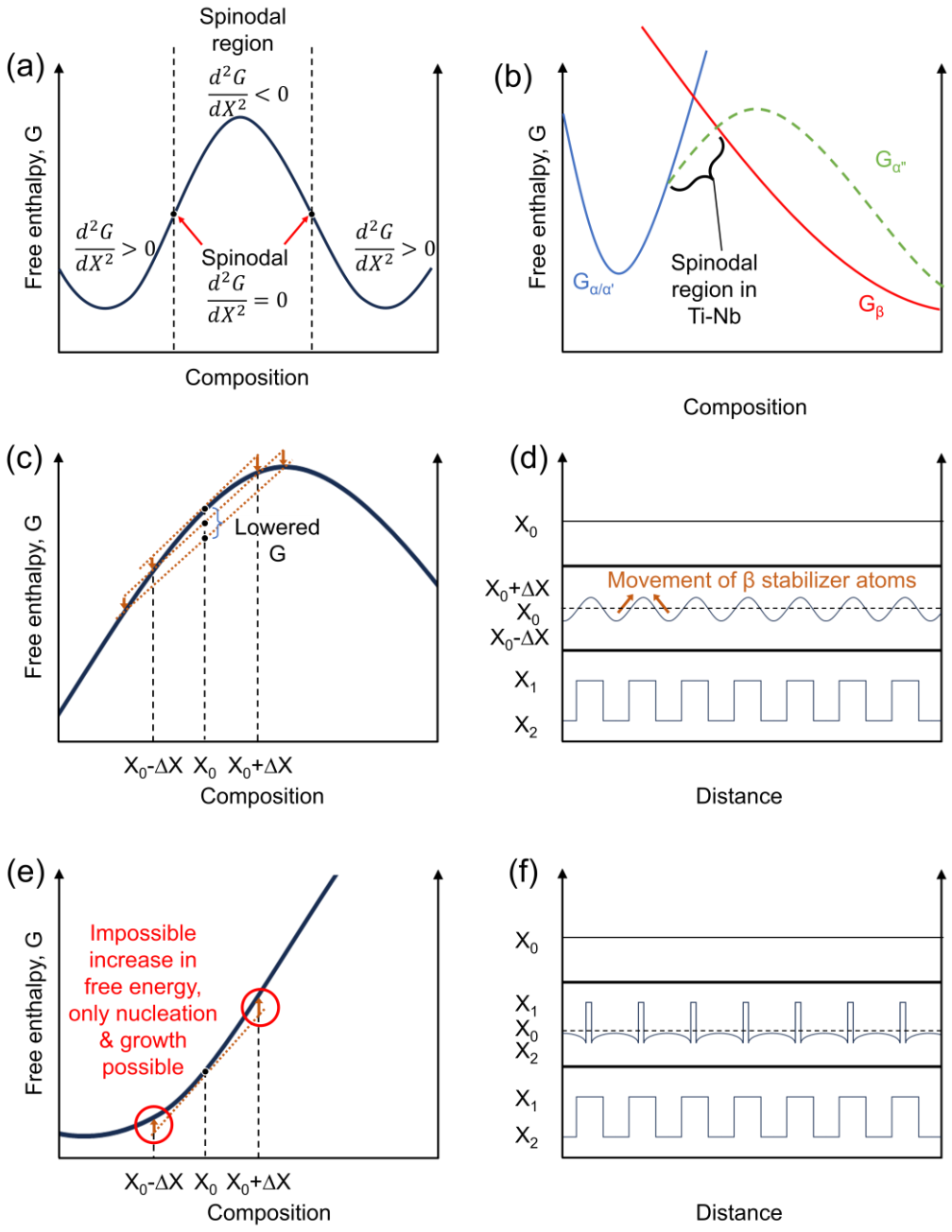

Fig. 2.18. (a) A schematic example of molar free enthalpy curves of a two-phase material with a spinodal region. (b) Compositional fluctuations within the spinodal region allows for lowering of free energy by decomposing into solute rich and lean regions. (c) The precipitation process of a system undergoing spinodal decomposition showing the amplification of initial composition fluctuations in a waveform. (d) Illustration of a system outside the spinodal region unable to amplify compositional fluctuations to lower free energy. (e) The process of nucleation and growth must occur in a system composition outside the spinodal. Distinct precipitates with X_1 and X_2 are immediately formed and then grows to expand. (f) The illustration of the spinodal free enthalpy curve of α" between α and β in Ti-Nb as suggested by Davis [87] .

Other than spinodal decomposition into the equilibrium phases, the α" phase have also been counterintuitively observed to form from isothermal diffusional processes [78, 88-90]. It is important

to note that the isothermal conditions for the formation of α"$_{iso}$ are not strictly restricted to isothermal conditions, but also include a slow change in temperature, i.e. a slow heating/cooling rate, to be qualified as an isothermal condition as evidenced by the formation of α"$_{iso}$ in studies of non-isothermal conditions [91-93]. At low heating rates, the isothermally formed α" (α"$_{iso}$) was seen to form from ω in a ω+β mixed phase. Suggested by Bönisch in the study of the free enthalpy landscape of the Ti-Nb system [2], α"$_{iso}$ is able to form as an intermediate low energy phase when ω proves to be energetically unfavourable.

2.6. Thermal expansion of phases within Ti-Nb

2.6.1. Thermal expansion of α" phase

Recently, the lattice thermal expansion of the α" phase in martensitic β-Ti alloys has been studied through diffraction experiments to reveal an anisotropic NTE along the $\langle 010 \rangle_{\alpha''}$ direction of up to 90 ppm/°C [2, 94]. Despite this, the anisotropic lattice NTE does not always translate to observable NTE in bulk β-Ti alloys. One of the reasons lies in the lattice thermal expansion of the other two principal directions, $(001)_{\alpha''}$ and $(100)_{\alpha''}$. Of these two principal directions, the latter has been reported to exhibit an incredibly positive thermal expansion of over 100 ppm/°C, while the former exhibits a very slight PTE [2, 3, 5, 91]. The second reason lies in the condition of the material. In a material of isotropic texture, the positive thermal expansion of all the directions of random grains in the material are able to mask the NTE of the $(010)_{\alpha''}$ plane, averaging to a positive isotropic thermal expansion [3, 4]. In Table 2.2, the lattice thermal expansion of a list of studied Ti alloys are compiled to visualize the effects of composition on the lattice thermal expansion. The lattice thermal expansion of the parent β phase, when available, are also provided. When looking at these compiled data, it is imperative to understand a few precursor conditions. The lattice CTE taken from these studies is the average CTE defined as:

$$Average\ CTE = \frac{\varepsilon_T - \varepsilon_0}{T - T_0} \tag{2.26}$$

Where ε_T is the strain at a specific end temperature, ε_0 is the initial strain, T is the end temperature, and T_0 is the initial temperature. While the equation assumes a linear response, the thermal strain

response of most materials, including Ti alloys, are often non-linear. The temperature range and thermal strain profile of an alloy within a specific temperature range could wildly differ to an identical alloy measured in separate temperature range. These conditions should be taken into consideration when making comparisons since the temperature range and thermal strain response of every study cannot be normalized. This is likely the case when noticing the exceedingly large discrepancy between the $(010)_{\alpha''}$ NTE between Ref [2] and Ref [3, 95], where the measured temperature ranges were not equal. Within the same studies, it can be observed that the composition largely affects the magnitude of lattice NTE exhibited. The magnitude of lattice NTE is generally seen to increase significantly with concentration of β stabilizer. Beyond that, the CTE of the $(100)_{\alpha''}$ plane increases significantly while the $(001)_{\alpha''}$ plane increases slightly with β stabilizer concentration. The inducing of texture in alloys is a known technique to alter the thermal expansion of alloys [96]. In a study of martensitic alloys with anisotropic properties by Monroe [1], cold rolled Ti-Nb alloys were found to exhibit macroscale NTE along the rolling direction. The reorientation of crystal grains within the material due to cold rolling brought about alignment of crystallographic directions, allowing the material to exhibit macroscale NTE without being affected by PTE of the other principal directions. Since then, increasingly more studies have been performed on the behaviour and extent of NTE of textured Ti alloys. The extent of texturing highly affects the macroscale NTE of the final alloy. Nakai et al. showed that the cold roll reduction of a Ti-NbTaZr alloy highly affects its ability to exhibit NTE, with high cold roll reduction exhibiting the largest NTE along the rolling direction [97]. Later, Monroe showed that cold rolling of even 20% cold roll reduction could cause a Ti-Nb alloy to exhibit NTE along the rolling direction [1], with improvements in NTE going up to 80% cold roll reduction. Other than cold rolling, inducing texture through axial tension can also lead to macroscale NTE in the alloy. A study from Gehring on tensile pre-strained Ti-Nb alloys showed that the same trend can be found with higher pre-straining leading to higher NTE [3]. One outlier in Gehring's study showed that pre-straining did not affect the macroscale NTE of Ti-15Nb (at.%). This was discussed that the deformation mode of Ti-15Nb (at.%) at this composition triggered dislocation plasticity before grain reorientation, thus failing to exhibit macroscale NTE. This further highlights the importance of imposing texture in martensitic β-Ti alloys for NTE. The plausibility of the aforementioned stress

induced martensite to simultaneously form in a preferred orientation and exhibit NTE have also been documented in many alloys, most noticeably in Ti-NbTaZr alloys [97-102]. However, stress induced martensite has not been encountered in this study thus it will not be discussed.

Table 2.2. Compilation of lattice thermal expansion of Ti-Nb based alloys.

Alloy (at.%)	Phase, crystal system	Deformation (%) /Condition	Temperature range (°C)		Lattice CTE (ppm/°C)			Ref
			T_{min}	T_{max}	a	b	c	
Ti-Nb15	α", orth	0	-173	277	~33.8	~ -26.9	~2.05	[3]
Ti-Nb20	α", orth	0	-150	210	~40.3	~ -26	~ 8	[3]
Ti-Nb22	α", orth	0	-173	102	~46.8	~ -29.7	~7	[3]
Ti-Nb24	α", orth	0	-170	90	~36.8	~ -39		[3]
Ti-Nb8.9	α", orth	0	50	600	25.7	4.7	10.6	[2]
Ti-Nb12	α", orth	0	50	510	47.2	-20.9	6.9	[2]
Ti-Nb17	α", orth	0	50	315	81.4	-60.6	5.1	[2]
Ti-Nb22.5	α", orth	0	50	310	163.9	-95.1	24.4	[2]
Ti-Nb22.5	β, bcc	0	50	305	27.9			[2]
Ti-Nb20	α", orth	0	-170	20	37	-26		[103]
Ti-Nb20	β, bcc	0			10			[103]
Ti-Nb19.5	α", orth	0	-190	20	37	-26		[95]
Ti-Nb19.5	β, bcc	0			10			[95]
Ti-Nb24	α", orth	0			39	-36		[95]
Ti-Nb24	β, bcc				16			[95]
Ti-Nb15-Zr2.6-Sn4	α", orth	6% pre-strain	25	300	70.4	-22.3		[104]
Ti-Nb15-Zr2.6-Sn4	β, bcc				1.5			[104]
Ti-Al5.3-V4.7-Mo2.25	α", orth	Quenched 780°C	40	100	81	-37	-8	[15]
Ti-Al5.3-V4.7-Mo2.25	α", orth	Quenched 800°C			53	-27	7	[15]
Ti-Al5.3-V4.7-Mo2.25	α", orth	Quenched 820°C			45	-14	-1	[15]
Ti-Mo4.2	α", orth	0	40	350	39	-19	6	[105]
Ti-Mo1.5-Al10.3	α", orth	0	40	300	18	1	7	[105]

Alloys sampled from literature are mostly at 0% deformation for a meaningful comparison. The lattice CTE values quoted from Gehring [3] were approximated from the figures published, namely Figure 11a from the mentioned article. The CTE value for the c-axis was not visibly seen in said figure and is left blank. The temperature range at the onset of α-β transformation from Elmer [106] was not stated and was roughly approximated from figures. The CTE c-axis value of the hcp lattice was not reported from Elmer as well and intentionally left blank.

The origin of the intrinsic lattice NTE property in martensitic shape memory alloys has been explained theoretically by Li. The martensitic thermal strain response modelled as an interaction between the intrinsic cubic lattice thermal strain and temperature dependent transformation strain resulted in the NTE movement of minimum free energy positions of atoms in martensitic shape memory alloys, which includes Ti-Nb and several shape memory β-Ti alloys.

2.6.2. Thermal expansion of α, β and ω phase

The thermal expansion of a material is a contribution of all coexisting phases within the material. Hence, it is also imperative to envision the thermal expansion of the other equilibrium and non-equilibrium phases within the β-isomorphous Ti system. In this section, the thermal expansion of β, ω and α phases are presented and lightly discussed. Table 2.3 presents the lattice thermal expansion of α and β elemental Ti and TiH are shown. Lattice thermal expansions for the equilibrium phases do not vary much across a wide temperature range. The α phase has been reported to also exhibit anomalous thermal expansion with NTE along the c-axis at very low temperatures below 160K by Souvatsiz [107], but otherwise exhibits regular thermal expansion above. Available data for lattice thermal expansion of the ω phase is very limited. Among the few studies that have displayed figurative data for the thermal strain response of ω, it can be observed that the lattice parameters of ω do not change drastically until the cusp of phase transformation, such as reversion to α or β. A study by Zháňal [108] on Ti-Mo alloys showed that the lattice parameter a_ω and c_ω displayed a general trend of decreasing and increasing with temperature respectively. However, none of these studies have reported the actual value of lattice CTE for the ω phase [91, 92, 108]. While it is possible to estimate from the figures in the aforementioned studies, the scatter of the data and inaccuracies would make it disingenuous.

Table 2.3. Compilation of lattice thermal expansion of the equilibrium phases in Ti systems.

Alloy (at.%)	Phase, crystal system	Deformation (%)	Temperature range (°C)		Lattice CTE (ppm/°C)			Ref
			T_{min}	T_{max}	a	b	c	
Ti	α, hcp	0	28	155	9.5		5.6	[109]
Ti	α, hcp	0	0	600	9.55		10.65	[110]
Ti	β, bcc	0	900	1070	12.0			[110]
Ti	β, bcc	0	900	1000	13.8			[111]
Ti-6Al-4V	α, hcp	0		Approx. <500	9.7			[106]
Ti-6Al-4V	β, bcc	0		Approx. <400	9.2			[106]
Ti-6Al-4V	β, bcc	0	Approx. >700		58			[106]
Ti-8H	β, bcc	0	820	960	13.4			[111]
Ti-19H	β, bcc	0	720	920	13.2			[111]
Ti-23H	β, bcc	0	720	920	13.3			[111]
Ti-29H	β, bcc	0	560	820	13.2			[111]

2.7. Thermal stability of α" phase

A significant property to deliberate when employing martensitic Ti alloys for its NTE property is the thermal stability of the responsible martensitic phase. The temperature range that the martensitic phase can exist stably without decomposing via diffusive or displacive pathways to the equilibrium phases determines the maximum working temperature without the deterioration of NTE. As mentioned before, heating of martensite above the A_s temperature can lead to a displacive reverse martensitic transformation (or martensitic reversion) of α" to β, reducing α" phase fraction and resulting in a loss of NTE. At elevated temperatures with a low heat rate, or at isothermal conditions with sufficient time, the α" phase can also decompose into stabilizer rich and lean components, eventually leading to a duplex phase alloy.

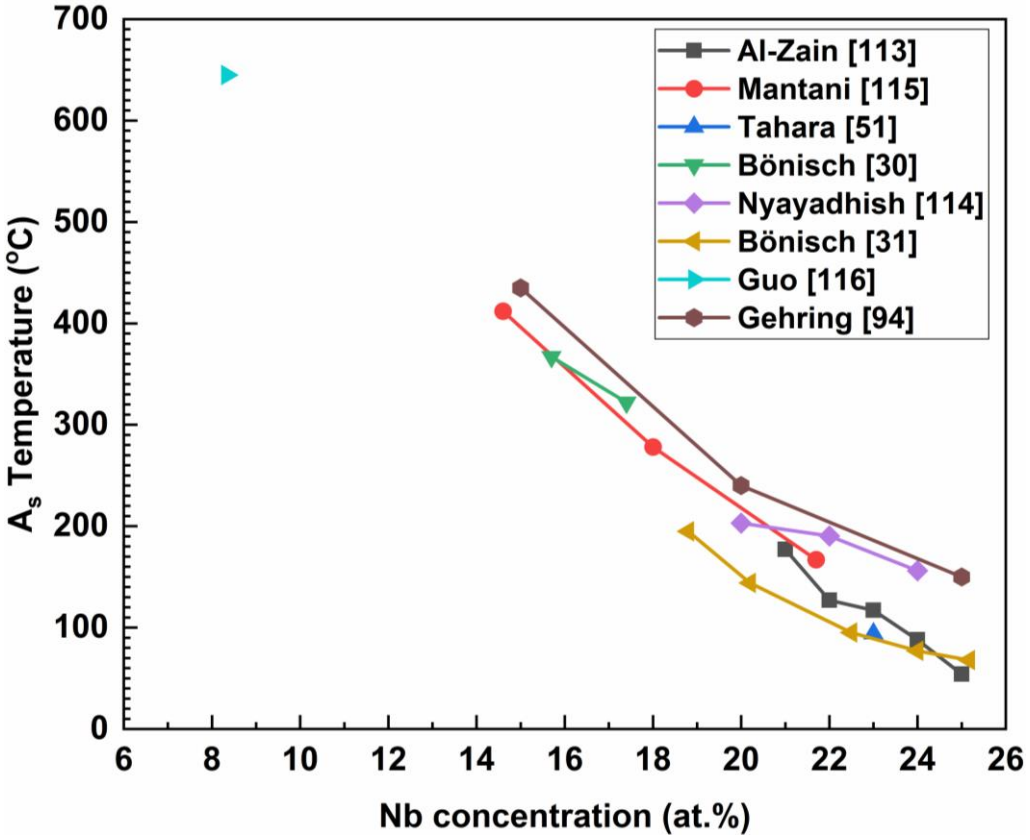

Fig. 2.19. Compilation of A_s temperatures of various literatures.

The As temperature of Ti-Nb alloys with respect to Nb concentration is shown in Fig. 2.19 [30, 31, 51, 94, 112-116]. It is evident that with increased β stabilizer content, the amount of thermal energy required for reverse martensitic transformation is lowered, resulting in a less stable α" and a more stable β phase. The thermal stability of α" also manifests in the dimensions of the α" unit cell at any given temperature, and the thermal strain response of the unit cell. In a series of studies by Bönisch [30, 31] studying the phase transformations of a wide composition of martensitic Ti-Nb alloys, an evident correlation is found between the mentioned factors. It was previously mentioned that the α" phase is thermodynamically an intermediate phase between α and β, but this description also applies to the shape of the unit cell. The likeness of the α" unit cell towards β is often described using the edge ratios: $\frac{b_{\alpha"}}{a_{\alpha"}}$ and $\frac{c_{\alpha"}}{a_{\alpha"}}$, where $a_{\alpha"}, b_{\alpha"}, c_{\alpha"}$ are lattice parameters of α". Perfect likeness of an α" unit cell towards β is reached when $\frac{b_{\alpha"}}{a_{\alpha"}}$ and $\frac{c_{\alpha"}}{a_{\alpha"}}$ are at √2, and an α" unit cell with a higher β stabilizer concentration pushes the edge ratio towards √2 at a fixed temperature. The edge ratios of the α" unit cell also trends towards √2 with increasing temperature, showing gradual gravitation towards the bcc

unit cell approaching the A_s temperature. The rate at which this progression towards the bcc edge ratios is more rapid in α" of higher β stability, leading to an exhibited increased NTE along $\langle 010 \rangle_{\alpha''}$ and increased PTE along $\langle 100 \rangle_{\alpha''}$ and $\langle 001 \rangle_{\alpha''}$. Ultimately, a Ti-Nb alloy with lower Nb content would give a more thermally stable α" with a higher A_s temperature, but exhibit weaker lattice NTE and as a result, a weaker macroscale NTE. Although the trade-off appear to be between selecting a lower Nb content for higher thermal stability and lower NTE or the reverse, as pointed out by Gehring [3], a Ti-Nb alloy of lower Nb content would reach thermal strains equivalent to that of a higher Nb content if given a high enough temperature.

One of the key traits of diffusive metastable phase transformations is the time dependency of the process. Given enough time for long range diffusive atomic transport to take place after the thermal energy requirement has been met, the previously mentioned spinodal will separate into stoichiometrically different Nb lean and rich phases and eventually at the end of the Nb rejection process, α''_{lean} turns into α and α''_{rich} into β phases [2, 77, 78]. However if the heating rate is quick enough, the diffusive step could be skipped altogether as reported by Barriobero [91] and Settefrati [117]. In these studies, athermal martensitic reversion occurs at a much higher rate at high heating rates compared to the rate of decomposition, resulting in a much more rapid consumption of the α" phase. Under appropriately low heating rates, diffusional composition of α" phase into duplex α+β structure was observed through diffusional and microstructural observations. Conversely, a heating rate high enough to skip over diffusional decomposition depends on the kinetics of the alloy at that composition. In a study by Bönisch [31], Ti-Nb alloys of 18.8-20.2 at.% Nb experienced concurrent martensitic decomposition and martensitic reversion at heating rates as high as 100 K/min, resulting in a β+α"+α mixed phase from a purely martensitic phase. This pushes the need to strengthen our current understanding of the free enthalpy landscape to predict diffusional and displacive phase transformation pathways in Ti-Nb alloys [40].

3. Experimental details

3.1. Experimental aim and procedures

This chapter presents the steps taken for the material synthesis, sample preparation and characterization methods used in the study of thermal stability, mechanical properties and phase transformation pathways of cold-rolled Ti-22Nb (at.%) alloy. Conditions under which the experiments were conducted are also described in detail.

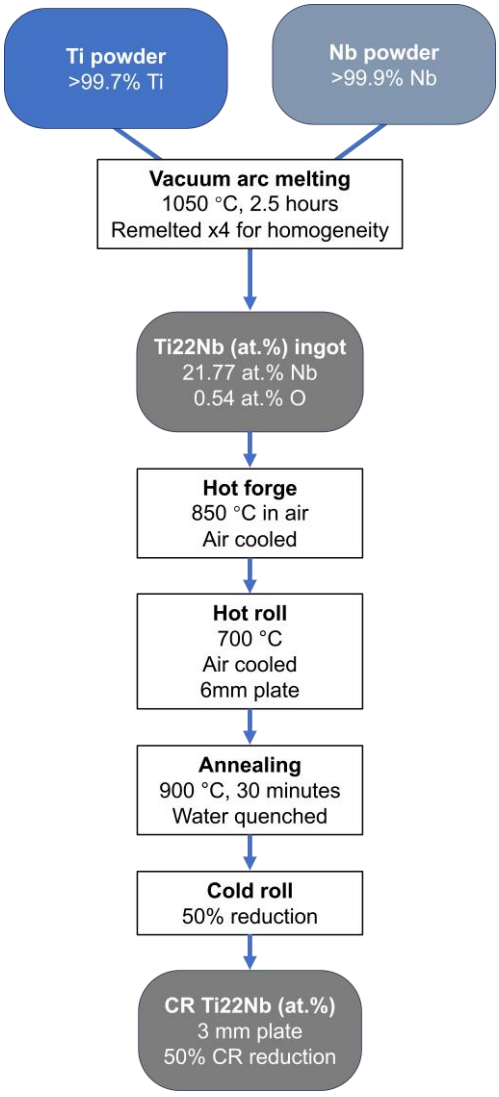

Fig. 3.1. Process diagram for the synthesis of cold-rolled Ti-22Nb sample for the use of thermal expansion studies.

3.2. Material synthesis

Fig. 3.1 shows the process for synthesizing the two reference Ti-Nb states for this thesis, namely the water-quenched (WQ) and cold-rolled (CR) states. The raw materials used to synthesize an ingot of Ti-Nb were Ti sponges of grade MHT-100 following the standard GB/T2524-2002 and Nb powders with purity of >99.9% purity with 0.005% C and 0.14% O. To achieve a the target of 22 at.% Nb, the weight of Nb powder required was calculated using the atomic weight of Ti and Nb at 47.87 and 92.9 respectively using Equations (3.1 and (3.2. The weight fraction of Nb powder used in the synthesis was 35.38 wt.%.

$$Atomic\ weight\ of\ element\ A\ in\ 1\ mol\ of\ Ti22Nb\text{: } \frac{(at.\%\ of\ A)(Atomic\ weight\ of\ A)}{100} \quad (3.1)$$

$$Weight\ \%\ of\ element\ A = \frac{Weight\ of\ element\ A\ in\ 1\ mol}{Total\ weight\ of\ all\ elements\ in\ 1\ mol} \times 100 \quad (3.2)$$

Vacuum arc melting was used to melt the raw materials at Shanxi Key Laboratory of Biomedical Metal Materials, Northwest Institute for Nonferrous Metal Research. The ingot was remelted four times to achieve homogeneity. Chemical and gas analysis of the final ingot indicated Nb and O contents of 21.77 at.% and 0.54 at.% respectively. The final composition of the alloy is acceptable due to minimal effect on the A_s temperature according to Fig. 2.19. A reduction of 0.23 at.% Nb would result in an increase of A_s temperature that is smaller than the spread of reported experimental data in said figure. The phase composition of the alloy would still be fully martensitic according to the phase diagram (Fig. 2.2). Theoretically, the NTE of Ti-21.77Nb would be slightly lower in magnitude than the targeted Ti-22Nb. The ingot was further homogenized through annealing at 1050 °C for 2.5 hours in vacuum, then forged to a thick plate at 850 °C in air and hot rolled to 6 mm in thickness at 700 °C. The sheet was then annealed at 900 °C for 30 minutes and water quenched. This forms the WQ reference state of this study. The oxide layer of the quenched plate was removed through mechanical polishing before cold-rolling with a thickness reduction rate of 50% to 3 mm. This produces the CR reference state for this study.

3.3. Experiment workflow

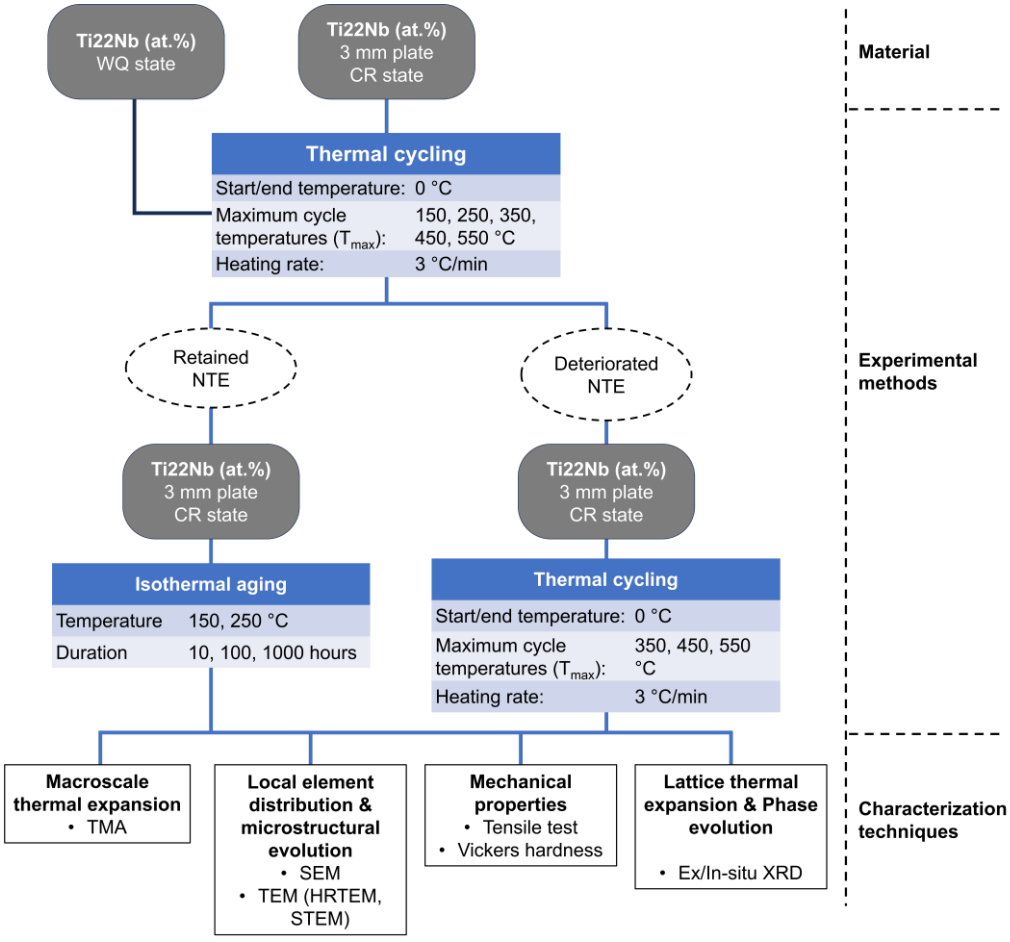

Fig. 3.2. Workflow of experiments done on Ti-22Nb in this study.

The goal of this study was to investigate the changes in NTE behaviour of CR Ti-22Nb (at.%) alloy at temperatures elevated above the A_s temperature. The experiment overview and workflow are illustrated in Fig. 3.2. To date, majority of studies on the NTE of textured Ti-Nb alloys report its thermal expansion behaviour below its A_s temperature. Hence, the retained thermal expansion of the CR samples after thermal cycling to maximum temperatures of 150, 250, 350, 450, 550 °C were characterized in Chapter 0. Successive increments in maximum temperature of 100 °C from 150 °C up to 550 °C were deemed appropriate to instigate distinct changes in thermal expansion, microstructure and mechanical behaviour to study. The NTE of the alloy along RD was expected to deteriorate with increasing temperatures as the deterioration of martensite takes place and the mechanical behaviour to change with the formation of the metastable ω phase and stable α and β phases. In Chapter 5, thermal stability experiments were conducted by isothermally aging the CR samples at temperatures where

NTE was retained after thermal cycling for 10, 100, 1000 hours to characterize the change in NTE behaviour over time and the causes behind it. Similarly in Chapter 6, the phase transformation sequence in a single heating cycle scenario leading to rapid loss of NTE was examined. In these experiments, the macroscale thermal expansion was measured through thermomechanical analysis (TMA). For the cold-rolled samples, care was taken to carefully measure the macroscale thermal expansion along all principal directions in reference to the direction cold-rolling was performed, namely the rolling direction (RD), transverse direction (TD), and normal direction (ND). In-depth crystallographic information like the lattice scale thermal expansion, overall phase constitution and phase stabilizer concentration were collected by a combination of ex-situ and in-situ X-ray diffraction (XRD). The local element distribution of precipitates in the sample were characterised using energy dispersive X-ray (EDX) coupled with scanning electron microscopy (SEM) or transmission electron microscopy (TEM) depending on the dimensions of the precipitates. These imaging techniques also allowed us to visualize the microstructural evolution of the precipitates after heat treatment at successive temperatures. More detailed microstructural information such as the orientation of precipitates were captured using an electron backscattering diffraction (EBSD) attachment on SEM. Furthermore, mechanical properties such as tensile and hardness tests were conducted to reveal properties such as ductility, Young's modulus, ultimate tensile strength, and Vickers hardness to uncover supporting evidence of nucleated phases and precipitates within the sample.

3.4. Isothermal aging

Isothermal aging of the CR samples was conducted in a resistively heated bath. For isothermal aging at 150 °C, a mineral oil bath was used; for aging at 250 °C, a bath of melted tin was used to prevent carbonization of the mineral oil bath at this temperature and risk oxidation of the sample. Smaller CR sheets of dimensions of 80 × 20 × 3 mm^3 were first cut using electro discharge machining (EDM) and then submerged into the bath for 10^n (n=1, 2, 3) hours after the bath reached the desired temperature. The submerged sample was supported by a suspending wire rack to prevent contact with the surface of the resistive heated container walls which would be at higher temperature than the heated medium.

At the end of the aging process, the samples were removed and allowed to air cool. Before conducting any experiments with the aged samples, the surface of the aged samples was grinded to remove any possibility of contamination or formation of unwanted compounds.

3.5. Thermomechanical Analysis (TMA)

For the unaged samples, larger sheets of the WQ and CR sample were first cut from the bulk CR sheet using an abrasive SiC wheel saw cooled with a water-based coolant, then cut to smaller pieces using a Struers Accutom-50 precision saw cutter cooled under a water-based coolant. For the textured samples, cuts were meticulously ensured to be perpendicular to the RD, TD, and ND. The dimensions of the sectioned TMA samples are listed in the table below:

Table 3.1. Dimensions of samples used in this study as sectioned by EDM.

Sample condition	Dimensions (mm)		
WQ	8	10	3
CR	8* (RD)	10 (TD)	3 (ND)
CR	8 (RD)	8* (TD)	3 (ND)
CR	8 (RD)	10 (TD)	3* (ND)
150 °C aged	8* (RD)	10 (TD)	3 (ND)
250 °C aged	8* (RD)	10 (TD)	3 (ND)

The measured direction of interest is marked with an asterisk (*), and the direction associated with cold-rolled samples are in parentheses.

Sample faces perpendicular to the direction of interest were grinded up to a grit of P1200 to ensure both faces were perpendicular to said direction and parallel on both ends. The initial dimension of the sample along the direction of interest were measured using a Mettler Toledo TMA/SDTA841e by heating in air using the in-built furnace and cooled using a controlled stream of liquid nitrogen at a

constant rate of temperature change of 3 °C per minute from a start and end temperature of 0 °C up to a maximum temperature of 150 + 100n °C (n = 0-4).

3.6. Tensile testing

Dog-bone shaped tensile test specimens were machined from the CR sheet by EDM following the GB/T 228.1-2021 standard with the tensile axis parallel to the RD direction. This testing standard has been accepted by credible peer reviewed journals [118, 119]. Both faces of the specimen were wet grinded to a grit of P1200 to meet the thickness specification. An Epsilon Technology axial extensometer model 3442-015M-100M-ST was used was used to measure the deformation experienced by the sample. The tensile tests were performed on a Tesmart E6.304-L tension testing machine with a speed of 0.1 mm/s. The ductility of the sample was obtained at the point of fracture, and the ultimate tensile strength was obtained as the highest stress achieved, both being computed through tensile analysis.

3.7. Young's modulus characterization

The Young's modulus of the samples used in this study were measured using the resonance method following the standard ISO-12680 with a Nihon Techno-Plus JE-RT instrument. The samples used were electro-discharge machined to dimensions of 60 × 10 × 3 mm^3 and mechanical ground to a grit of P2000.

3.8. Vickers Hardness

Vickers hardness measurements were conducted on the RD face of the aged and thermally cycled samples. These faces were extracted using the precision saw cutter at 2 mm thickness, mechanically ground to a grit of P2000 and polished using the techniques described in Section 3.9.1. The measurements were taken using a Wolpert VICKERS 430SVA at a load of 1N and a dwell time of

30s. Indentations were made at eight locations evenly distributed across the width of the sample and at least 2.5 indent diagonals away from each other as recommended in ASTM E92-17 and ISO 6507-1:1997 for Vickers hardness testing.

3.9. Microstructural characterization

3.9.1. SEM/EBSD

Samples for metallographic investigations were prepared by cutting a section perpendicular to the RD direction of dimensions: 2 mm along RD, 10 mm along TD, and 3 mm along ND using a Struers Accutom-50 precision saw cutter cooled under a water-based coolant. The faces were then wet grinded with increasingly higher grit to P3000. The sample was cleaned in an ultrasonic bath filled with pure ethanol then polished using a mixture consisting of 20 vol.% hydrogen peroxide and 80 vol.% colloidal silica (SiO_2) suspension until none or minimal imperfections and no microstructural features were observed under an optical microscope. The polished sample was then further vibration polished with a suspension of 20 vol.% colloidal silica suspension for 8 hours to remove surface residual stresses imparted during grinding and polishing. For EBSD characterization, an additional step of ion polishing was done to further improve surface flatness and remove any micro damage from the previous grinding or polishing steps that could affect the collection of grain orientation data. The SEM machine used was a Carl Zeiss sigma 500 microscope equipped with an Oxford Symmetry S2 EBSD detector and an Ultim Max energy dispersive X-ray spectroscopy (EDS) detector.

3.9.2. TEM

Sections of faces perpendicular to RD were cut in an identical method as in the previous section. The samples of 2 mm along RD were mechanically grinded to 0.1 mm at a grit of P2000 and cleaned in an ultrasonic ethanol bath to remove any particles on the surface. Specimens of 3 mm in diameter were cut using a circular punch and subjected to twin jet electropolishing with a mixture of 5 vol.% perchloric acid, 35 vol.% butyl alcohol and 60 vol.% methanol at sub-zero temperatures cooled by liquid nitrogen. The electropolishing process was stopped as soon as light was detected to shine

through the sample. TEM was performed using a FEI Talos F200S G2 field emission TEM with an acceleration voltage of 200 kV.

3.10. Ex-situ, in-situ XRD

Sample preparation method of XRD samples were identical to samples prepared for metallographic analysis detailed in Section 3.9.1. The XRD machine used was a Rigaku Smartlab XE in a Bragg-Brentano geometry fitted with a Cu target, unless otherwise specified, of wavelength $K\alpha_1$ = 1.540593 Å, $K\alpha_2$ = 1.544414 Å. The instrumental broadening profile was first collected using a known standard Si sample in powder diffractometry. For the in-situ diffraction experiments, a custom machined stage was used to house the sample in vacuum. The stage was fitted with resistive heating coils and liquid nitrogen cooling pipes under a silver coated stage, and a shroud made of polyimide was constructed around the sample to allow X-rays to pass through unaltered, while providing structural integrity to maintain a vacuum. Due to the limited thickness of the CR sample at 3 mm, three identical samples sectioned parallel were aligned side-by-side to provide enough surface area for the X-rays to diffract. Real-time temperature of the sample was measured through a thermocouple on the surface of the sample and a thermocouple built under the stage, and the average of the two thermocouples were taken as the temperature of the sample.

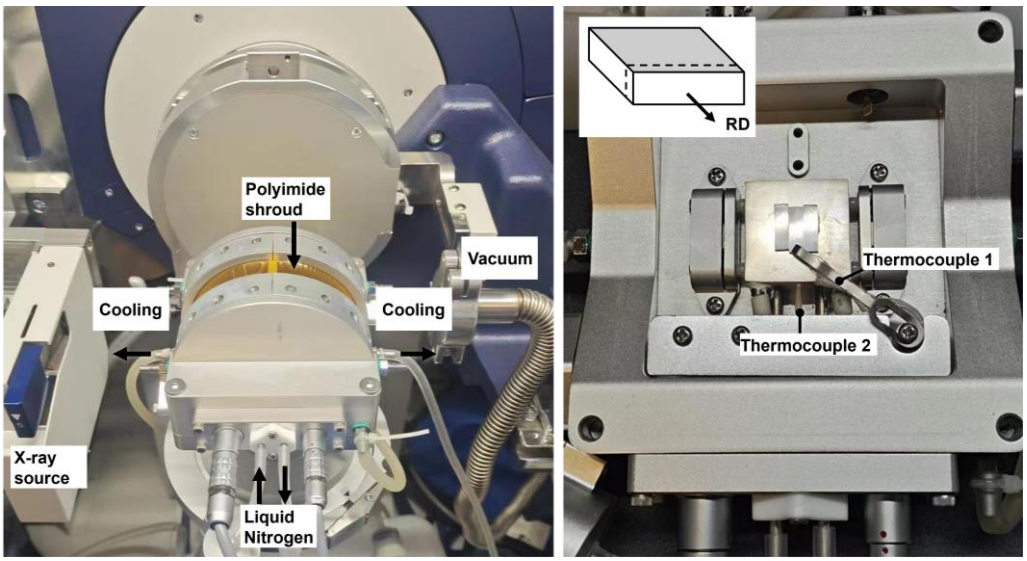

Fig. 3.3. In-situ XRD set-up with a heating-cooling stage and vacuum shroud.

A step size of 0.005° and a scan speed of 6 °/min were used in the in-situ scans. A slow scan speed would create a notable difference in the temperature at the start and end of the scans. Hence, a balance of scan speed and accuracy was achieved through trial and error. Ex-situ room temperature XRD scans utilized the same step size, but a scan speed of 3 °/min.

4. Behaviour of macroscale NTE of cold-rolled Ti-22Nb alloy through heating

4.1. Introduction

β Ti alloys are well known for their unique functional mechanical properties such as superelasticity and shape memory effect. However, only recently has the value of the anisotropic lattice NTE of the orthorhombic α" phase been recognized and studied [1, 3]. Despite several studies displaying the alloy's ability to translate NTE on a lattice scale to a polycrystalline (macro) scale, knowledge of the thermal expansion behaviour of the alloy at temperatures especially above the A_s temperature are lacking, as conservative studies have mostly reported NTE behaviour within the fully martensitic temperature region. A clear grasp of the material's NTE across a wide spectrum of temperatures is required for the evaluation of the material's potential engineering utilization. In this chapter, the NTE behaviour of a cold-rolled Ti-Nb alloy was studied across a wide temperature range above A_s temperature to establish aspects for further study in the following chapters according to the exhibited thermal expansion characteristic at specific temperatures.

4.2. Results

4.2.1. X-ray diffraction

Firstly, the compositions of the reference WQ and CR specimens were verified through ex-situ XRD and provided in Fig. 4.1 in a wide-angle scan between 2θ of 30-90°. Peak positions of the WQ diffraction pattern follow the calculated diffraction pattern of single α" phase with the *Cmcm* space group. The lattice parameters for Ti-22Nb were estimated using the lattice parameters a = 3.166 Å, b = 4.854 Å, c = 4.652 Å of a Ti-20Nb (at.%) sample by Brown et al. [120] combined with the extrapolated change in lattice parameter per at.% Nb by Kim and Miyazaki [121] of Δa = +0.01364 Å, Δb = -0.01564 Å, Δc = -0.00238 Å per at.% of Nb. Evidently, more distinguishable peaks can be observed in the WQ than CR state due to the textured condition of the CR sample caused by deformation and reorientation of grains from the cold-rolling process. Plastic deformation from cold work reorients the originally self-accommodated α" grains in the WQ condition into a preferred

orientation in order to accommodate the cold-rolling stresses. The result is a large fraction of grains with a preferred orientation, skewing the number of planes that could satisfy Bragg's law and diffracting an incoming X-ray, resulting in preferentially diffracted peaks. In the case of Ti-Nb alloys, the preferred orientation with increasing deformation has been studied. The preferred orientation of $[010]_{\alpha''}$ parallel to the rolling direction was shown to develop and increase in intensity with increased stress [3, 122]. This coincides with the increased peak intensity of $(020)_{\alpha''}$ and diminished intensity of other peaks compared to WQ seen in Fig. 4.1b.

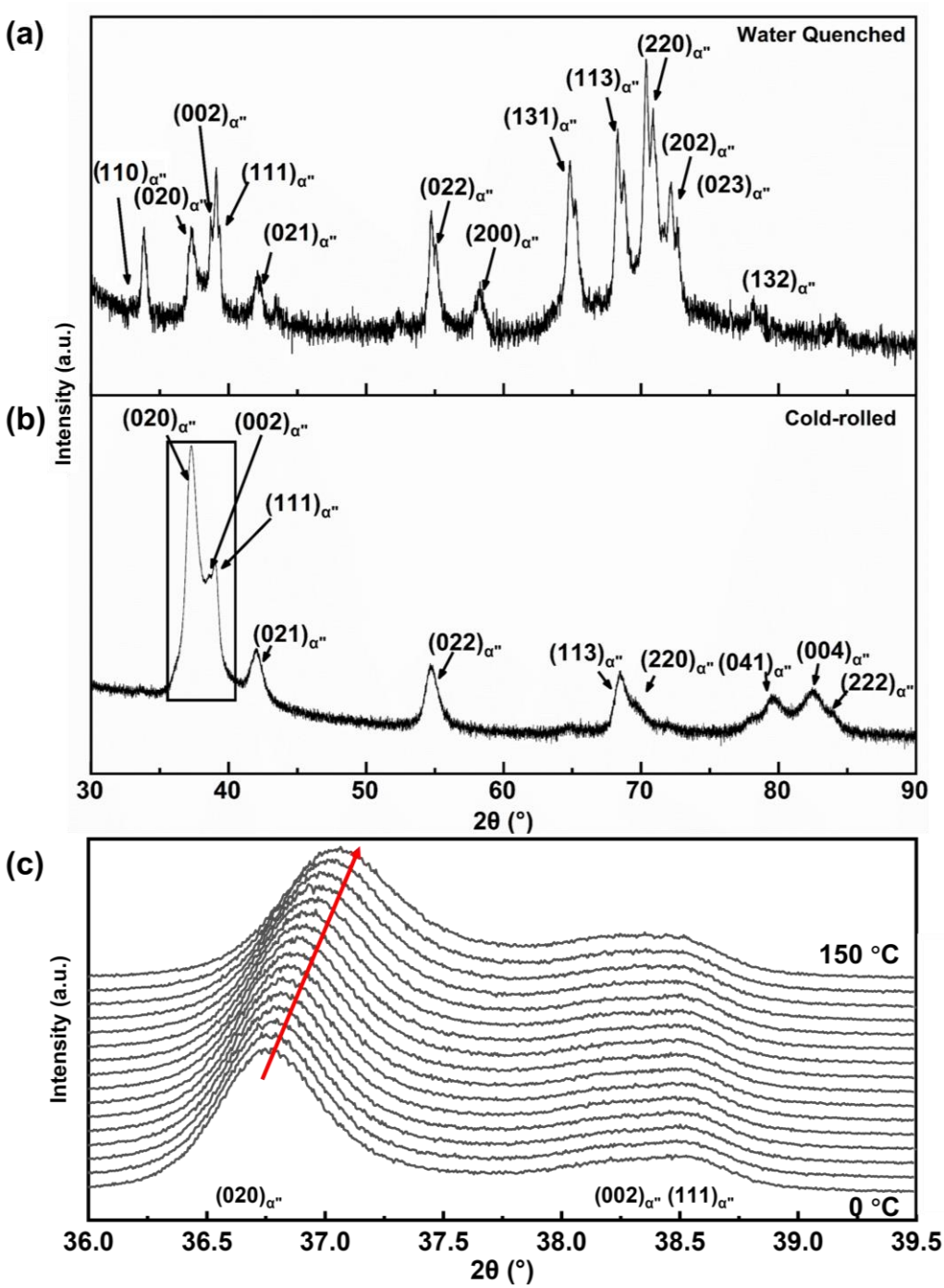

Fig. 4.1. Wide range XRD scan of Ti-22Nb (a) WQ and (b) CR sample with indexed peaks. (c) The in-situ XRD pattern of the boxed area from (b) heated from 0 °C to 150 °C.

4.2.2. Analysis method of XRD patterns

In-situ XRD was used to provide insight on the evolution of phase composition through the change in peak position and intensity. Using these diffraction patterns, lattice thermal expansion can be

calculated by calculating the change in unit cell lattice parameters between every in-situ heating diffraction pattern. The unit cell lattice parameters can be obtained with the following methods:

1) **Rietveld refinement.** Under the condition of knowing beforehand or identifying the material phases, Rietveld refinement can be performed. Sets of peaks are generated based on the selected phases. Then, the positions, intensity, and shape of the peaks (width, asymmetry etc.) are calculated based on the unit cell parameter, instrumental and material condition broadening to fit the experimental curve. Unit cell parameter values are taken once a satisfactory goodness of fit value, measuring the conformity of the calculated pattern to the measured experimental pattern, is reached.
2) **Profile fitting.** The existence of peaks is determined based on intensities detected in the experimental diffraction pattern. Phase(s) present in the sample is determined based on the detected peak positions and intensities. The peak positions, intensities, and peak shapes are individually calculated to fit the experimental data instead of as a whole in Rietveld refinement.

Several factors influence our selection of the preferred method to obtain the unit cell parameters. Firstly, peak broadening and noise-to-signal ratio in the CR state were significantly higher outside of the boxed area in Fig. 4.1b due to the cold work process. The diminished number of peaks and the induced preferred orientation led to difficulty in obtaining favourable Rietveld refinement results. Secondly, multiple contributions of peak signals in a small range due to overlapping leads to doubtful results, as different combinations of peak intensities and widths could lead to the same final fitted result. The consequence is multiple solutions to what is ultimately a mathematical problem to obtain a value fitting the experimental data.

Attempts to obtain lattice parameters using Rietveld refinement were done but the fitting result was unsatisfactory despite many attempts and thus not presented here. Hence, in the case of the textured CR and aged samples, profile fitting was chosen in an area that was least affected by peak broadening and has a high signal-to-noise ratio. Fig. 4.2a presents the full range profile fit and the refined lattice parameters with uncertainty in parentheses. It can be seen that even with a good visual fit, the refined

lattice parameters have high uncertainty. The difference between the observed and refined lattice parameters are shown in Fig. 4.2b. Only the peaks below 45° present as good fits, while the heavy influence of peak broadening and overlapping can be seen at higher angles. Diminished peaks and limited number of high confidence peaks does not allow for accurate calculation of all lattice parameters of a phase.

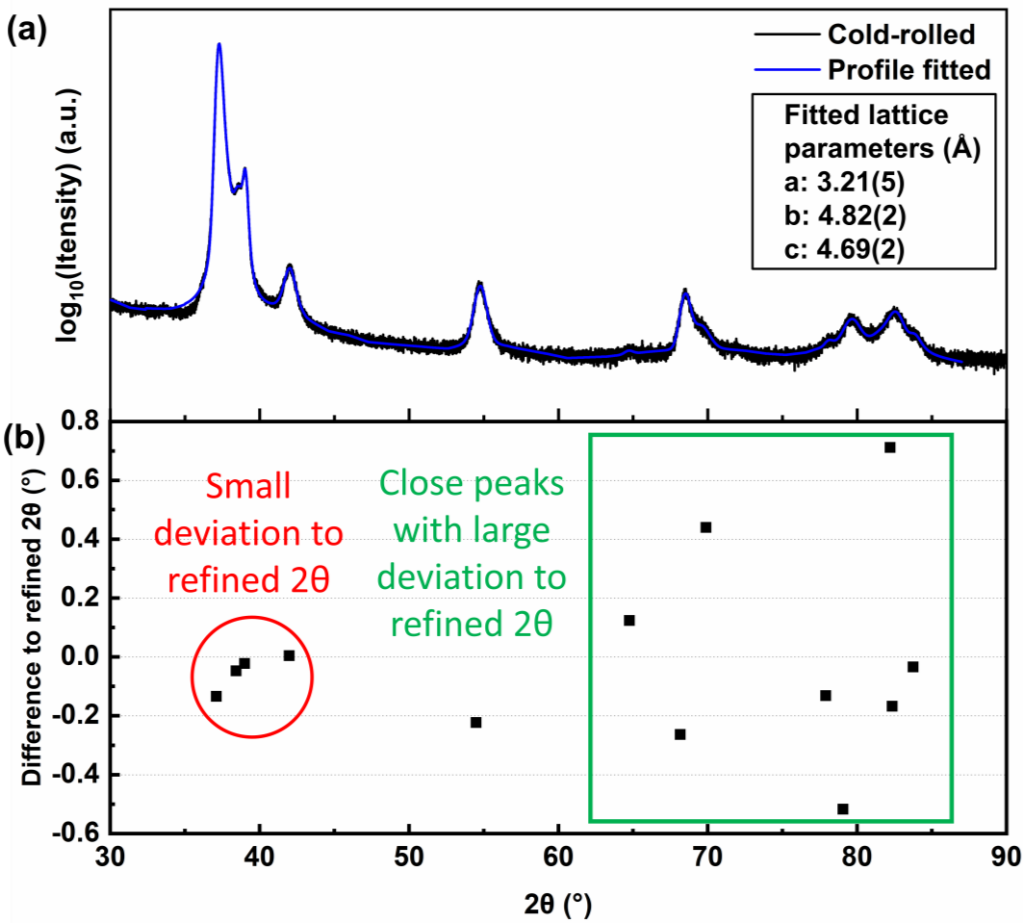

Fig. 4.2. (a) Profile fitted full range XRD pattern of CR Ti-22Nb. The inset shows the refined lattice parameters using the available peaks with uncertainty in parentheses. (b) The difference between the position of profile fitted peaks against the position of peaks calculated by refined lattice parameters.

4.2.3. In-situ XRD

The heating rate used in the collection of all in-situ XRD patterns in this study was fixed at 3 °C/min, while the temperature interval between the start of every in-situ XRD pattern of the CR sample collected was 10 °C. In these patterns, two regions of interest, 37.3° and 38.5°, were selected from the in-situ heating XRD scans of the CR specimen (Fig. 4.1c). These regions correspond to the $(020)_{\alpha''}$ peak and the collective peaks $(002)_{\alpha''}$, $(011)_{\beta}$ and $(111)_{\alpha''}$, in order of 2θ. The $(020)_{\alpha''}$ peak has

been reported by multiple studies [1-3, 5, 94, 123] to exhibit NTE and thus focus was placed on characterizing the lattice strain of this plane. Within these regions, the $(020)_{\alpha''}$ peak was least affected by overlapping from peak broadening and thus the reliability of the calculated peak position was high, allowing for high confidence in the calculated thermal lattice strain in the direction of interest, $[020]_{\alpha''}$. Under in-situ heating, the position of the $(020)_{\alpha''}$ peak visibly shifts to the right with increasing temperature. This, according to Bragg's law, $n\lambda = 2dsin\theta$, indicates a shrinking of the corresponding lattice spacing, d, with increasing temperature. The peak position of the $(020)_{\alpha''}$ peak was obtained through profile fitting for every in-situ scan. From the peak position, the lattice spacing of the $(020)_{\alpha''}$ peak can be calculated and thermal strain of $b_{\alpha''}$ was calculated for every 10 °C temperature interval starting from 0 °C. A low number of accurately indexed peaks greatly affects the accuracy and is insufficient to accurately refine all three lattice parameters $a_{\alpha''}$, $b_{\alpha''}$ and $c_{\alpha''}$. As a result, only the thermal strain of the well isolated $(020)_{\alpha''}$ peak is presented with high confidence. The average CTE presented in this entire thesis is defined from 0-100 °C to maintain consistency and comparability. The average lattice CTE of $(020)_{\alpha''}$ from 0-100 °C for the CR sample was calculated to be -41.5 ppm/°C using Equation (4.1, where α_{TE} is the average CTE, ε and T are lattice strain and temperature at 100 °C, and the subscripts represent initial values (0 °C in this study).

$$\alpha_{TE} = \frac{\varepsilon_0 - \varepsilon}{T_0 - T} \tag{4.1}$$

In both these scans, no observable peaks could be identified as ω phase. Weak or even complete absence of ω peaks is common in quenched Ti alloys, where the alloy does not dwell at temperatures favourable for growth of ω for any significant amount of time. The resulting athermal ω (ω_{ath}) are usually nanoscale in size and lack long-range order but observable under TEM.

4.2.4. Macroscale thermal expansion

In selecting the cold-roll reduction of our CR sample, a reduction amount that would provide the highest NTE response while still being able to provide clear microstructural characterization was desired. Excessive CR reduction while providing little to no improvement in NTE would only serve to further fracture grains in the sample, making it difficult for microstructural characterizations. The

NTE response along RD of three WQ samples that had undergone 30%, 50% and 70% reduction in plate thickness was measured and presented in Fig. 4.3. Among these, the 30% reduction exhibited the least NTE, while 50% and 70% reduction essentially exhibited the same NTE response. In a study by Monroe on a Ti-Nb alloy of identical composition, a cold work thickness reduction from 50% to 80% provided a minor NTE increase [1], but since further reduction from 50% did not contribute to any increase in NTE in our experiment, a 50% cold-roll reduction was selected to be the reference material exhibiting NTE in all our subsequent experiments.

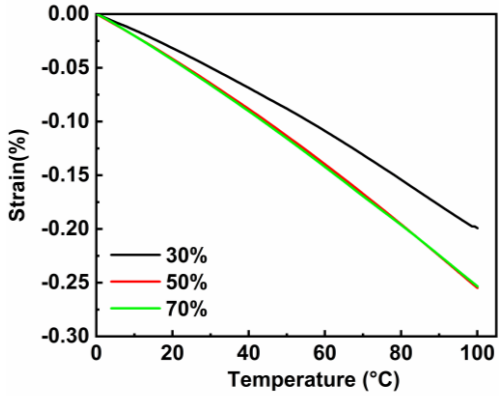

Fig. 4.3. Macroscale NTE response along RD of Ti-22Nb alloys of three cold-roll thickness reductions (30%, 50%, 70%).

Reference macroscale thermal expansion behaviours of Ti-22Nb samples were established with the martensitic water quenched (WQ) and cold-rolled (CR) states using TMA. The two sample states were heated from 0 °C with a rate of temperature change of 3 °C/min. Samples in these states were not heated past 100 °C to avoid exceeding the A_s temperature of ~100°C [31]. A dynamic change in phase composition would occur when heated past the As temperature, thus leading to inconsistency in the obtained thermal strain response. The average CTE of the sample was calculated using Equation (4.1, where macro thermal strain was used instead of lattice strain.

In Fig. 4.4a, the measured TE responses of WQ along two directions were identical, indicating that the WQ sample is isotropic in texture thus measurement along the third direction was assumed to be identical at 8.56 ppm/°C. For the CR specimen, strain measurements were taken along all three directions: RD, ND, and TD for a complete understanding of the sample's thermal expansion in all

directions. Although the negatively thermal expanding direction of interest has been reported to be along RD parallel to the $\langle 010 \rangle_{\alpha''}$ direction, an intriguing colossal positive thermal expansion of up to 100 ppm/°C was also reported [2] along the $\langle 100 \rangle_{\alpha''}$direction. Among the three directions along the CR sample, NTE was exhibited along RD as expected from literature and corresponds to a crystallographic texture of $\langle 020 \rangle_{\alpha''}$. The average CTE for CR sample was measured to be -25.3 ppm/°C and was in line with CTE reported by Monroe et al. [1] for a sample of exact composition and cold-roll reduction. Between the two remaining directions, ND showed a positive average CTE of 32.3 ppm/°C which is largest in magnitude of all three directions. From literature, this large PTE indicates that ND has a preferred orientation parallel to $\langle 100 \rangle_{\alpha''}$ [2] and consequently TD is parallel to $\langle 001 \rangle_{\alpha''}$.

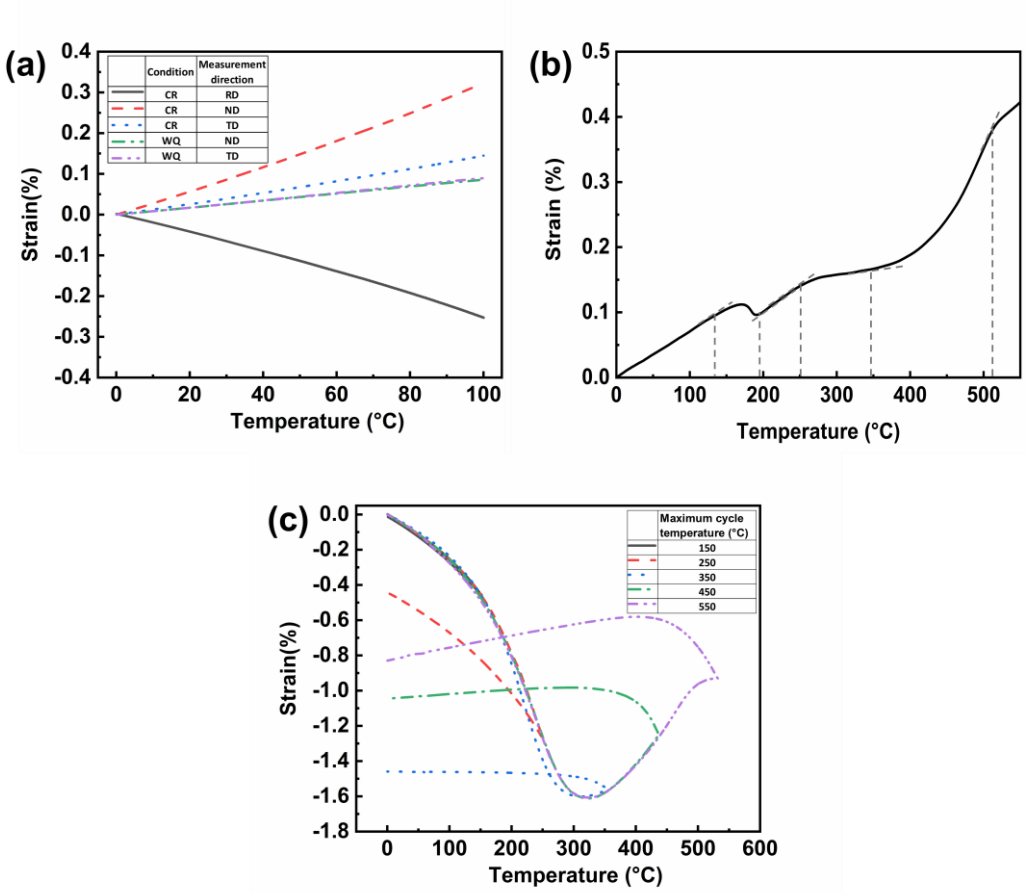

Fig. 4.4. (a) The macroscale thermal expansion response of WQ and CR samples along all directions from 0-100 °C. (b) Macroscale thermal expansion of WQ from 0-550 °C with points deviating from the gradient marked. (c) The NTE response of the CR sample over a wide temperature range from 0-(100n + 50) °C for n = 1-5.

Subsequently, the wide temperature range thermal strain response of WQ was measured from 0℃ to 550 ℃ in Fig. 4.4b. Points where change of gradient occur were measured visually by drawing a vertical drop line where the tangent deviates from the prior sections of constant gradient. Heating and cooling dilatometry of solution treated WQ Ti-Nb alloys have been previously reported by Bönisch [31] and dilatometric results here are in agreeance. In our study, this dilatometric result for WQ serves as an unaltered thermal expansion behaviour, while also acting as a reference for occurrence of phase transformations.

In Fig. 4.4c, the NTE behaviour of the CR sample was measured in a series of thermal cycles of increasing maximum temperature. All thermal cycles start at 0 ℃ and the lowest maximum temperature chosen was 150 ℃, this increment of 50 ℃ from 100 ℃ was chosen to elucidate the effects on the negative thermal expansion along RD when heated past the A_s temperature. Upon reaching maximum cycle temperature, the sample was cooled and the direction of the strain response reversed. In this experiment, the thermal strain response, average CTE retained upon cooling and the permanent negative strain incurred were of interest. An increasingly negative thermal strain gradient is seen in the first 300 ℃ during heating and a maximum negative strain of -1.47% was achieved around 320 ℃ before the gradient positively increases and strain rebounds with increasing temperature. At around 500 ℃, a dip in the positive gradient of the strain was observed before quickly reaching the maximum temperature of 550 ℃ and cooled. After every thermal cycle, the permanent strain retained by the sample and the resulting average CTE during cooling was recorded in Table 4.1. NTE magnitude was largely unchanged after a maximum cycle temperature of 150 ℃, and significant NTE was retained after heating to 250 ℃ relative to the CR state. After a maximum cycle temperature of 350 ℃, NTE was largely diminished and an astonishingly low average CTE of -0.22 ppm/℃ was obtained. After heating a maximum cycle temperature of 450 ℃, the sample exhibited a low linear PTE of 2.58 ppm/℃ across a wide temperature range during cooling. Lastly, a conventional PTE behaviour of 6.81 ppm/℃ was exhibited by the sample upon cooling from maximum cycle temperature of 550 ℃. This PTE magnitude is similar to Ti rich Ti-Mo and Ti-Zr alloys [124], thus it is assumed that no further change would be obtained upon heating to a higher temperature. The

permanent strain retained in the samples show a non-unidirectional trend, as increasingly negative strain was retained upon cooling to room temperature for the first three heat cycles up to a minimum at maximum cycle temperature of 350 ℃. The retained strain then showed positive increments at maximum cycle temperature of 450 ℃ and 550 ℃.

Based on the retained thermal expansion behaviour after the respective heating cycles, three temperature regions of interest were determined. The first temperature region of interest is where significant NTE is retained after the heat cycle to 150, 250 ℃. The study of the ability of the alloy to retain NTE at these elevated temperatures for a long duration was dedicated to Chapter 5. In this chapter, the thermal stability, i.e. the change in thermal expansion behaviour at elevated temperatures, was studied through aging at their relative maximum cycle temperatures for 10^n hours (n=1, 2, 3). In Chapter 6, the deterioration of NTE of the CR alloy to achieve ZTE at 350 ℃, low PTE at 450 ℃, and PTE at 550℃ were studied in terms of the sequence of phase transformations and the effects on its thermal expansion behaviour. In both these two chapters, the exhibition of thermal expansion behaviours will be studied from the perspective of macro and lattice scale thermal expansion, changes in phase composition, microstructure, and mechanical properties.

Table 4.1 Measured values of CR samples after undergoing single cycle heating and cooling to various temperatures.

Maximum temperature (℃)	Permanent strain after heating (%)	Average CTE between 0-100 ℃ after thermal cycle (ppm/℃)
150	-0.013	-25.07
250	-0.045	-22.81
350	-1.473	-0.22
450	-1.045	2.58
550	-0.829	6.81

4.2.1. Microstructural characterization

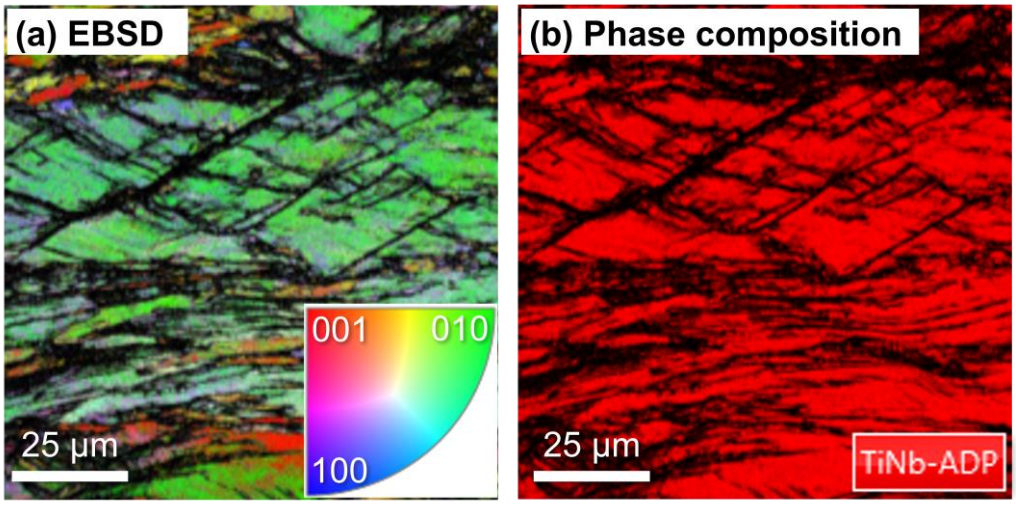

Fig. 4.5. (a) EBSD and (b) EDS images of the CR sample showing uniform $\langle 010 \rangle_{\alpha''}$ and fully martensitic composition.

Fig. 4.5a shows the EBSD image captured for the CR sample. The direction shown is parallel to the RD face and shows that a majority of grains are oriented perpendicular to the $\langle 010 \rangle_{\alpha''}$ direction as expected from literature. The grains appear as deformed and elongated grains with many zero-solution around the boundaries due to high angular difference. Fig. 4.5b shows the phase identification of the same area and was identified as pure α" phase. The legend ADP stands for alpha double prime (α").

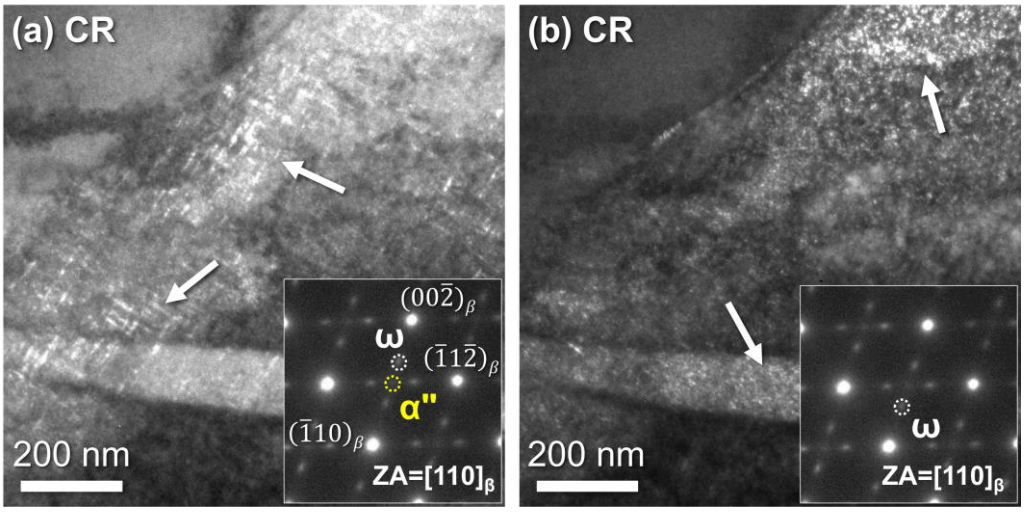

Fig. 4.6. DF TEM image of an area captured using two separate ω diffraction spots obtaining different ω morphologies in the CR sample. (a) Acicular and (b) globular ω precipitates are seen.

The strength of Ti alloys is closely related to the ω phase within the sample as ω induces strength but also brittleness within the material, hence TEM here will be focused on the change in morphology of the ω phase with aging to explain the resulting mechanical behaviours. Fig. 4.6 shows DF TEM images of the CR sample captured along the zone axis $[110]_\beta$ using the circled ω reflections at 1/3 and 2/3$\{112\}_\beta$ within the SAED inset to visualize the morphology of the initial ω phase in the CR sample. Two distinct morphologies were captured using different ω diffraction spots. Acicular basket-weave structures and globular ω phase were observed to be dispersed in the lathe and surrounding matrix in Fig. 4.6a and b respectively, indicated by white arrows in the figure. The globular ω phase is the commonly observed morphology in quenched Ti alloys where the high cooling rate is classified as an athermal process [70, 125, 126]. The acicular morphology fits descriptions of stress induced ω phase in cold-rolled Ti alloys and was only able to be imaged using one of the four ω reflections. Indeed, stress induced ω have been reported to form a preferred variant that can be detected in their SAED pattern [127, 128]. Distinction between the two morphologies is not required in the upcoming discussion and thus are hereby collectively referred to as ω_{ath} by their athermal formation conditions (quenched and stress induced).

4.3. Summary

In this chapter, macroscale thermal expansion of a CR Ti-22Nb alloy was characterized over a large temperature range from 0-550 °C. The subsequent chapters were based off of the thermal expansion behaviour exhibited by the alloy at specific maximum cycle temperatures. The lattice thermal expansion, microstructure and mechanical behaviour of the CR reference sample were established in this chapter and to be used for comparison of the effects of heating past A_s in the subsequent chapters.

5. NTE thermal stability and mechanical behaviour of cold-rolled Ti-22Nb under long-term aging

5.1. Introduction

The established NTE behaviour above A_s in Chapter 4 revealed that NTE is retained in the CR Ti-22Nb alloy after thermal cycling to 150 °C and 250 °C. Deterioration of NTE in Ti-Nb alloys operating above its A_s temperature is a property that requires careful consideration for possible future utilization of this alloy, as NTE is tightly connected to the stability of the metastable martensitic phase. Up until now, the effects of long-term exposure at high temperatures on the NTE ability and mechanical properties of cold-rolled martensitic Ti-Nb have not been explored. The goal of this chapter is to elucidate the thermal stability of NTE and resulting mechanical properties in CR Ti-22Nb isothermally aged at 150 °C and 250 °C for 10^n hours (n = 1, 2, 3). The NTE stability of the alloy will be evaluated through the phase composition and lattice thermal expansion of α" obtained through in-situ XRD and macroscale thermal expansion through dilatometry. Explanation of the origin of these changes will be supplemented by TEM microstructural observations and characterization of mechanical properties such as tensile tests, Young's modulus and Vickers hardness tests.

5.2. Results

The results of this chapter are organized to present the all the results for the 150 °C aged specimens first in Section 5.2.1, then results for the 250 °C aged specimens in Section 5.2.2. Discussion of the results will include both aging temperatures and will be presented collectively in Section 5.3.

5.2.1. Aging at 150°C

5.2.1.1. Macroscale thermal expansion

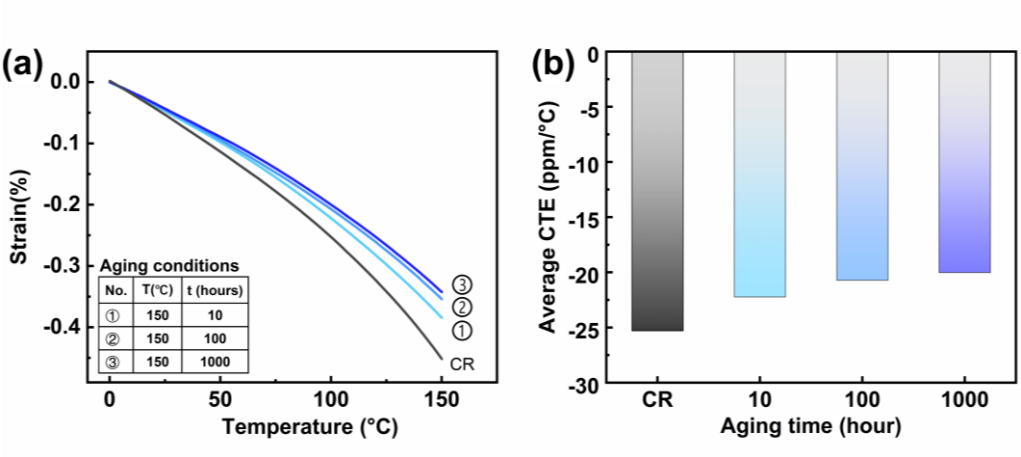

Fig. 5.1: (a) TMA measurements along RD for 150 °C aged samples and CR. (b) The calculated average CTE along RD between 0-100 °C of each sample.

The macroscale NTE response along RD between 0-150 °C for the CR and 150°C aged conditions are illustrated in Fig. 5.1. Increasing deterioration of NTE along RD was observed in the 150°C aged samples with increasing aging duration compared to the initial CR state. The largest loss in average CTE occurred within the first 10 hours of aging at 150 °C, going from -25.3 ppm/°C to -22.2 ppm/°C while subsequent tenfold increase in aging time indicated progressively less loss of NTE (-20.7 ppm/°C and -20.0 ppm/°C for samples aged at 100 and 1000 hours respectively). The trend of CTE with increasing aging times shows signs of plateauing over a long period of time, suggesting that a metastable equilibrium is being approached within the sample with longer aging time.

5.2.1.2. X-ray diffraction

The phase constitutions of the 150 °C aged samples were first studied by ex-situ XRD scans at room temperature and presented in Fig. 5.2a-c. In these three figures, no significant changes were observed when comparing between aging durations. This is also true when comparing with the wide-angle CR scan in Fig. 4.1a. The $(020)_{\alpha''}$ lattice thermal strain was calculated by in-situ XRD using the same region of interest as Fig. 4.1c using profile fitting. This was done for every in-situ scan at 25 °C intervals from 0-150 °C at a rate of temperature change of 3 °C/min. The lattice thermal strain for every aging duration was calculated from the results of profile fitting and are depicted in Fig. 5.2g, h.

The average lattice CTE between 0-100 °C was highest in the least aged 10h sample at -43.4 ppm/°C, followed by reduced NTE in subsequent longer aged samples at -41.4 ppm/°C and -34.9 ppm/°C for 100h and 1000h aging duration respectively. In Fig. 5.2g-h, one can notice that the CR specimen exhibited weaker lattice NTE, at -41.5 ppm/°C, than the 10h aged sample but stronger NTE than the 100h aged sample. Further scrutinizing the room temperature ex-situ scans of the $(020)_{\alpha''}$ peak in Fig. 5.2i revealed a leftward peak shift with increasing aging duration (indicated by a leftward arrow). The $(020)_{\alpha''}$ for the 10h aged sample is situated at the rightmost, corresponding to the smallest lattice spacing of the four conditions according to Bragg's law, and the CR at the leftmost indicating the largest lattice spacing. Similarly, looking at the peaks $(002)_{\alpha''}$ and $(111)_{\alpha''}$, indicated by vertical lines in Fig. 5.2j, we can see an opposing trend to its neighbouring peak. First of all, an obvious rightward shift, corresponding to shrinking lattice spacing, was observed between subsequent aging durations, followed by an increase in intensity in between the two peaks.

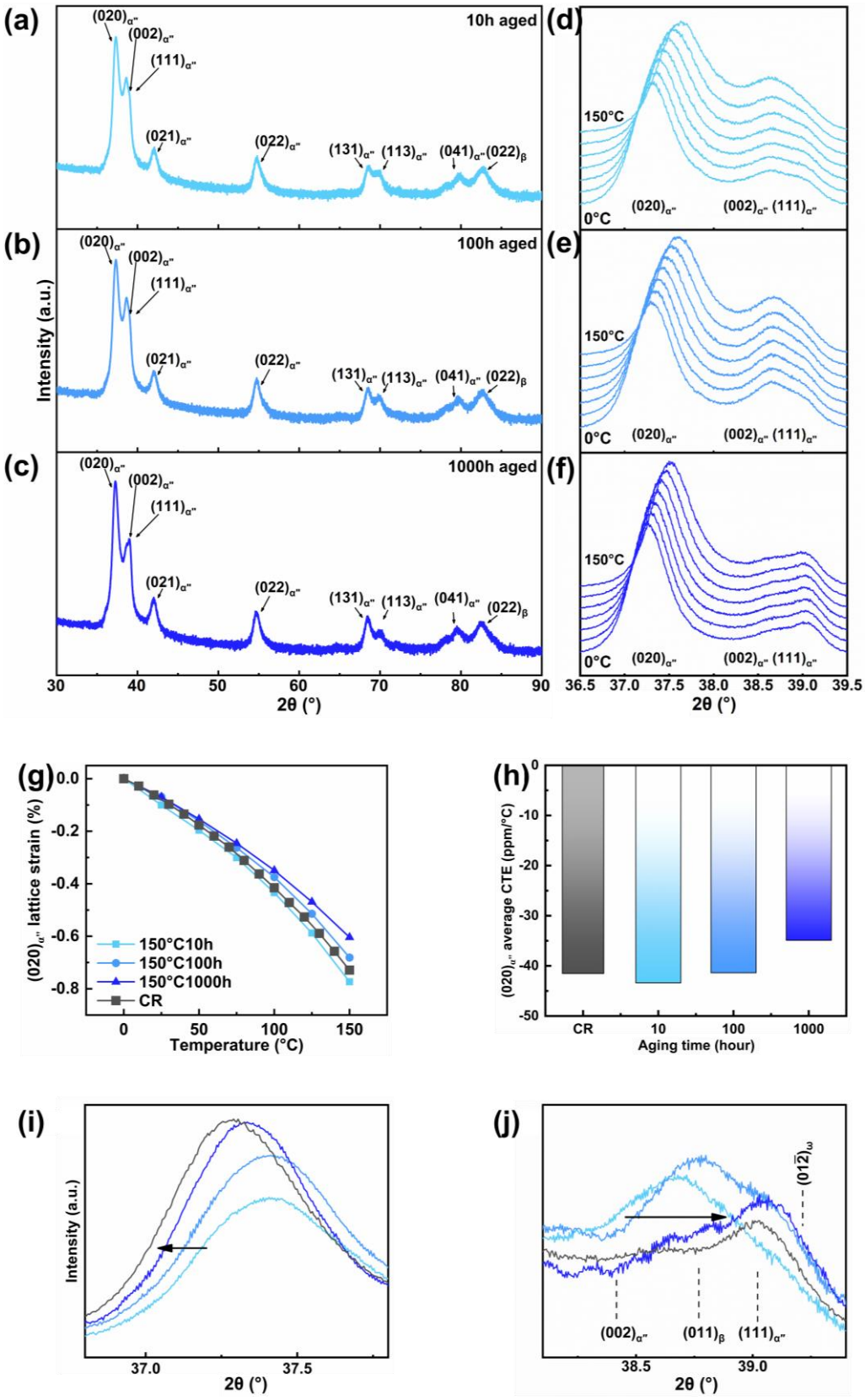

Fig. 5.2. (a-c) Wide range XRD scans of 150 °C aged samples at room temperature. (d-f) Enlarged area showing in-situ diffraction of peaks $(020)_{\alpha"}$, $(002)_{\alpha"}$ and $(111)_{\alpha"}$ from 0 °C to 150 °C. (g) Lattice NTE

response of $(020)_{\alpha''}$ of all three aging conditions and CR, then visualized in (h). Stacked room temperature ex-situ XRD of (i) $(020)_{\alpha''}$, (j) $(002)_{\alpha''}$ and $(111)_{\alpha''}$ peaks together with CR.

5.2.1.3. Microstructural characterization

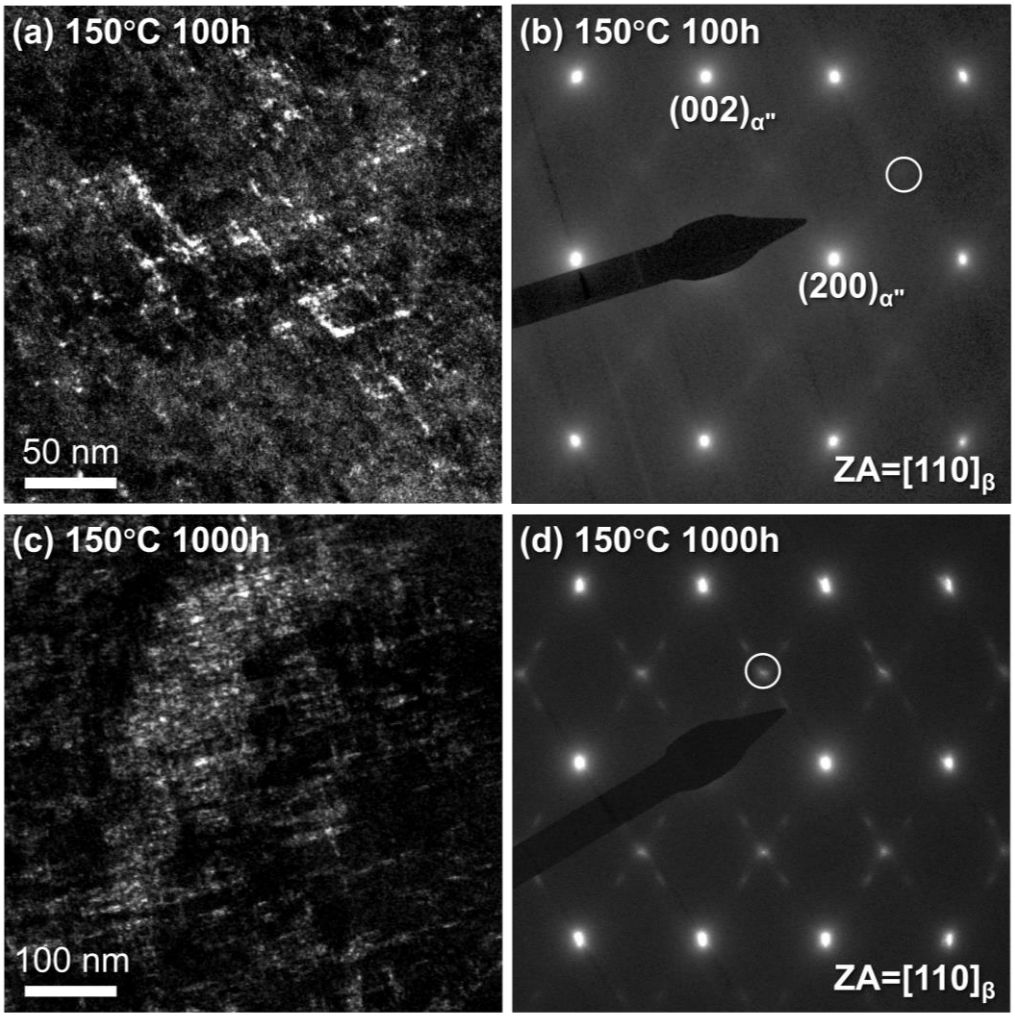

Fig. 5.3. DF TEM of α" after aging for (a) 100h and (b) 1000h captured using the circled $1/2\{112\}_{\beta}$ spot, with their respective SAED patterns (c, d)

In Fig. 5.3, the morphology of α" for the samples aged at 150 °C for 100h and 1000h were captured with DF TEM using the $1/2\{112\}_{\beta}$ SAED spot circled in Fig. 5.3b and d. The comparatively short duration of aging in the 10h aged sample did not result in a change in morphology that was noticeable using the aforementioned SAED spot. In Fig. 5.3a and Fig. 5.3c, an acicular basket-weave morphology was observed for samples aged for 100h and 1000h using the $(200)_{\alpha''}$ spot circled in Fig. 5.3b and d respectively. In the 100h aged state, the observed acicular structures were sparse and discontinuous. Aging for 1000h saw these sparse structures develop into larger contingent areas of the

same morphology. The larger and more distinct morphology was reflected in the increased intensity of the $1/2\{112\}_\beta$ SAED spot of the 1000h sample when comparing Fig. 5.3b and d.

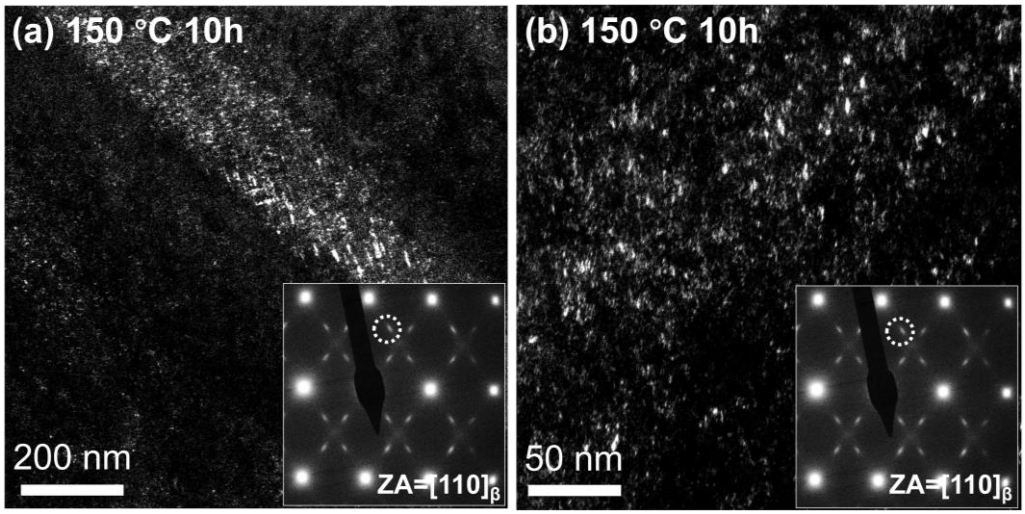

Fig. 5.4. DF TEM of ω captured using the circled SAED diffraction spot in the inset after aging for 10h at 150 °C. ω is seen (a) concentrated in a lath form similar to lath seen in Fig. 4.6 and (b) dispersed in the surrounding matrix.

The morphology of ω phase in the sample aged for 10h at 150 °C was captured using the $1/3\{112\}_\beta$ SAED diffraction spot shown in the inset of Fig. 5.4a. In these figures, ω particles were seen concentrated in a lathe form (Fig. 5.4a) and also dispersed in the surrounding matrix (Fig. 5.4b). The distribution of ω in lathes and the surrounding matrix is similar to the distribution in the reference CR sample (Fig. 4.6). The morphology was observed to be more ellipsoidal and appear denser and larger compared to the CR state. This signals that the ω observed here were the same as the ω_{ath} seen initially in the CR sample but grown under favourable thermal conditions. In the CR sample, globular ω_{ath} particles were measured to be ~1 to 3 nm in radius. While in Fig. 5.4, the grown ellipsoidal ω_{ath} were measured to be approximately 4 to 7.5 nm along the major axis and roughly 1 to 3 nm along the minor axis. Large particles of ω_{ath} in the 10h aged sample were measured to be around 10 nm along the major axis and 4 nm along the minor axis.

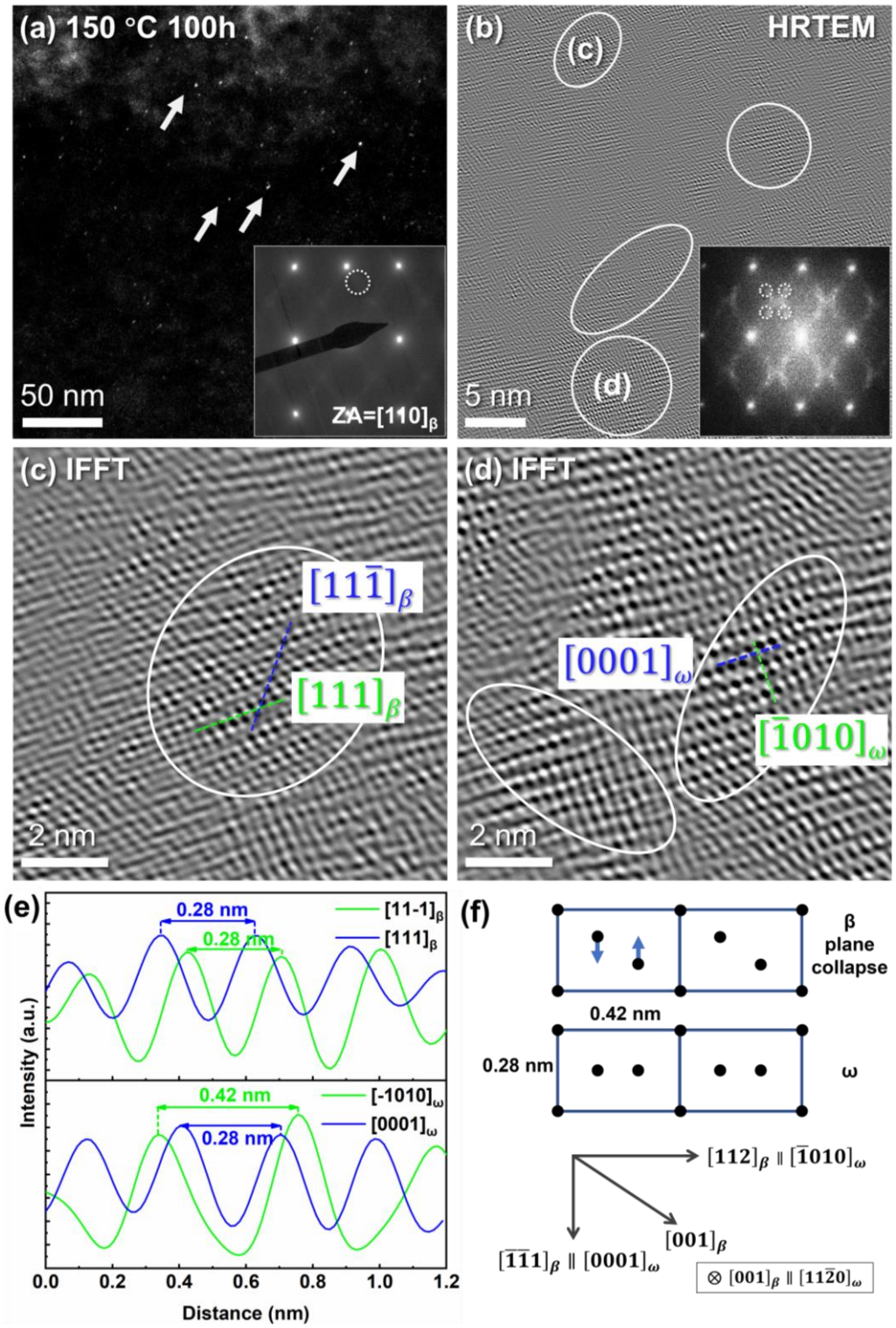

Fig. 5.5. (a) DF TEM of ω and the captured SAED pattern in the inset showing uniformly dispersed particles. (b) HRTEM of said area and the FFT inset that matches the SAED pattern captured. Several areas of clear lattice fringes are circled in white and two are selected to be enlarged in (c) and (d). Intensity profiles of the lattice fringes were measured along the dashed lines in (e) and their respective directions labelled with respect to the ω and β lattice shown in (f).

The morphology of ω in the sample aged at 150 °C for 100h is presented in Fig. 5.5a was captured using the identical 1/3$\{112\}_\beta$ SAED diffraction spot as before. The previously distinct ω precipitates in the 10h state were replaced by a distribution of extremely fine particles throughout the β matrix indicated by white arrows. Compared to the CR and 10h SAED patterns, the SAED inset in Fig. 5.5a appeared as a set of diffuse streaks instead of distinct ω diffraction spots at 1/3 and 2/3$\{112\}_\beta$ for commensurate ω precipitates. Diffuse streaking in SAED patterns is often observed when fine precipitates are detected [129]. The appearance of diffuse streaks such as these match the descriptions of streaks produced by cylindrical precipitates, specifically those in the shape of discs [129, 130]. Specifically in Ti alloys, diffuse streaking at the 1/3 and 2/3$\{112\}_\beta$ positions have been observed in Ti alloys that contain fine incommensurate ω embryos that are at the cusp of formation from isothermal processes [131-133]. In order to discern the size and morphology of these extremely fine particles, HRTEM was employed on the sample and presented in Fig. 5.5b. In the inset of Fig. 5.5b, the FFT of the captured area matched the SAED pattern of Fig. 5.5a, and an inverse FFT image was produced by masking the selected FFT streaks circled in white (Fig. 5.5b). Several areas of clear, but short ranged fringes were seen in the inverse FFT image. Two larger notable spots were highlighted with white circles and enlarged in Fig. 5.5c, d. The dimensions of these discontinuous areas were around 2-3 nm along the minor axis and 3-4 nm along the major axis. In the two selected areas (Fig. 5.5c, d), two different orientations of ω were observed, as characterized by the lattice spacings measured through the intensity profiles of the fringes. Shown in Fig. 5.5e, the lattice spacings of the observed fringes in Fig. 5.5c were measured to be 0.28 × 0.28 nm corresponding to $[111]_\beta$ and $[11\bar{1}]_\beta$ directions. In Fig. 5.5d, the lattice spacings were measured to be 0.42 × 0.28 nm. In this area, fringes of spacing 0.42 nm corresponded to the direction $[\bar{1}010]_\omega \parallel [112]_\beta$ and spacings of 0.28 nm corresponding to the direction $[0001]_\omega \parallel [\bar{1}\bar{1}1]_\beta$. The orientation relationship between the ω and β structure is shown in Fig. 5.5f. Both of these lattice spacings of the ω phase have also been observed by Liu et al. in a similar β Ti alloy [134]. The lattice spacings in Fig. 5.5c and d were respectively described to as non-ideal and ideal ω lattices of different variants originating from the well-studied lattice collapse mechanism of the β matrix. Evidently, these ω precipitates were different

morphologically to the observed commensurate ellipsoidal ω_{iso} particles in the 10h aged sample that had undergone isothermally promoted growth.

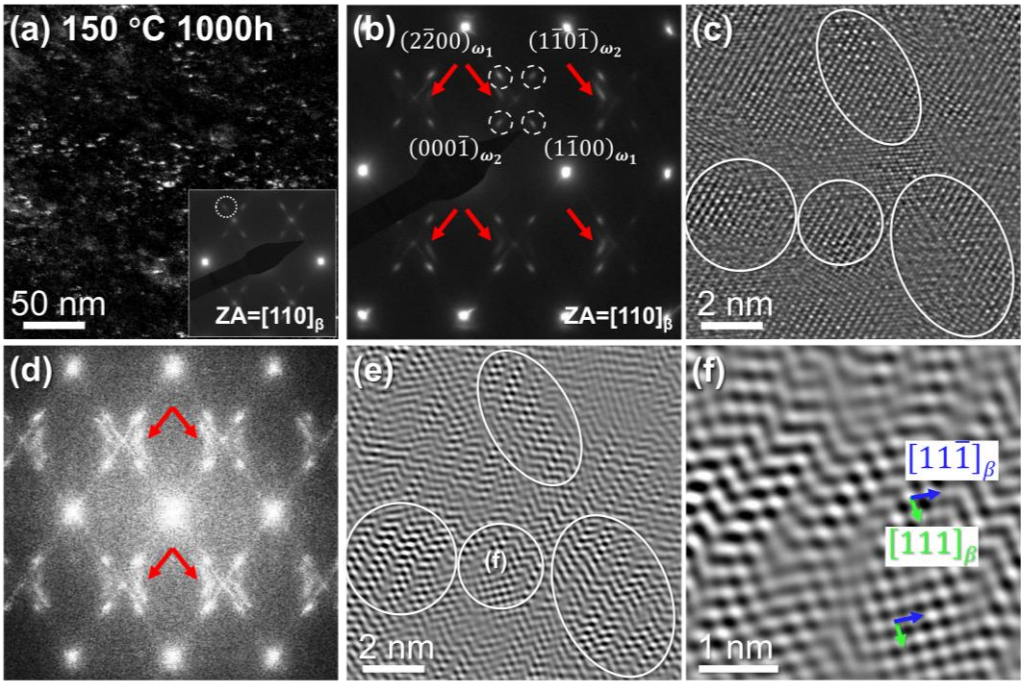

Fig. 5.6. (a) DF TEM image of ω imaged using the circled SAED diffraction spot in the inset. (b) A peculiar SAED pattern captured in only certain areas of the sample showing extra circular diffraction streaks marked with red arrows. The two ω variants are circled and labelled to for discussion. (c) HRTEM image of with circled areas of clear lattice fringes and the respective FFT shown in (d). Inverse FFT was performed using the extra circular diffraction streaks and shown in (e). A selected area is enlarged and presented in (f) to show the lattice spacings measured.

In the sample aged 1000h at 150 °C, the SAED pattern captured in the inset of Fig. 5.6a resembles the ones seen in the CR and 10h states with distinct commensurate ω diffraction spots. DF TEM (Fig. 5.6a) captured using the circled $1/3\{112\}_\beta$ ω spot showed large, well-defined ellipsoidal ω precipitates. These particles measure from 4-12 nm along the major axis and 3-6 nm along the minor axis. However, an unusual SAED spot was captured at certain areas within the sample as shown in Fig. 5.6b. In this pattern, an extra circular diffuse streak was detected and marked with red circles in Fig. 5.6b. This diffuse streak was not positioned at the ideal ω or α" spots but was seen between the two ω variant diffraction spots marked in dotted white circles in Fig. 5.6b and to the sides of the α" spot. HRTEM was employed in the area where the diffraction pattern was captured to discern the morphology of precipitates contributing to this extra diffuse streak and shown in Fig. 5.6c. The FFT

of this area was shown in Fig. 5.6d and matches the SAED pattern in Fig. 5.6b, with the extra diffuse streaks now clearly visible at the same locations marked with red arrows. To visualize the distribution and morphology contributing to these extra diffuse streaks, inverse FFT was performed by masking these extra diffuse streaks and presented in Fig. 5.6e. In this figure, numerous linear fringes were seen in multiple locations circled in white. An area is selected and magnified in Fig. 5.6f to measure the spacing and directions of these fringes. The 0.28 × 0.28 nm spacings and directions of these fringes were identical to the ones measured in Fig. 5.5e, evidencing that these circular diffuse streaks were also contributed by ω precipitates.

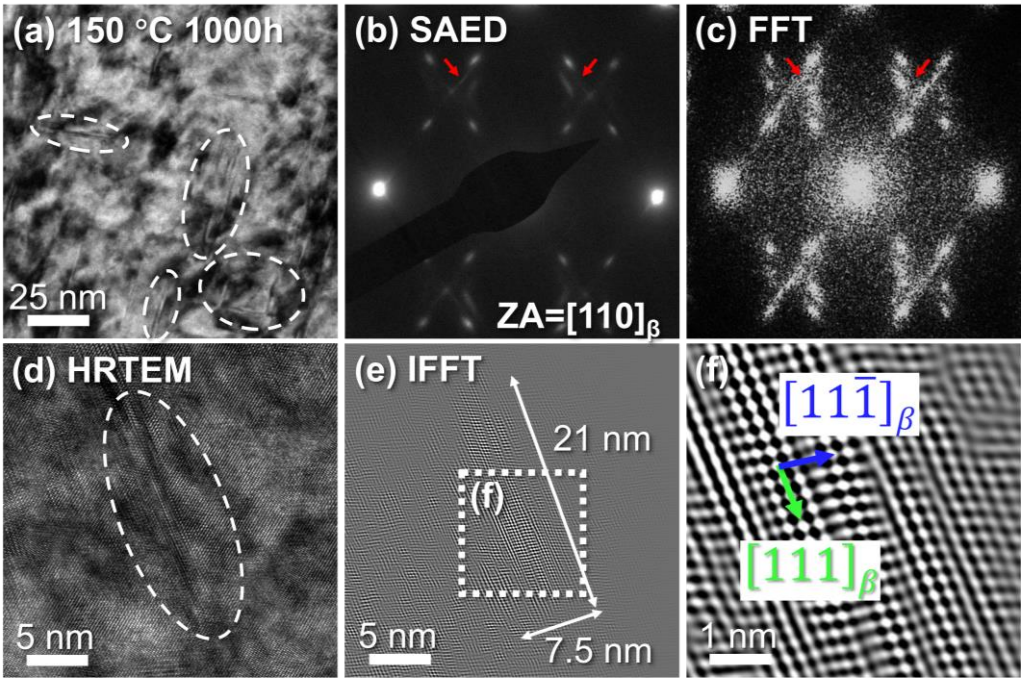

Fig. 5.7. (a) BF TEM image of an area in the 150 °C 1000h aged sample containing fine precipitates. Fig. 5.6b shows the SAED pattern of this area. These precipitates are related to the thin diffraction streak marked in red arrows in (b) between the ω and α" spots. (c-d) HRTEM was performed in the area and clear disc-like precipitates similar to the BF image were found. (e) Inverse FFT was performed by selecting the diffraction streaks marked in (c) and a disc-like shape similar in width and length was found. (f) Enlarged area of the disc-like precipitate to measure lattice spacings identical to those in Fig. 5.5c and Fig. 5.6f.

Additionally, within certain areas of the 1000h aged sample, numerous fine precipitates that measured lengthwise of 19-25 nm were found under bright field (BF) TEM mode (Fig. 5.7a). The description of fine precipitates of this morphology coupled with the fine streaks seen in the SAED pattern (marked with red arrows in Fig. 5.7c) matched descriptions of disc-like precipitates [129, 130, 135]. HRTEM

performed on this area showed regions that resembled the disc-like precipitates as seen in Fig. 5.7d. Inverse FFT (Fig. 5.7e-f) performed on this area by selecting the streaks marked in Fig. 5.7c reveals clear plate-like bands of length around 20 nm and thickness of around 6 nm, matching the dimensions of the precipitates measured under BF mode. These plate-like bands were measured with lattice spacings of 0.28 × 0.28 nm and exact intersecting angle as previously found in Fig. 5.5c and Fig. 5.6f. This confirmed that disc-shaped ω_{iso} precipitates were found in the 1000h aged sample.

5.2.1.4. Mechanical behaviour

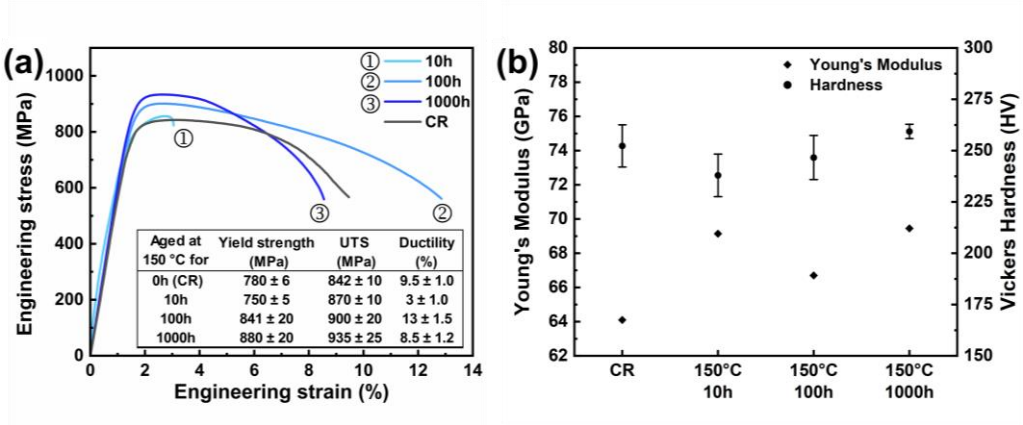

Fig. 5.8. (a) Tensile test and (b) Vicker's hardness and Young's modulus of the 150 °C aged and CR samples.

Fig. 5.8a shows the tensile test results for representative samples aged at 150 °C for each duration. The yield strength taken as 0.2% strain starts off at 780 MPa for the CR sample and showed an initial drop when aged to 10h to 750 MPa. Subsequent tenfold increase in aging duration saw constant increase in yield strength at 841 MPa and 880 MPa for 100h and 1000h respectively. The trend of ductility showed an abnormal behaviour where ductility from CR to 10h decreased initially but greatly increased at 100h and slightly decreases at 1000h. The UTS increased with aging time from 842, 870, 900, 935 MPa for CR, 10h, 100h, 1000h samples respectively. The Young's modulus increased significantly during the first 10 hours of aging from 64.1 to 69.1 GPa but experienced a slight dip at 100h to 66.7 GPa and increased to 69.5 GPa. The Vickers hardness decreased initially when aged from CR to 10h from 252.3 HV to 238.0 HV and subsequently increased with aging time to 246.6 HV and 259.3 HV for 100h and 1000h respectively.

5.2.2. Aging at 250°C

5.2.2.1. Macroscale thermal expansion

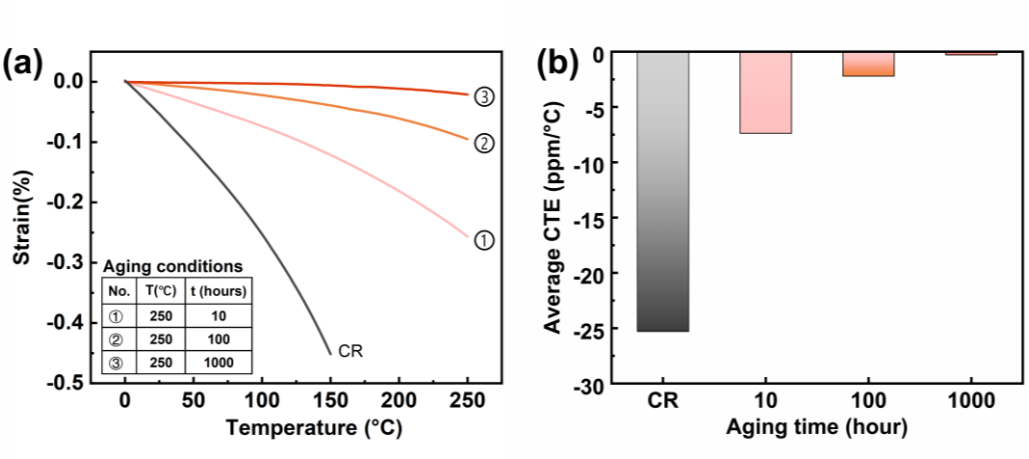

Fig. 5.9. (a) TMA measurements along RD for 250 °C aged samples and CR. (b) The calculated average CTE along RD between 0-100 °C of each sample.

In Fig. 5.9, macroscale thermal expansion along RD from 0-250 °C of 250 °C aged samples at 10, 100, 1000 hours was presented and a much more drastic change in thermal expansion was observed with increasing aging durations. The change in average CTE between 0-100 °C from the CR state to 250 °C 10h state is evidently the largest, from -25.3 ppm/°C to -7.37 ppm/°C. Aging for 100 and 1000 hours gave NTE of -2.21 ppm/°C and -0.29 ppm/°C respectively. Although the illustrated average CTE in Fig. 5.9b also indicated a plateauing effect, the values seemed to taper off more drastically compared to the mild slope of the 150 °C aged samples. This could indicate that the sample at each duration is further from metastable equilibrium compared to the samples aged at 150 °C for the same duration. Following this trend of CTE evolution, one can hypothesize that further evolution of CTE past 1000 hours could lead even closer towards ZTE or even PTE if given enough time.

5.2.2.2. X-ray diffraction

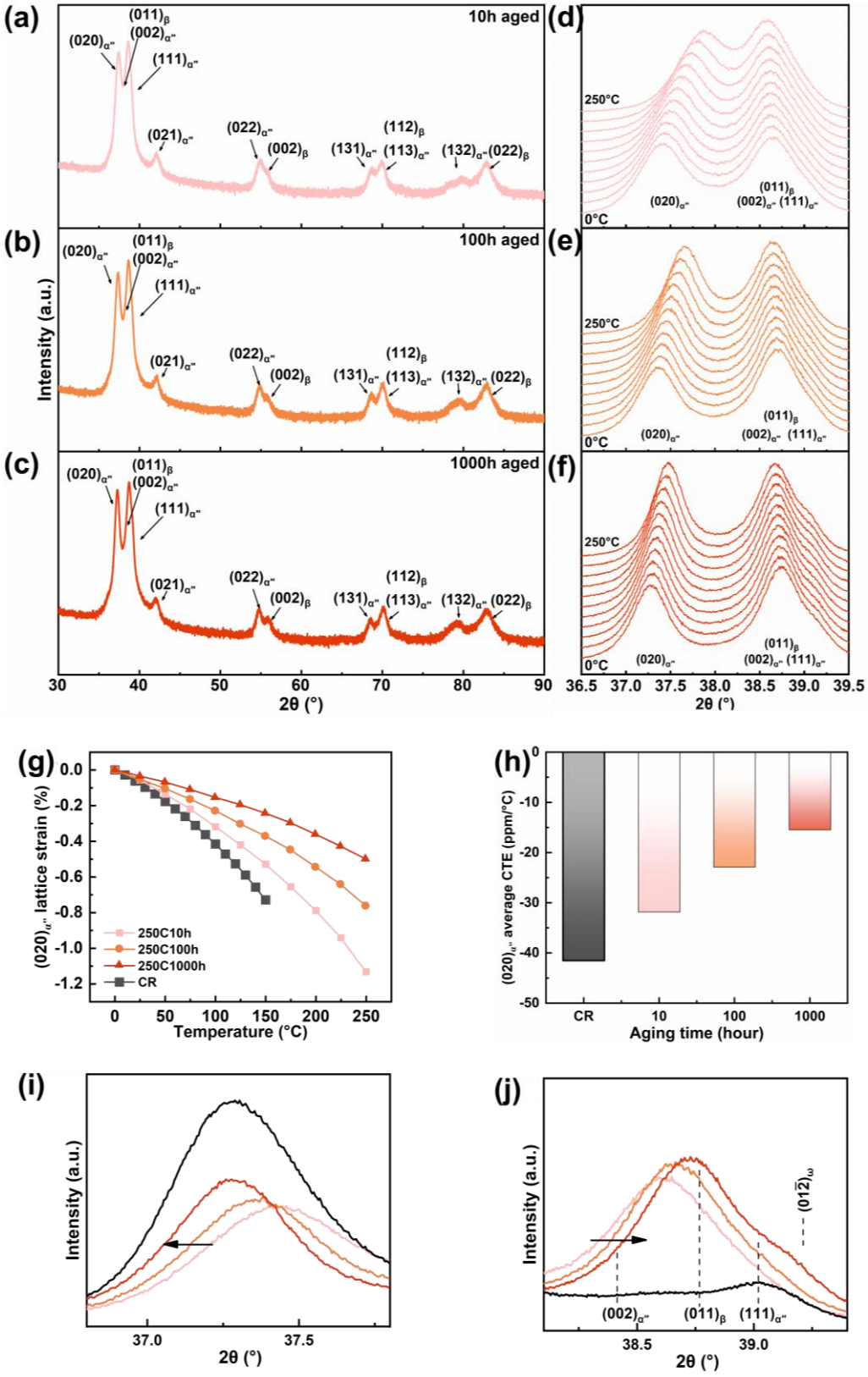

Fig. 5.10. Wide range XRD scans of 250 °C aged samples. (d-f) Enlarged area showing in-situ diffraction of peaks $(020)_{\alpha"}$, $(002)_{\alpha"}$ and $(111)_{\alpha"}$ from 0 °C to 250 °C. (g) Lattice NTE response of $(020)_{\alpha"}$ of all

three aging conditions and CR, then visualized in (h). Stacked room temperature ex-situ XRD of (i) $(020)_{\alpha''}$, (j) $(002)_{\alpha''}$ and $(111)_{\alpha''}$ peaks together with CR.

Fig. 5.10a-c shows the wide-range XRD scans of samples aged for 10, 100, and 1000 hours at 250 °C. Largely the same peaks observed in these samples were similar to the 150 °C aged samples in Fig. 5.2a-c. However, differences between the two sets of diffraction patterns were spotted at several positions of increased intensities corresponding to positions of β peaks in the 250 °C aged samples. Namely at 38.5° for $(011)_{\beta}$, 56° for $(002)_{\beta}$, 70° for $(112)_{\beta}$ and 83.3° for $(022)_{\beta}$. Lattice NTE was still exhibited by the $(020)_{\alpha''}$ peak in all three samples after aging, as shown by the in-situ peak shift from 0-250 °C in Fig. 5.10d-f. The average $\langle 010\rangle_{\alpha''}$ CTE of the 250 °C aged samples were measured to be -31.8, -22.9 and -15.5 ppm/°C for aging duration 10, 100 and 1000 hours respectively (Fig. 5.10g, h). Unlike the 150 °C aged series, the least aged sample did not exhibit higher lattice NTE than the CR sample. Looking at the stacked $(020)_{\alpha''}$ peaks in Fig. 5.10i of the aged and CR samples, we see a similar situation where the least to most aged is ordered from right to left, with the CR sample situated at the leftmost. In Fig. 5.10j, the first distinct change was seen in the evident increase of intensity of the $(011)_{\beta}$ peak mentioned before. A unanimous leftward shift was observed in this area in the aged samples arranging from least to most aged. Lastly, a shoulder peak corresponding to a possible $(01\bar{2})_{\omega}$ peak can be seen on the rightmost position around 39.4°.

5.2.2.3. Microstructural characterization

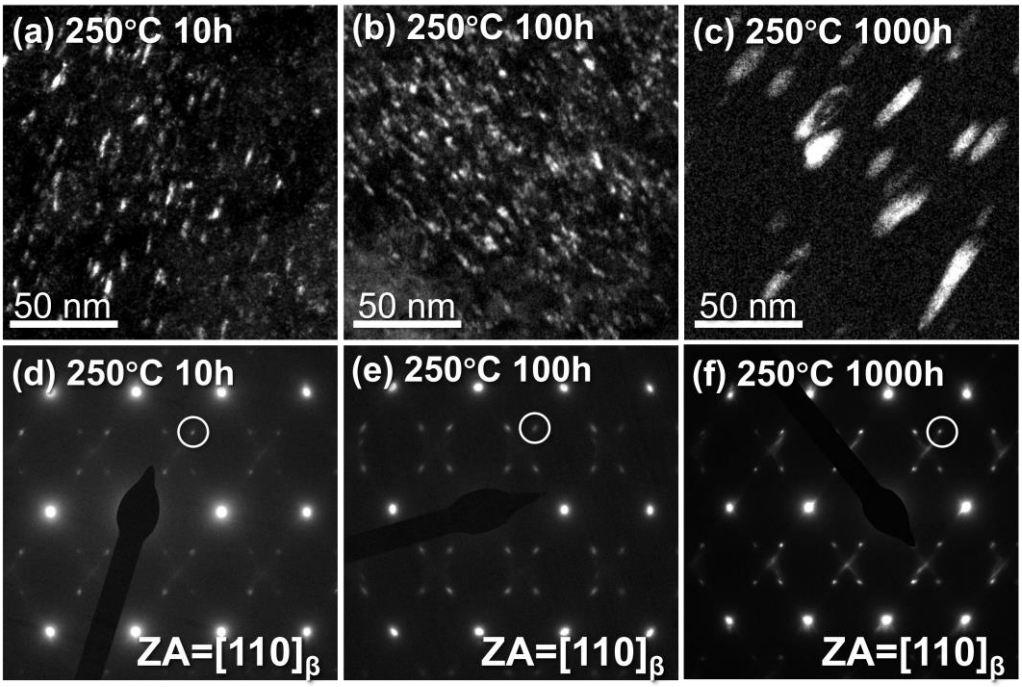

Fig. 5.11. DF TEM images of ω in samples aged at 250 °C for (a) 10h, (b) 100h, (c) 1000h and their respective SAED patterns (d-f).

Fig. 5.11a-c shows the morphology of ω imaged in the samples aged at 250 °C for 10h, 100h and 1000h respectively using the circled SAED spots in Fig. 5.11d-f respectively. In all the SAED patterns, clear ω spots at the commensurate 1/3 and 2/3$\{112\}_{\beta}$ spots were seen. In the DF images for the 10h and 100h aged states (Fig. 5.11a, b), distinct ellipsoidal ω were seen with dimensions of around 5-10 nm along the major axis and 2-4 nm along the minor axis. The density of ω, however, was much higher in the 100h state. The morphology of ω imaged in the 1000h aged sample (Fig. 5.11c) showed ellipsoidal particles that were much larger than all the previous aged states at 10-50 nm along the major axis and 3-12 nm along the minor axis.

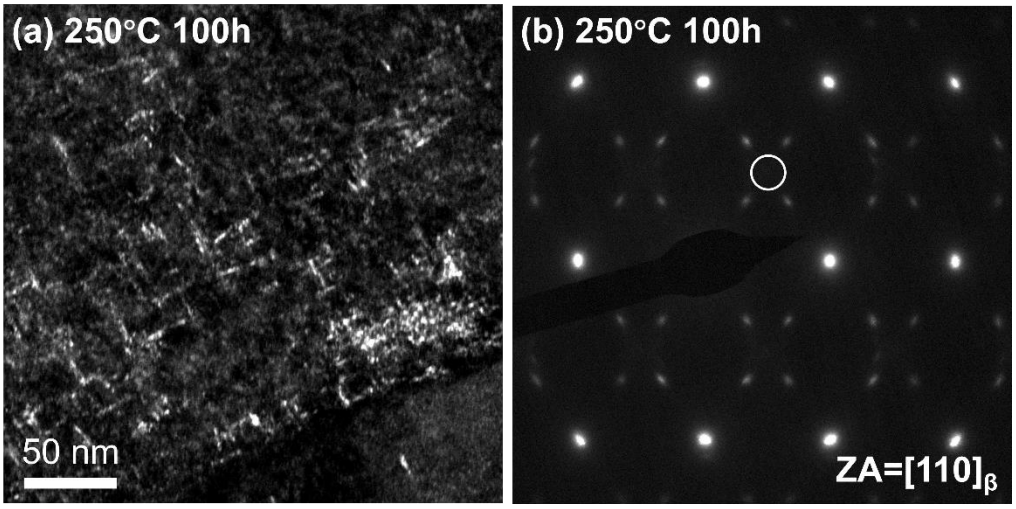

Fig. 5.12 (a) DF TEM of α" and the (b) captured SAED pattern in the sample aged at 250 °C for 100h. Short basket-weave acicular structures were seen.

The morphology of α" in the sample aged at 250 °C for 100h was captured under DF TEM (Fig. 5.12a) using the circled SAED diffraction spot in Fig. 5.12b. A sparsely distributed basket weave structure was observed, closely resembling the structure of α" in the sample aged at 150 °C for 100h (Fig. 5.3a). Similar to the 150 °C aged samples, this basket weave structure was not captured in the 10h aged samples possibly due to insufficient time for these structures to be visibly developed. The DF morphology of α" in the 1000h aged sample is showcased in Fig. 5.13a, captured using the same α" diffraction point shown in Fig. 5.13b. The α" diffraction spot in the 1000h aged sample was visibly brighter and DF imaging showed distinct intersecting acicular structures in a basket weave configuration. HAADF imaging of the 1000h aged sample is presented in Fig. 5.13c and presents a similar intersecting morphology, but much more well developed and in a larger area. EDS was performed in this region in Fig. 5.13d to show the distribution of Nb in this aging condition. The distribution of Nb revealed gaps corresponding regions of lean Nb to the positions of acicular structures. This evidenced that the acicular structures were lean in Nb. In both these aging states, we can determine that the intersecting basket weave structures had slowly developed with longer isothermal duration. Hence, these structures were identified as $\alpha"_{iso}$ formed through isothermal aging.

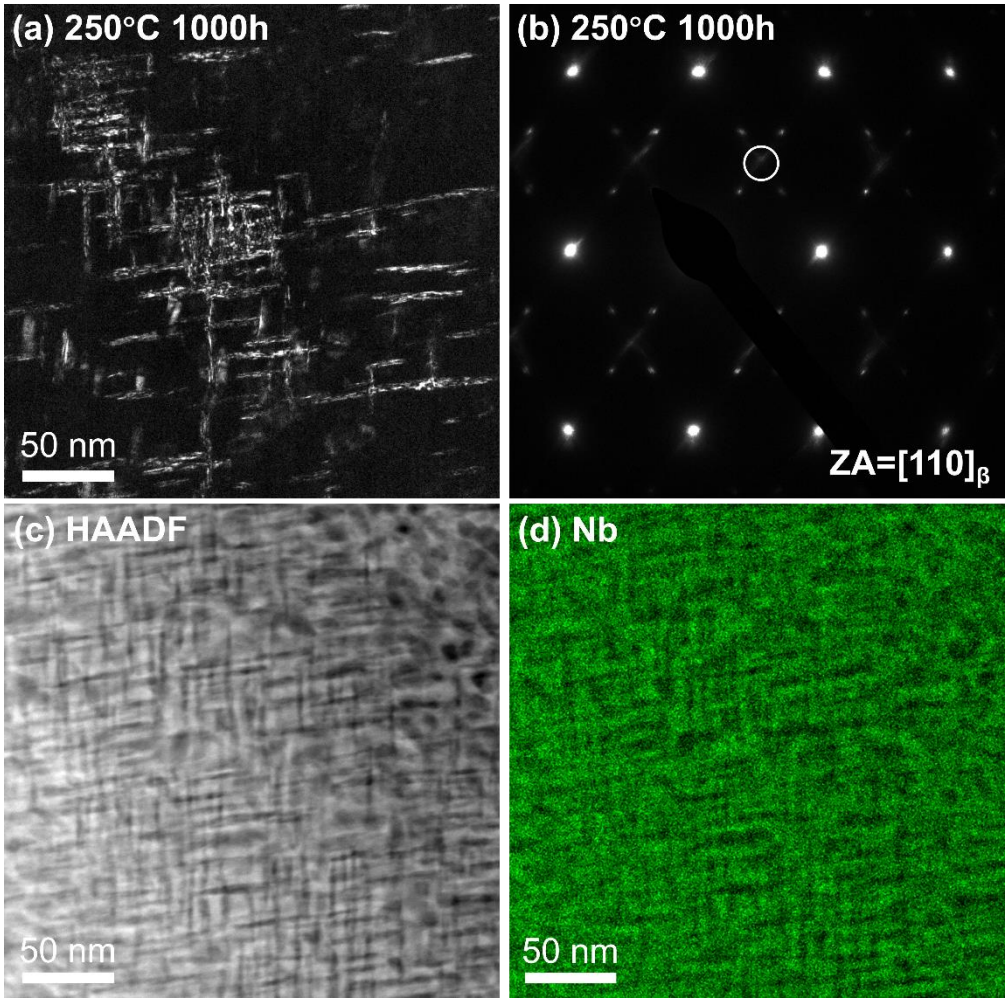

Fig. 5.13. (a) DF TEM of α" in the sample aged at 250 °C for 1000h and the captured (b) SAED pattern. (c) HAADF-STEM image of the sample showing a wide-range basket-weave acicular structure and (d) EDS mode under HAADF-STEM that shows zones of lean Nb correlating to the acicular structures.

5.2.2.4. Mechanical behaviour

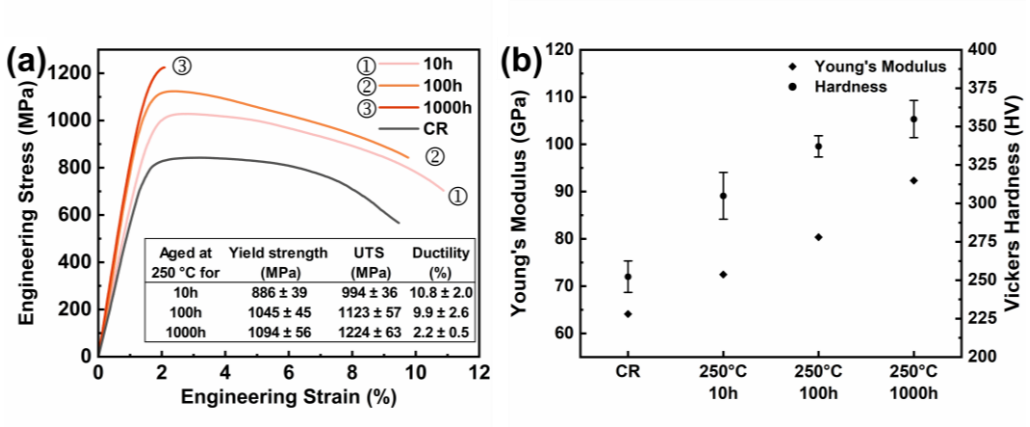

Fig. 5.14. (a) Tensile test response and (b) Vicker's hardness and Young's modulus of the 250 °C aged samples.

In Fig. 5.14, the change in mechanical behaviour of the samples aged at 250 °C showed a very gradual unidirectional change. The yield strength and ultimate tensile strength both saw significant increase from aging. The yield strength of the 10, 100, 1000h aged samples saw a steady increase of 886, 1045 and 1094 MPa respectively from the 780 MPa of the CR state. The ultimate tensile strength of the aged samples also saw a one-way increase from 842 MPa of the CR state to 994, 1123 and 1224 MPa at 10, 100 and 1000h of aging. The ductility of the 10h aged sample saw an increase to 10.8% from 9.5% in the CR state. Subsequent increase in aging duration saw an initial small decrease in ductility to 9.9% at 100h of aging and a drastic decrease to 2.2% at 1000h of aging. The Young's modulus of the samples increased steadily from 64.1 GPa in the CR state to 72.5, 80.3 and 92.3 GPa at 10, 100 and 1000h of aging. The Vickers hardness was increased from 252.3 HV to 304.9, 337.2, 354.9 HV respectively for the 10, 100 and 1000h aged state.

5.3. Discussion

Discussion of the results for this chapter is done collectively for both aging conditions. The results will be ordered such that one aspect of both aging conditions will be discussed in order, i.e. the thermal expansion of the 150 °C aged condition, then the thermal expansion of the 250 °C aged condition; before moving to the next aspect, such as the microstructural discussion.

5.3.1. Lattice and macroscale thermal expansion after 150 °C aging

Studies on binary Ti-Nb alloys of a range of compositions [42, 60, 61, 136] showed that the unit cell parameter *b*, directly corresponding to the d-spacing of $(020)_{\alpha''}$, increases with a decrease in Nb content at constant temperature. In the ex-situ XRD patterns of the aged samples in Fig. 5.2i, the leftward shift of the $(020)_{\alpha''}$ peak with increasing aging duration indicated an increase in d-spacing of the $(020)_{\alpha''}$ lattice plane according to Bragg's Law. This is evidence that diffusional rejection of Nb was able to occur in α" at a low aging temperature of 150 °C and progresses further with longer aging duration. Experimental studies on the lattice thermal expansion of Ti-Nb alloys across a range of compositions have also shown that Ti-Nb alloys with a lower Nb content exhibited lower NTE along the $[020]_{\alpha''}$ direction [2, 3]. The measured lattice NTE from in-situ XRD in Fig. 5.2g, h also showed that longer aged samples exhibited lower NTE magnitude, corresponding to a lower Nb content. Both

ex-situ measurements of the $(020)_{\alpha''}$ peak position and in-situ measurement of $(020)_{\alpha''}$ lattice NTE affirms that diffusional rejection of Nb occurs at 150°C and the extent of diffusion is closely related to the duration at this temperature.

Upon closer examination of Fig. 5.2g, an evident increase of lattice NTE can be observed from the CR state to the 10h aged state. This finding seemingly contradicts the previous explanation of diffusional rejection of Nb from the CR state to the 10h aged state, as the higher lattice NTE in the 10h aged state should suggest that the aged sample contains a higher Nb content. The increase in lattice NTE is likely attributed to the release of residual stress present in the CR state through the process of aging. Cold rolling of Ti-Nb alloys results in a texture of $[020]_{\alpha''}$ that is parallel to RD. However, this also imparts a residual stress that has been known to act along the RD in a tensile manner, parallel to $[020]_{\alpha''}$, and acts in opposition to NTE, hence reducing the magnitude of NTE. Relaxation of residual stress was achieved as a result of the combined effects of heating induced thermoelasticity and aging induced compositional change, manifesting increased lattice NTE in the 10h aged state. This behaviour aligns with a study done by Gehring [3] where Ti-Nb samples subjected to higher tensile pre-strain exhibited lower lattice NTE. Additionally, more insight can be shed from the position of the $(020)_{\alpha''}$ peak of the CR state as measured by ex-situ XRD in Fig. 5.2i. The $(020)_{\alpha''}$ peak in CR is situated at the smallest 2θ angle for the CR state, indicating the largest d-spacing of all the samples. This would suggest that the CR sample had the lowest Nb concentration between the aged samples, and hence should exhibit lowest lattice NTE. Instead, this contradicts the lattice thermal expansion behaviour measured in Fig. 5.2g, where CR exhibited the second highest lattice NTE. This suggests that while the imparted residual stress increased the lattice spacing of the parallelly aligned $(020)_{\alpha''}$ planes while slightly opposing the NTE of the α" phase by acting opposingly to the $[020]_{\alpha''}$ direction. Hence, the reason behind the discrepancy between the ex-situ $(020)_{\alpha''}$ peak position and in-situ lattice NTE of the CR state is not intrinsically compositional, but caused by external factors, namely the existence of a tensile residual stress stretching the $(020)_{\alpha''}$ plane and acting in opposition to NTE [137].

In Fig. 5.2j, an increase in intensity was observed between the two peaks $(020)_{\alpha''}$ and $(111)_{\alpha''}$, suggesting the growth of the $(011)_{\beta}$ peak situated right in between the two aforementioned peaks and an increase in phase fraction of β. Although this is likely a result of thermoelastic martensitic reversion via heating the sample to temperatures above A_s, it is unclear if diffusional rejection of Nb from α" could have resulted in the formation of β as this alloy is near the α"/ β composition limit. In this 2θ range, the occurrence of diffusion is also supported by the rightward shift of this group of peaks. Calculation of the peak positions of $(002)_{\alpha''}$ and $(111)_{\alpha''}$ in Ti-Nb of lower Nb concentrations was done using the reported lattice parameters and change in lattice parameter per unit concentration for Ti-Nb alloys [42, 60, 61, 120, 136] and presented in Fig. 5.15. The calculated peak positions of $(002)_{\alpha''}$ and $(111)_{\alpha''}$ do indeed show a significant rightward shift for $(111)_{\alpha''}$ while the peak positions of $(002)_{\alpha''}$ was almost insignificant, supporting the occurrence of diffusion. The intensity (I) of the calculated peaks was simulated using the proportional relationship as shown in Equation (5.1 between the intensity of the *hkl* peaks and the structure factor (F), the factor *s* which relates to the intensity of the radiation beam, *L* the Lorentz factor, and *p* the polarization factor [138].

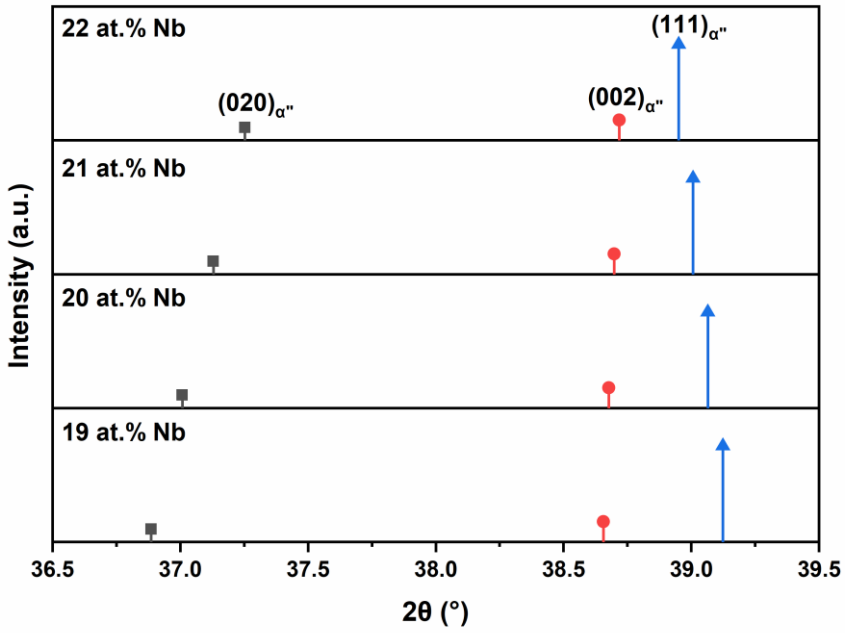

Fig. 5.15. (a) The calculated positions of peaks $(020)_{\alpha''}$, $(002)_{\alpha''}$ and $(111)_{\alpha''}$ in Ti-Nb from 19 at.% to 22 at.% Nb.

$$I(hkl) \propto |s \cdot Lp \cdot F(hkl)|^2 \tag{5.1}$$

$$p = \frac{(1 + \cos^2 2\theta)}{2} \tag{5.2}$$

$$L = \frac{1}{\sin\theta \cdot \sin 2\theta} \tag{5.3}$$

When looking at the correlation between loss of **macroscale** and **lattice** NTE, a direct proportionality was not observed. This comparison excludes the CR state due to the influence of residual stress that is only unique to this sample condition. When comparing the 10h and 1000h aged condition, the change in lattice NTE is larger when compared to the change in macroscale NTE. A loss of 4.7% **lattice** NTE was calculated between the 10h and 100h aged states, followed by a further 15.7% loss of **lattice** NTE between 100h and 1000h aging duration. In contrast, the sample experienced a 6.8% loss of **macroscale** NTE between the 10h and 100h aged state, followed by a comparatively small loss of only 3.4% **macroscale** NTE when aging progressed from 100h to 1000h. At the end of the aging process, the 1000h sample exhibited 90% of the **macroscale** NTE of the 10h sample. Meanwhile, the same sample exhibited 80% of the **lattice** NTE when compared to the 10h sample. This indicates that in aging, the loss of macroscale NTE was not solely dictated by the loss of lattice NTE. When looking at the sample as a whole, it is difficult to pinpoint the origin of the loss to any specific factor. One major reason could be attributed to the fraction of the sample that had reverted to β through reverse martensitic transformation, while minor reasons could be change in orientation density and residual stress relaxation affecting the final macroscale NTE of the sample.

Table 5.1. Measured comparison of lattice scale and macroscale NTE for the 150 °C aged states.

Duration aged at 150 °C	Macroscale NTE (ppm/°C)	Difference from previous condition (%)	Lattice scale NTE (ppm/°C)	Difference from previous condition (%)
10h	-22.2	-	-43.4	-
100h	-20.7	-6.8	-41.4	-4.7
1000h	-20.0	-3.4	-34.9	-15.7%

5.3.2. Precipitation of α"$_{iso}$ during 250 °C aging

In Fig. 5.10a-c showing the wide-range XRD of the 250 °C aged samples, positions of increased intensity corresponding to β peak positions indicate that the overall phase fraction of β had increased in the samples. This is most likely as a result of reverse martensitic transformation that occurs above A_s temperature of ~100 °C. When considering the prior $(020)_{\alpha''}$ texture of the sample, the significant increase in intensity of $(011)_{\beta}$ compared to other β peak positions can be rationalized according to the orientation relationship of $(020)_{\alpha''} \parallel (011)_{\beta}$. The gradual development of β phase throughout aging can be visualized by overlapping the in-situ XRD patterns of the aged and CR specimens heated to 250 °C (Fig. 5.16). Upon heating the CR sample to 250 °C, the diffraction pattern resembles a single peak of β phase as the unit cell tends towards the shape of a bcc unit cell with increasing temperature. However, it was apparent that the pattern cannot be described as a single peak according to the pseudo-Voigt function, a function combining the Lorentzian and Gaussian forms, used to for profile fitting of peaks. Instead, a left shoulder peak corresponding to α" phase was still detected, indicating that the sample was not a single β phase at this point. Upon overlapping the diffraction pattern of the 250 °C aged samples (Fig. 5.16), it is observed that the peak intensity of α" in the aged samples increased, and their positions shifted leftward with aging duration. The increase in intensity indicated that the phase fraction of α" had increased during isothermal holding, and hence pointed towards isothermal precipitation of α" (α"$_{iso}$). The leftward $(020)_{\alpha''}$ peak shift indicated continuous rejection of Nb throughout isothermal holding. Similar evidence for Nb diffusion was presented under ex-situ XRD in the positions of the $(020)_{\alpha''}$ peaks (Fig. 5.10i). At this point, it can be rationalized that throughout the isothermal holding process, α"$_{iso}$ could have be formed in the CR sample through three possible pathways: (i) α"$_{iso}$ precipitated from the sample which consisted of a significant fraction of β, which formed through reverse martensitic transformation, through localized rejection of Nb; (ii) The fraction of α" was retained at 250 °C rejected Nb resulting in a Nb lean form that approaches the concentration of α"$_{iso}$.; (iii) The retained α" at 250 °C gradually transformed into β, before

precipitating α''_{iso}. The competition between these pathways required further study that was not conducted in this thesis.

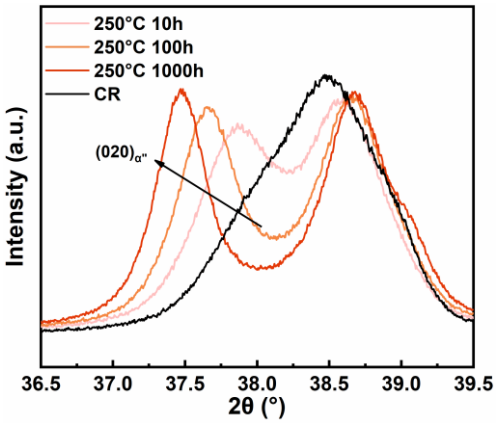

Fig. 5.16. (a) The evolution of peaks $(020)_{\alpha''}$, $(002)_{\alpha''}$ and $(111)_{\alpha''}$ between 36.5° and 39.5° from the CR state at 250 °C throughout aging for 10, 100, 1000h.

5.3.3. Lattice and macroscale thermal expansion after 250 °C aging

The change in NTE magnitude between the 250 °C aged samples was more drastic than the 150 °C aged samples. The least aged sample at 250 °C showed a lattice NTE that was lower in magnitude (-31.8 ppm/°C) than the longest 150 °C aged sample (-34.9 ppm/°C). This indicated that diffusional rejection of Nb had progressed further for the sample aged at 250°C for 10h compared to the sample aged at 150 °C for 1000h. Naturally, subsequent samples subjected to longer aging durations of 100h and 1000h at 250 °C also saw a gradual decrease in lattice NTE to -22.9 ppm/°C and -15.5 ppm/°C respectively.

Interestingly, when comparing samples aged for 10h at both temperatures, we see that the 250 °C aged sample exhibited lower NTE than the CR state, while the 150 °C sample contrarily exhibited higher NTE than the CR state. This indicated that the loss of NTE from diffusion in the 250 °C aged sample was higher than the NTE regained from the release of residual stress. Evidence of the release of residual stress observed in the 150 °C condition was also observed in the 250 °C aged sample in Fig. 5.10 With the release of tensile residual stress from aging, the $(020)_{\alpha''}$ lattice spacing decreased and peak position returned rightward in the 10h sample. Additionally, a shoulder peak seen at the rightmost of the 1000h aged diffraction pattern in Fig. 5.10j could be related to $(01\bar{2})_{\omega}$, but no other

evident ω peaks were observed. However, the morphology of the large ω precipitates was well captured under DF TEM in Fig. 5.11c, confirming the presence of ω precipitates.

Hence, we can conclude that the low, or zero thermal expansion achieved in the sample aged at 250 °C for 1000h was a combination of the effects of reduced α" phase fraction from reverse martensitic transformation, concurrent precipitation of α''_{iso}, and reduction of lattice NTE by diffusion. Another possible factor that could affect the exhibition of NTE is the strength of texture. A characterization of this could be through an orientation distribution function (ODF) that was not performed in this study.

5.3.4. Microstructural and mechanical behaviour after aging at 150 °C

Although ω precipitates were clearly imaged in the aged samples, XRD did not reveal any peaks that could have been attributed to the ω phase. As mentioned in Section 4.2.3, weak or absence of ω peaks are common. Even in studies studying the isothermal aging of the ω phase at favourable growth temperatures, the XRD peak intensities are usually low in intensity and hard to detect [44, 139] unless opting for techniques such as synchrotron [140]. Compared to the isotropic samples in other studies, a textured sample in this study severely limits the already hard-to-detect ω peaks. In a textured sample, reflections of ω satisfying Bragg's Law are severely limited, and any weak ω intensities that could have arisen could also be drowned by the widened existing α" peaks, leading to the absence of ω peaks. This applies to samples isothermally aged at 150 °C and 250 °C.

The DF TEM image of the sample aged at 150 °C for 10h presented in Fig. 5.4 revealed ω_{ath} particles that were measurably larger than the ω_{ath} particles in the CR state. This indicated promoted growth of ω_{ath} particles during aging from the CR to 10h aged state. These high strength ω_{ath} particles have been known to act as impairments to dislocation glide during deformation, thus attributing to the increase in Young's modulus, ultimate tensile strength, and reduction in ductility. Further aging to 100h resulted in an SAED pattern lacking distinct ω diffraction spots at the ideal positions and DF imaging (Fig. 5.5a) shows a sparse distribution of ω. A hypothesis may be reached that the previously seen ω_{ath} seen in the 10h aged state was destroyed during aging to the 100h mark. Instead, new isothermally formed ω_{iso} were observed. Although the decomposition of ω has been widely studied under constant

temperature or slow heating conditions [117, 125, 126, 139, 141] (both of which are classified under isothermal conditions), virtually no study has reported the destruction of ω under these extremely long low temperature conditions. This highlights the uniqueness and necessity for this study of prolonged aging in expanding our understanding of the metallurgy of metastable β Ti alloys. The formation of isothermally precipitated ω is not uncommon at temperatures as low as 150 °C. In a recently proposed phase diagram by Bönisch [40], the temperature for ω formation was predicted to lie around 130 °C and indeed, the precipitation of ω_{iso} has been detected through resistometric methods at temperatures as low as 150 °C [142, 143]. Additionally, ω_{iso} has been found to precipitate around defects formed from the reversion of previously athermally formed ω_{ath} into β [142, 143].

The replacement of grown ω_{ath} precipitates with fine ω_{iso} was reflected in the significant dip in Young's modulus and a significant increase in ductility from 10h to 100h aging (Fig. 5.8). Extremely fine ω_{iso} precipitates have been reported to increase ductility and increase strength in Ti alloys [144-146]. Ductility was improved through the destruction of commensurate ω due to the reduced dislocation impairment ability of fine ω_{iso} precipitates, which contrasts the commonly held belief that the ω phase is generally detrimental to ductility. The strength of the alloy was improved through the increase in phase fraction of high strength ω in the overall alloy composition. The observed DF morphology of this fine ω_{iso} in the 100h aged sample is very similar to ω embryos described by Devaraj et al. in a similar β-isomorphous Ti-Mo alloy [70], where compositional partitioning caused localized differences in atomic composition that was observed under HAADF-STEM mode and later confirmed by atom probe tomography (APT). Some of these studies suggest that the mechanism behind the formation of ω_{iso} involves the rejection of β stabilizer (in this case, Nb) into the surrounding matrix and hence changing the deformation mode of the alloy to TWIP (twinning induced plasticity) through β stabilizer enrichment of the surrounding matrix, resulting in an increase in ductility [144, 146].

In 1988, a novel idea proposed by Morinaga et al. [147] proposed two new parameters, $\overline{Bo}$ and $\overline{Md}$, to predict phase stability for Ti alloys by creating a figure consisting of zones attributed to deformation modes as a guideline for designing Ti alloys with properties such as superelastic, shape memory etc.

The parameter Bo is the bond order, which describes the covalent bond strength between Ti and the alloying element, while Md quantifies the energy level of the d-orbital in metal atoms [148]. The averaged values, $\overline{Bo}$ and $\overline{Md}$, of an alloy are calculated from its compositional averages of Bo and Md. The illustration in Fig. 5.17 shows the deformation modes of Ti alloys as characterized by the $\overline{Bo} - \overline{Md}$ figure by Morinaga [147]. Annotated by dashed arrow lines, the trend of $\overline{Bo} - \overline{Md}$ of an alloy with increasing β stabilizer concentration is visualized starting from pure Ti according to five commonly used β stabilizers. This shows that the deformation mode of a Ti alloy can be changed to TWIP from the martensitic region as their $\overline{Bo} - \overline{Md}$ increases from enrichment of β stabilizer content. This increase in ductility was seen in Fig. 5.8a, where the 100h aged sample showed the highest ductility of the four samples presented. Due to the scope of this study, EBSD and SAED characterization of the sample after tensile tests were not performed to confirm the existence of twinning. However, the tensile behaviour of the sample and HRTEM analysis in Fig. 5.5 gives reasonable basis for the hypothesis of the formation of ω_{iso} in the 100h aged sample.

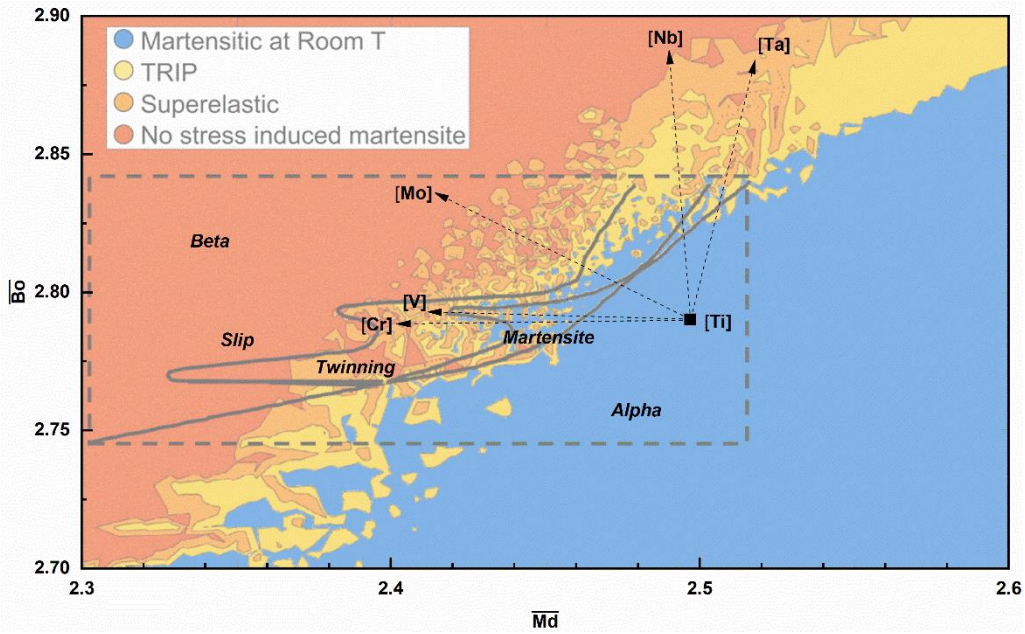

Fig. 5.17. The $\overline{Bo} - \overline{Md}$ figure by Morinaga [147] and adapted by Bignon [149] shows the starting point of pure Ti, and their position on the figure with increasing β-isomorphous stabilizer concentration.

In Fig. 5.6b, the appearance of the highlighted circular streaks in the 1000h aged sample has been reported to be caused by the movement of the two ω variant spots towards each other [132]. In more

drastic cases, such diffraction streaks can appear as fully circular diffraction streaks instead of the arc seen in Fig. 5.6b. The sample conditions that contribute to these circular streaks vary from solution treated to cold-rolled [68, 150]. However, the appearance of these circular streaks has been unanimously attributed to the ω phase. These ω, however, have been termed differently according to different authors, such as "initial ω-structures", "ω-like structures" or "incommensurate ω". In the inverse FFT analysis of these circular streaks (Fig. 5.6f), the lattice spacing measured corresponds to that of ω along the $[111]_\beta$ and $[11\bar{1}]_\beta$ directions. In a study by Jones [132], it was suggested that the movement of the ω variant diffraction spots towards each other and forming a circular streak was caused by the coupling of strain fields within the sample. This explanation, however, can be safely eliminated in our study, as aging for 1000h would have allowed sufficient time for stress, and therefore strain, relaxation. With prior knowledge that diffusion occurs during aging, attention should be diverted to the chemical stability of the phases in question.

The suppression of ω in Ti-Nb alloys of high Nb content has been well documented [151, 152]. The high Nb content chosen to achieve high NTE magnitude in our sample (22 at.%) is at the cusp of instability of ω, where higher contents of β stabilizer would lead to gradual instability and limit ω formation. Sightings of these circular ω-like diffraction streaks report that the chemical stability of ω and the surrounding β matrix as the reason for their formation [131, 134, 150, 153]. In some studies, the increase in β stability of the surrounding matrix has been known to shift the ideal ω diffraction spots into incommensurate diffuse streaks [154-157]. In searching for an explanation for the shift in the ω diffraction spot, Sinkler and Luzzi proposed a model and suggested that chemical short-range ordering of ω as the reason [150]. When extra partially-collapsed planes are added to the expected $\omega_{(3)}$ structure, a short ranged extended $\omega_{(5)}$ or $\omega_{(7)}$ structure is formed and thus resulting in the shifted diffraction pattern. The magnitude of the shift was correlated to stabilizer concentration, with higher concentrations contributing to larger shifts in the diffraction spot from their commensurate positions. In our study, prolonged aging duration from 100h to 1000h likely allowed sufficient time for the slow diffusion of Nb [42] to take place and allowing the incommensurate ω in the 100h state to grow into commensurate ω in most areas of the sample (inset of Fig. 5.6a). However, in some areas, short-range

extended ω structures from the incommensurate state still continue to develop through nanometer scale localized rejection of Nb, hence forming the circular ω diffraction streaks seen.

Compositional partitioning leading to the formation of ω_{iso} can be affirmed through its exhibited mechanical behaviour as well. In a first principal computation study by Salloom et al. [158], ω_{iso} formed via compositional partitioning was found to exhibit higher strength. Among the four samples in Fig. 5.8, the 1000h aged sample exhibited the highest ultimate tensile strength and Young's modulus. Although CSRO has been quoted to strengthen certain high entropy alloys, the increase in tensile strength is likely due to the aforementioned larger ω_{iso} precipitates acting as dislocation impairments. The effect of this can be seen as well in the reduced ductility of the 1000h aged sample from the 100h aged state.

Combining the observations of the development of ω under isothermal aging at 150 °C, the development of the ω phase from the CR state to the 1000h aged state can be summarized in Fig. 5.18. (1) Firstly, ω_{ath} starts off as mostly globular precipitates in the CR state. (2) Upon aging at 150°C for 10h, the ω_{ath} grows in size. (3) Further aging to 100h causes the ω_{ath} in the 10h state to be destroyed and replaced with incommensurate ω_{iso} which show up as diffuse streaks under SAED. Further prolonged aging at this temperature to 1000h causes ω_{iso} to undergo several stages of progression. (4) A fraction of ω_{iso} that sees slower growth develops into short-ranged order precipitates and show up as circular streaks under SAED. (5) Portion of ω_{iso} that has developed further show up as disc-shaped precipitates and presents under SAED as thin streaks between the commensurate ω and α" positions. (6) Finally, majority of the ω_{iso} grow into ellipsoidal shaped precipitates as shown in Fig. 5.6a.

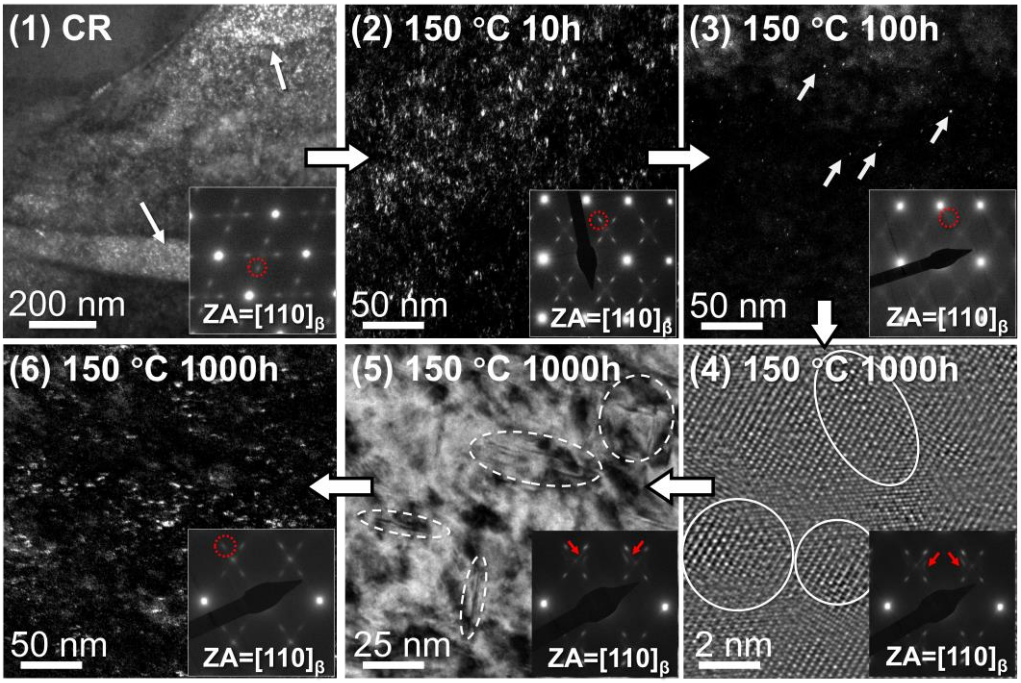

Fig. 5.18. Evolution of the ω phase throughout aging at 150 °C from the CR state.

5.3.5. Microstructural and mechanical behaviour after aging at 250 °C

Unlike the erratic ductility trend observed in the 150 °C aged samples, the ductility of the samples aged at 250 °C show a predictable unidirectional trend. An initial increase in ductility is seen from the CR state to the 10h aged state (9.9%), this is different from the low ductility exhibited by the least aged sample at 150 °C (6.0%). As determined from the lattice NTE, the Nb content of β matrix in the sample aged at 250 °C for 10h is higher than the Nb content of the longest aged 150 °C sample due to a more progressed Nb diffusion process in the 250 °C aged sample. From the $\overline{Bo} - \overline{Md}$ figure (Fig. 5.17), this pushes this 250 °C aged sample further into the TWIP region which exhibits increased ductility. Indeed, this sample has comparable ductility to the sample aged at 150 °C for 1000h (8.5%). The difference in ductility, however, could be the product of phase fraction and size of the ω precipitates. The growth and precipitation rate of ω is known to be affected by temperature and time [125, 139, 140, 159-161]. The size of ω of the sample aged at 150 °C for 1000h is comparable to the sample aged at 250 °C for 10h. The difference in ductility could mean that the size and phase fraction of ω in the sample aged at 150 °C for 1000h is higher. Subsequent increase in aging duration to 100h at 250 °C shows a slight decrease in ductility due to increase in ω phase fraction while the ω particle

sizes are imaged to be roughly the same. The plastic deformation region still persists at high strain showing good deformability in this sample. At 1000h of aging, the plastic deformation region is virtually non-existent, as the ultimate yield stress is the stress at which fracture occurs due to the large ω precipitates rendering the material brittle. The unidirectional increase of the Young's modulus and Vickers hardness of the 250 °C aged samples can be attributed to the continual precipitation and growth of ω precipitates. Although favourable isothermal conditions have been utilized to promote the growth of ω and leading to distinguishable ω peaks [126, 139, 140, 162], distinct ω peaks were not found in isolated angles. The obscuring of ω peaks could be accentuated by the preferred orientation and peak broadening induced by cold rolling even though concrete evidence of ω was seen under TEM. A summary of the observed results is shown in the table below.

Table 5.2. Summary of the average macro NTE, lattice NTE and TEM observations of the aged samples in this chapter.

Aging temperature (°C)	Aging duration (hours)	Average macro NTE (ppm/°C)	Average lattice NTE (ppm/°C)	TEM observations
Cold-rolled state	-	-25.5	-41.5	Acicular martensite, ellipsoidal ω_{ath}
150	10	-22.2	-43.4	Growth of ellipsoidal ω_{ath}
	100	-20.7	-41.4	Destruction of ω_{ath}, precipitation of incommensurate ω_{iso}
	1000	-20.0	-34.9	Growth of incommensurate ω_{iso} into disc precipitates, and further into ellipsoidal precipitates
250	10	-7.4	-31.8	Growth of ω_{ath} into large ellipsoidal precipitates. Destruction and precipitation not observed
	100	-2.2	-22.9	
	1000	-0.3	-15.5	

5.3.6. NTE performance of aged CR Ti-22Nb alloys

In Fig. 5.19, the Young's modulus and CTE of common alloys and the low thermal expansion Fe-Ni (Invar) alloy was adapted from Ashby [163], and the specific modulus of these alloys were calculated from the average density of commercial alloys from [164]. The low average CTE value of -0.29 ppm/°C achieved in this study is comparable to the CTE of Invar alloys of ≤ 2 ppm/°C at 400K (127 °C) [124]. The strength of Ti-22Nb alloys, however, is still lacking compared to Fe-Ni alloys even after prolonged promoted growth of ω_{iso} following aging at 1000h for 250 °C. The density of Ti-22Nb was obtained experimentally to be a value of 5890 (±100) kg/m^3. The strength of 150 °C aged alloys fluctuate minutely but its strengths lie in exhibiting significant NTE. The 250 °C alloys were significantly strengthened from aging and ZTE was achieved. When considering the weight of Ti-22Nb, the 250 °C aged samples have comparable specific moduli when compared to the well-known Invar alloys. This puts Ti-Nb alloys as a competitive material candidate when lightweight is of importance in applications such as wearable technology, optical alignment and aerospace applications where dimensional accuracy, strength and low weight are highly valued.

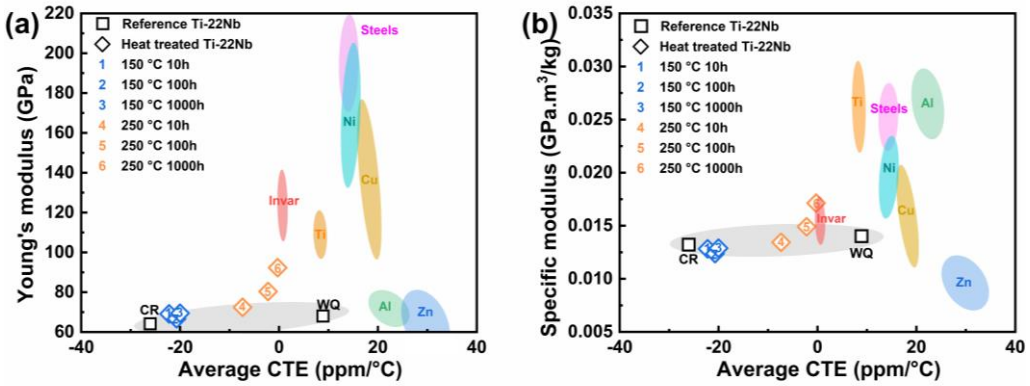

Fig. 5.19. Comparison of the (a) Young's modulus and (b) specific modulus against average CTE of aged Ti-22Nb alloys against commercial alloys.

5.4. Summary

In this chapter, the effect of sustained high temperatures above A_s on the NTE behaviour and mechanical properties of CR Ti-22Nb was studied through isothermal aging for 10, 100, 1000 hours at

150 °C and 250 °C. Aging at 150 °C for 10h sees an initial increase in NTE due to the release of the tensile stress induced by cold work opposing lattice NTE, then decreases minorly subsequently for each tenfold in aging time. Aging at a higher temperature of 250 °C sees drastic continuous decrease in NTE at every increase in aging duration. A remarkable ZTE was achieved after aging at 250 °C for 1000h. In both cases, diffusional rejection of Nb was observed through change in lattice NTE through in-situ XRD. A delicate opportune balance of Nb diffusion, concurrent precipitation of α''_{iso} and reverse martensitic transformation achieved macroscale ZTE. An irregular trend in ductility was observed in the 150 °C aged series was attributed to the dissolution of initial athermal ω at 10h aging, and the formation of isothermal ω observed via HRTEM at 100h and 1000h that reintroduced ductility. This irregular trend in ductility was not observed in the 250 °C aged series and a unidirectional loss of ductility was attributed to the continuous growth of ω.

6. Evolution of macroscale NTE in a cold-rolled Ti-Nb alloy through thermal cycling

6.1. Introduction

The contraction of CR Ti-22Nb was shown in Chapter 4 to reach a maximum at 320 °C before conversely exhibiting PTE behaviour at subsequent higher temperatures. Metastability in β Ti alloys consists of complex phase transformation pathways that could lead to the loss of NTE in material. Hence in this chapter, the mechanics behind the evolution of thermal expansion and mechanical properties of CR Ti-22Nb thermally cycled to 350, 450, 550 °C were investigated. In this chapter, the sequence of phase transformations occurring in CR Ti-22Nb during heating were characterized using a combination of ex- and in-situ XRD to reveal the changes to overall phase composition. These results were further supported by microstructural observations and changes in mechanical properties.

6.2. Results

6.2.1. Macroscale thermal expansion

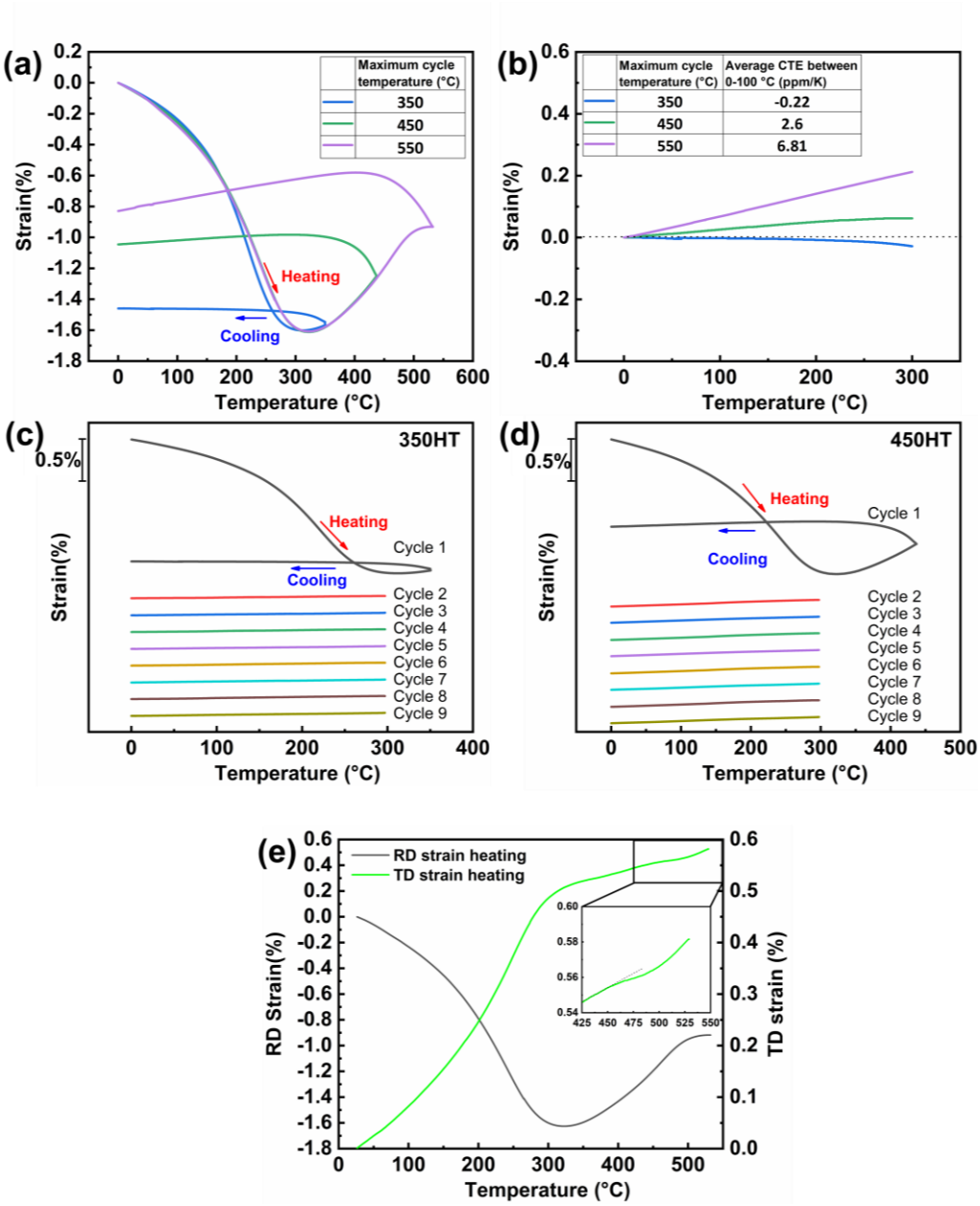

Fig. 6.1. (a) Macroscale thermal strain of CR Ti-22Nb along RD heated to maximum cycle temperatures of 350 °C, 450 °C, 550 °C and cooled down at temperature change rate of 3 °C/min. (b) Macroscale thermal strain of the thermal cycled samples. Individual thermal strain and thermal stability within eight thermal cycles heated to 300 °C of (c) 350HT and (d) 450HT. (e) Comparison of thermal strain along RD and TD of a CR Ti-22Nb.

The RD thermal strain of CR samples under single thermal cycles starting from 0 °C to maximum temperatures of 350 °C, 450 °C and 550 °C then cooled down to 0 °C is shown in Fig. 6.1a. The exhibited strain was fairly linear below temperatures ~100 °C but experienced a rapid increase in NTE

upon heating above 100 °C. Before reaching 300 °C, the gradient experiences a gradual positive increase and achieved zero gradient corresponding to maximum negative strain at about 320 °C. The positive increase in gradient persisted to about 500 °C, where a dip was observed for a short temperature range. This decline in gradient was observed to continue up to the maximum temperature of 550 °C before the sample was cooled. Upon being cooled to RT, the heat-treated samples were termed 350HT, 450HT and 550HT respectively, and their thermal strain responses were shown in Fig. 6.1b. The average CTE between 0-100 °C of the 350HT, 450HT and 550HT samples were measured to be -0.22, 2.6 and 6.81 ppm/°C respectively. The thermal stability of the HT samples was demonstrated by heating the samples from 0-300 °C for eight cycles in Fig. 6.1c-d. Within the eight heat cycles performed within this temperature range, the standard deviation of average CTE between 0-100 °C was measured to be ± 0.11 ppm/°C and ± 0.28 ppm/°C for the 350HT and 450HT samples respectively. The cyclic stability of the thermal strain response of 550HT was not considered here because its thermal expansion is largely positive and akin to conventional α+β Ti alloys and not of interest [124]. The strain at 0 °C measured for the 350HT sample between the eight cycles were between 0% to -0.008%, while the strain at 0 °C measured for the 450HT were ±0.003%.

In addition to the thermal strain along RD, the thermal strain response of the CR sample along TD from 25 °C to 550 °C was also measured in Fig. 6.1e and overlapped with the RD strain. In this figure, the 0% thermal strain along RD was adjusted to start from 25 °C instead of 0 °C to maintain comparability. Between the two measured directions, changes to the gradient of the curve that indicate phase transformation were seen to happen at around the same temperatures. Between 0-300 °C, where an increasingly negative strain gradient was seen along RD, an increasingly positive strain gradient was seen along TD. Before reaching 300 °C, where the RD strain curve gradient increases positively, similarly a change in gradient was seen in the TD curve. Lastly before reaching 500 °C, where a significant decrease in gradient is seen along the RD strain, a small change in gradient can be seen along the TD strain and is shown in the inset of Fig. 6.1e. The temperatures at which these gradient changes occur will be used to discuss phase transformations occurring in the sample in later sections.

6.2.2. X-ray diffraction

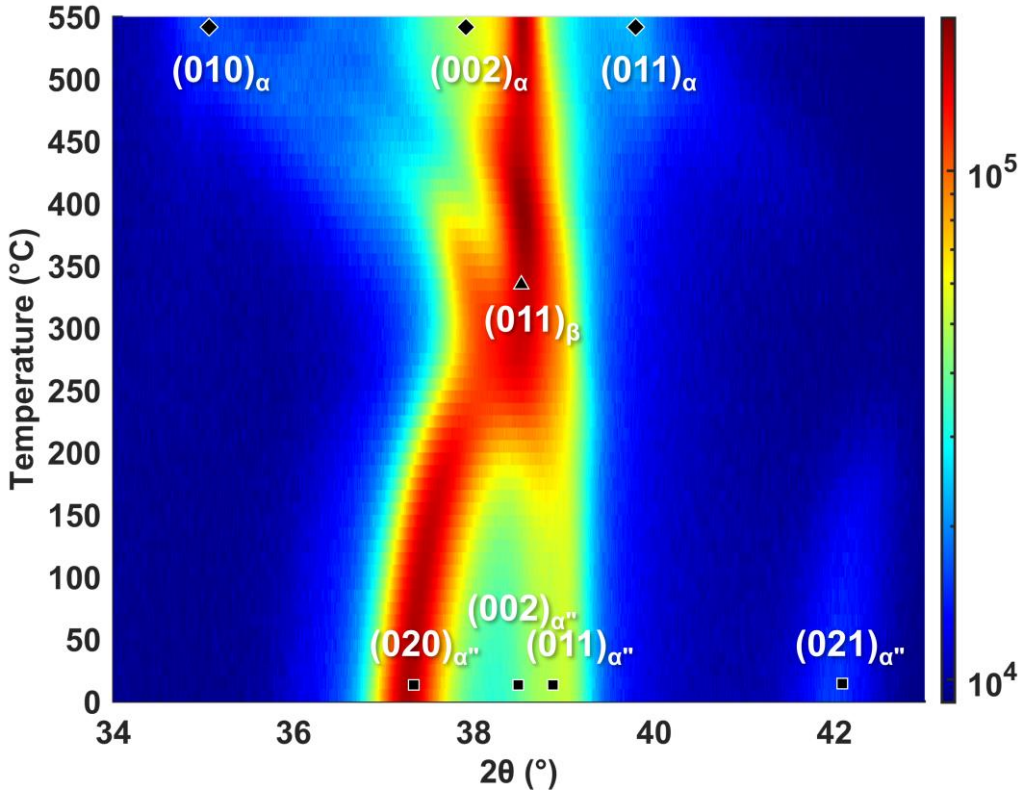

Fig. 6.2. In-situ XRD of CR Ti-22Nb heated from 0-550 °C from 2θ between 34-42.5°. The intensity is represented with the colour bar.

To visualize changes in phase constitution during heating, in-situ heating XRD of the CR sample was performed with a sectioned face normal to RD (Fig. 6.2). In this figure, the start of each subsequent scan was 10 °C apart and the heating rate used is consistent with experiments at 3 °C/min. Similar to XRD results in Chapter 5, since changes in the XRD pattern outside of 43° do not change significantly, only the 2θ range from 34° to 43° will be presented. The intensity of the signal at any specific 2θ angle is represented with the colour bar presented in log scale. At 0 °C, characteristic peaks of the martensitic α" were observed and indexed in the figure. Heating the sample saw expected results where the characteristic $(020)_{\alpha"}$ and $(021)_{\alpha"}$ peaks shift rightward indicating NTE, while the $(002)_{\alpha"}$ and $(011)_{\alpha"}$ peaks shift slightly leftward indicating PTE. With increasing temperature, the two PTE peaks $(002)_{\alpha"}$ and $(011)_{\alpha"}$ slowly merged into one significant peak indexed as $(011)_{\beta}$. The $(020)_{\alpha"}$ peak exhibited NTE up to around 320 °C, after which the peak does not continue to shift rightward to merge into the $(011)_{\beta}$ peak with increasing temperature. Instead, the $(020)_{\alpha"}$ peak

shifted leftward after 320 °C. This leftward peak shift persisted up to 550 °C. At around 450 °C, a second leftward shift of intensity was observed coming from the dominant $(011)_{\beta}$ peak. At the highest temperature of 550 °C, characteristic α peaks were indexed alongside the obvious β peak. The in-situ cooling XRD patterns during subsequent cooling upon reaching maximum temperatures of 350, 450, 550 °C did not involve complex dynamic changes, and thus was not presented in a continuous format. Instead, the in-situ XRD patterns of the CR sample at these maximum temperatures were presented together with the respective cooled HT patterns at room temperature in Fig. 6.3a-c. In Fig. 6.3a, cooling of the CR sample after reaching 350 °C resulted in the $(020)_{\alpha"}$ peak to shift largely leftward and increase in intensity, while the $(011)_{\beta}$ peak shifted rightward indicating typical PTE behaviour and a slight decrease in intensity. Cooling the CR sample from 450 °C in Fig. 6.3b saw shoulder peaks develop to the left and right of the dominant $(011)_{\beta}$ peak, with the left pair being more noticeable. The developed intensities in these ranges were more visibly seen in Fig. 6.2. These peaks were confirmed to both be $(020)_{\alpha"}$, but the peak further left was denoted as $\alpha"_{lean}$ while the other $\alpha"_{rich}$. However, the context of "rich" and "lean" α" is explicitly only used when discussed in the context of the 450HT sample, and later the 550HT sample. Cooling the CR sample from 550 °C in Fig. 6.3c saw the aforementioned left shoulder peak develop into two visible peaks at ~36.25° and ~37.25°, with the two leftmost peaks being indexed as $(010)_{\alpha}$ with "lean" and "rich" subscripts similar to 450HT. Meanwhile, a prominent shoulder peak had formed to the left of the dominant $(011)_{\beta}$ peak that was indexed as $(002)_{\alpha}$. The peak formed to the right of the β peak was indexed as $(011)_{\alpha}$. Through in-situ XRD in Fig. 6.2, the previously calculated $(020)_{\alpha"}$ thermal lattice strain of the CR sample in Chapter 5 was calculated and extended to 300 °C. Above 150 °C, the negative gradient of the $(020)_{\alpha"}$ thermal lattice strain showed a gradual negative rate of change, but sees a sudden significant positive increase in rate of change of gradient before 300 °C and gradually reaches a zero gradient state at ~300 °C, after which the peak "rebounds" and shifts left, as seen in Fig. 6.2. The $(020)_{\alpha"}$ lattice thermal strain of 350HT and 450HT were calculated and presented in Fig. 6.3d and results of CR samples aged at 250 °C were included for comparison. In the same figure, the lattice thermal strain of the two supposed $(010)_{\alpha}$ peaks labelled lean and rich for the left and right peaks in

Fig. 6.3c respectively, were also included in the same scale as the $(020)_{\alpha''}$ lattice thermal strain due to the orientation relationship of $(020)_{\alpha''} \parallel (010)_{\alpha}$. Shown in Fig. 6.3e, a slight but detectable leftward shift upon heating from 0 °C to 300 °C (indicated by the arrow) confirmed that these two peaks exhibit PTE, albeit slight, as opposed to the NTE of the α" phase.

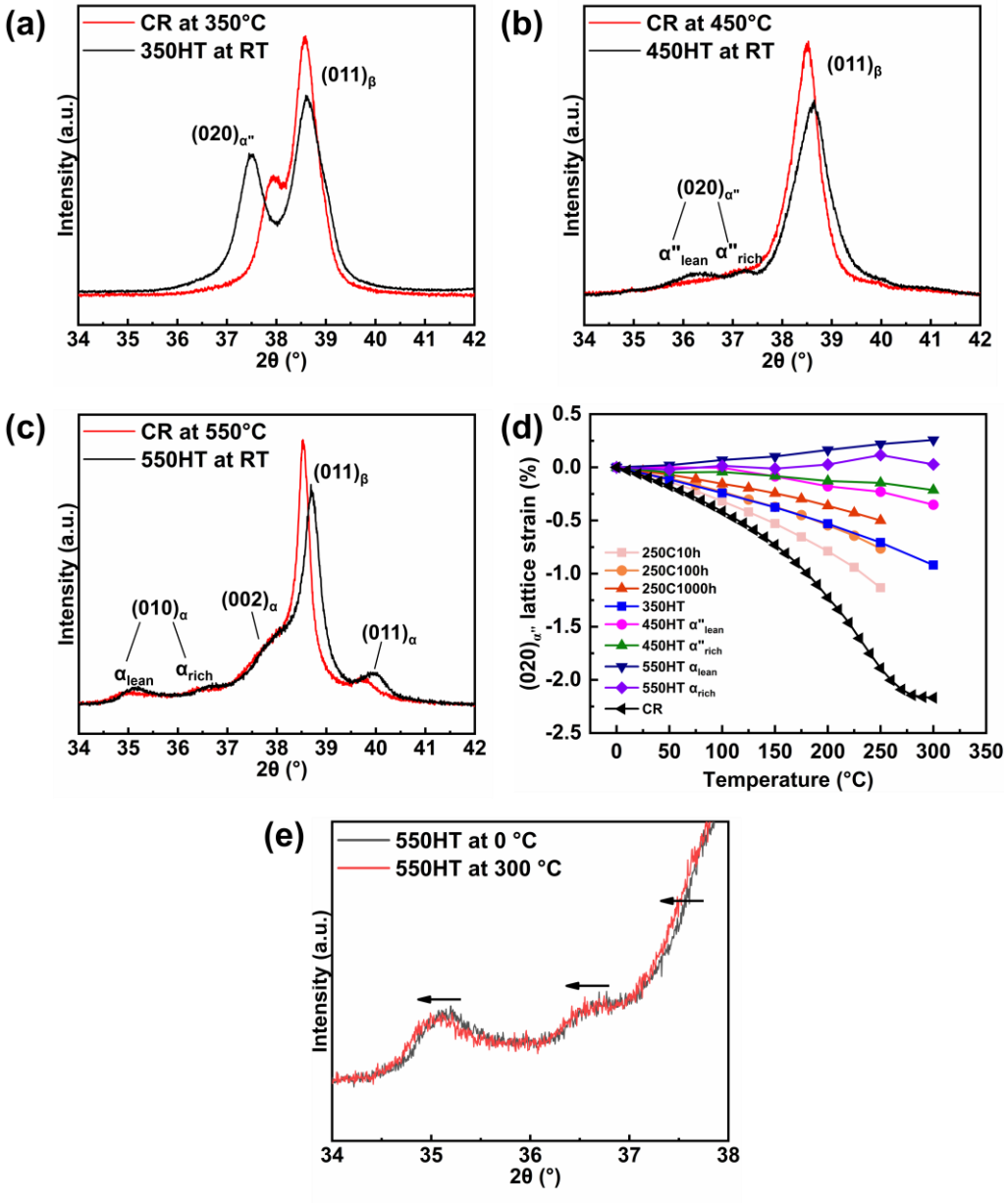

Fig. 6.3. Comparison of CR Ti-22Nb at (a) 350 °C, (b) 450 °C, (c) 550 °C and each respective HT state at RT. (d) Lattice thermal expansion of $(020)_{\alpha''}$ in 350HT, 450HT and 550HT compared with the 250 °C aged states from Chapter 5.

6.2.3. Microstructural characterization.

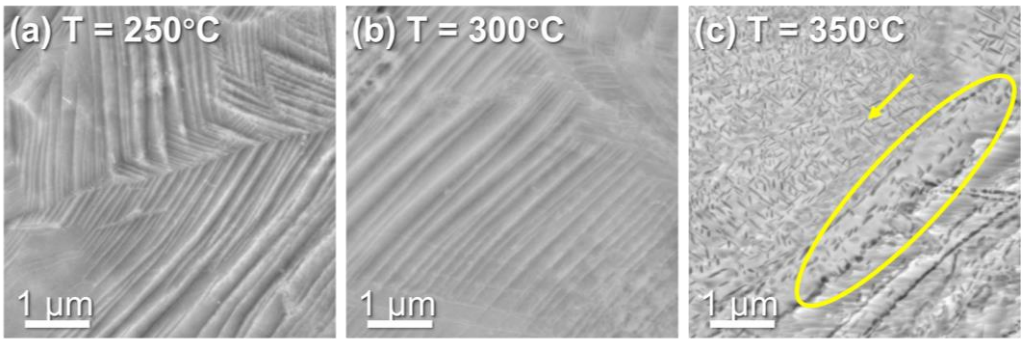

Fig. 6.4. SEM micrographs of CR Ti-22Nb heated to (a) 250 °C, (b) 300 °C, (c) 350 °C and cooled to RT.

To envision the gradual change in microstructure under heating, three separate CR samples were heated to maximum temperatures of 250, 300, 350 °C and cooled to room temperature with the same rate of temperature change of 3 °C/min. The microstructure of these thermally cycled samples were then captured under SEM (Fig. 6.4). The face viewed under SEM was sectioned normal to the RD. A uniform microstructure of deformed lathes was observed in the samples heated to a maximum temperature of 250 and 300 °C as seen in Fig. 6.4a, b. However, numerous fine precipitates were observed in the sample heated to 350 °C. These precipitates were observed along the prior grain boundaries (circled in yellow) and within the grains (indicated by the arrow). Precipitates along the boundary showed a more globular shape compared to the acicular appearance of precipitates within the grain. Dimensions along the major axis of these precipitates measured from approximately 50 to 400 nm, with the lower end contributed by the globular precipitates and the longer ones contributed by the acicular precipitates. Further inspection of the precipitates in the 350HT sample was performed using EBSD and EDX under Transmission Kikuchi Diffraction (TKD) mode in SEM (Fig. 6.5). Using EBSD, the phase of the precipitates and matrix were identified to be α" and β respectively. The orientation of grains in this same area is presented in Fig. 6.5c by referring to the left inset inverse pole figure (IPF). The orientation relationship between α" and β of $(011)_\beta \parallel (010)_{\alpha"}$ was confirmed by selecting a small area in the EBSD image including the precipitate and matrix and shown as the right inset of Fig. 6.5c. Majority of the precipitates showed an orientation of $(010)_{\alpha"}$ while the matrix showed a single orientation of $(011)_\beta$. This demonstrates preservation of the Burgers orientation

relationship within the material while heated to 350 °C. The element distribution was also imaged in the same area using EDX and presented in Fig. 6.5d. Given that two elements can exist at every position in the image, the element returning the highest count was presented in Fig. 6.5d. Distribution of individual elements can be separated from this image into Fig. 6.5e-f representing Ti and Nb respectively. In these images, the precipitates corresponding to the α" phase correspond to Ti-rich and consequently Nb-lean spots.

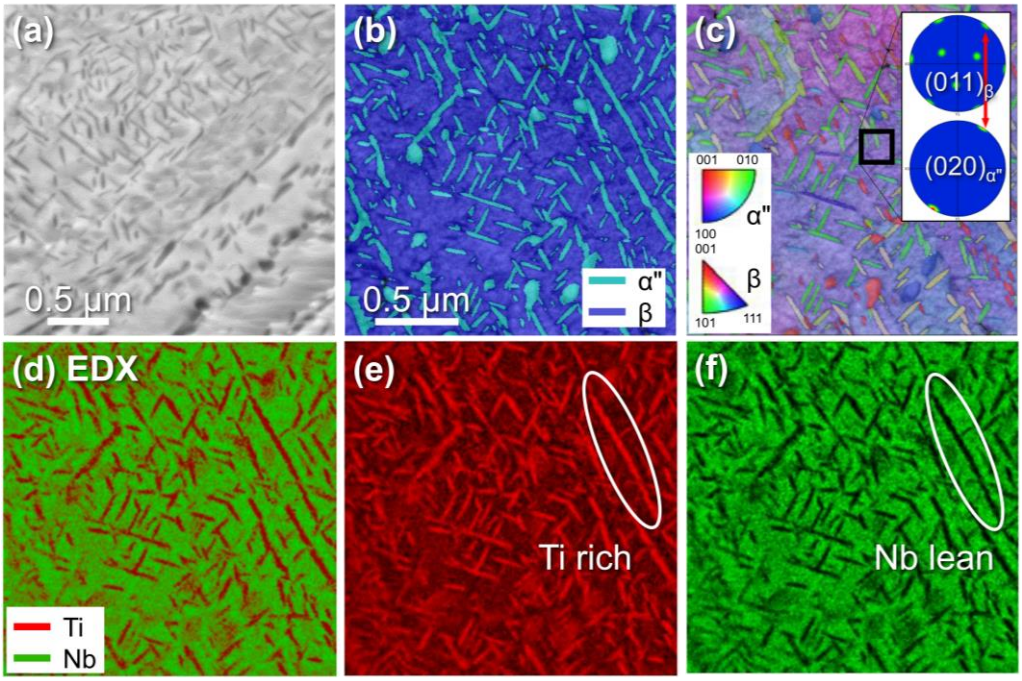

Fig. 6.5. (a) Enlarged micrograph showing precipitates in 350HT state. (b) Phase map of 350HT. (c) EBSD grain orientation map. EDX showing (d) majority element distribution, (e) Ti distribution, (f) Nb distribution.

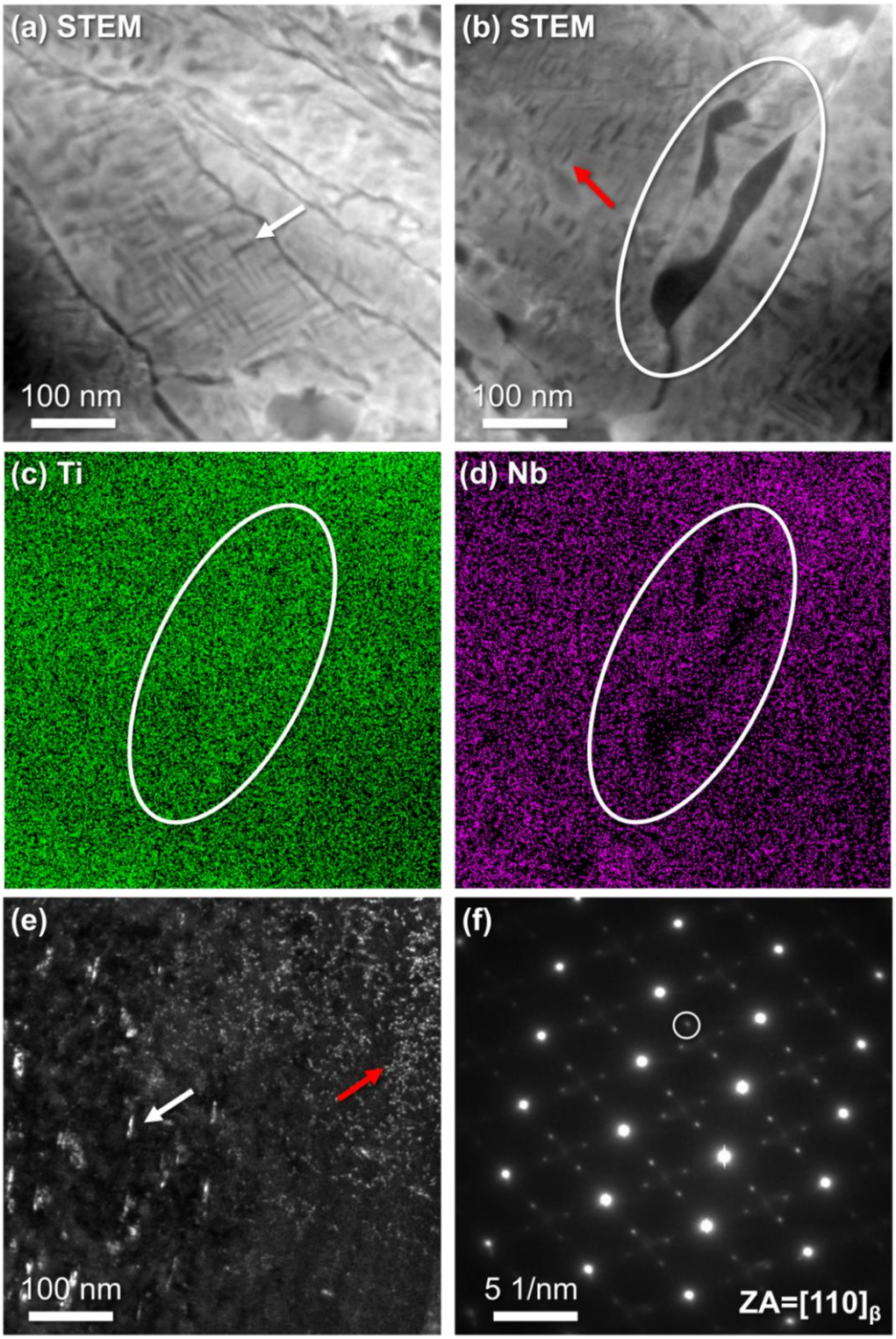

Fig. 6.6. STEM micrograph of 450HT showing (a) intersecting acicular structures and (b) parallel structures and grain boundary precipitates. EDX was performed on the same area as (b) and found the (c) Ti distribution to be fairly even while (d) Nb distribution shows a lean area corresponding to the grain boundary precipitates. (e) DF TEM of the 450HT sample using the selected ω diffraction spot in (f) showed two morphologies, ellipsoidal and globular side-by-side.

In Fig. 6.6a and b, STEM was performed on the 450HT sample on a sectioned face normal to RD. In these areas, fine acicular precipitates were observed in basket-weave and parallel structures indicated by white and red arrows respectively. Additionally, thin layers of precipitate and large globules were found along the grain boundary. In Fig. 6.6c and d, EDX revealed that the globular precipitate found in Fig. 6.6b was lean in Nb, while the concentration of Ti remained fairly even. In Fig. 6.6e, the morphology of the ω phase in 450HT was characterized by DF imaging using the diffraction spot circled in Fig. 6.6f. Two distinct morphologies of ellipsoidal and fine globular ω were observed across multiple areas of the sample indicated by white and red arrow respectively in Fig. 6.6e.

Finally, the morphology of the 550HT sample was characterized under SEM and presented in Fig. 6.7. In these micrographs, two types of morphologies are seen. Along the grain boundaries of both images in Fig. 6.7, precipitates were observed to form in a thin intergranular layer or in globular forms between grain boundaries and match descriptions of intergranular α phase formed between β grains [165-174]. Whereas within the grains, two types of acicular structures were seen and presented in Fig. 6.7a. The first acicular structure is indicated by the white arrow of straight needle-like intersecting structures, while the morphology in the neighbouring grain indicated by the red arrow shows lamellar structures that suggests that it could be formed from spinodal decomposition [87, 175, 176]. A wider area of these lamellar structures was found in another grain and enlarged in Fig. 6.7b. The wavy nature and uneven widths indicate that these structures may have been formed through spinodal decomposition.

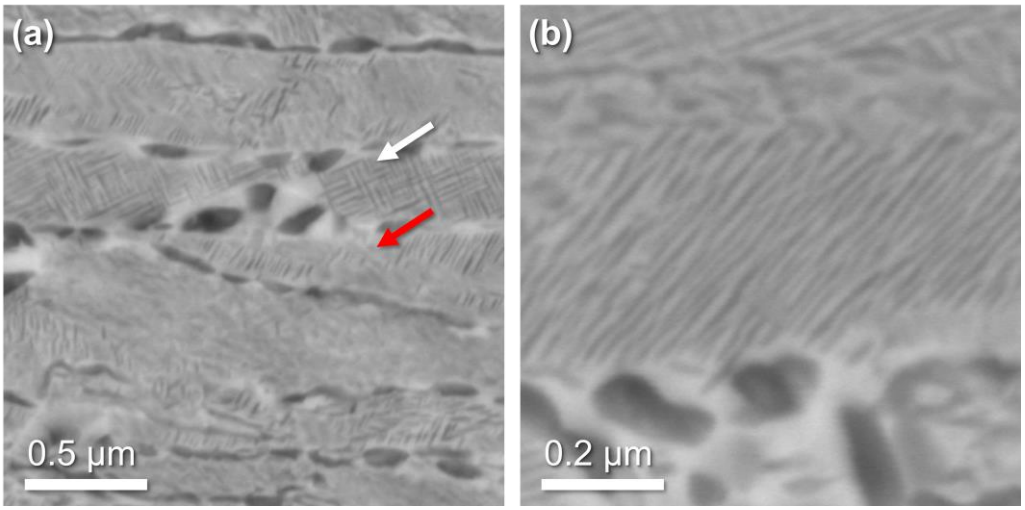

Fig. 6.7. SEM micrograph of 550HT sample (a) at a lower magnification showing grain boundary precipitates, intersecting acicular precipitates marked by white arrow, and parallel precipitates marked by red arrow. (b) Magnified area of an area with parallel precipitates.

6.2.4. Mechanical strength

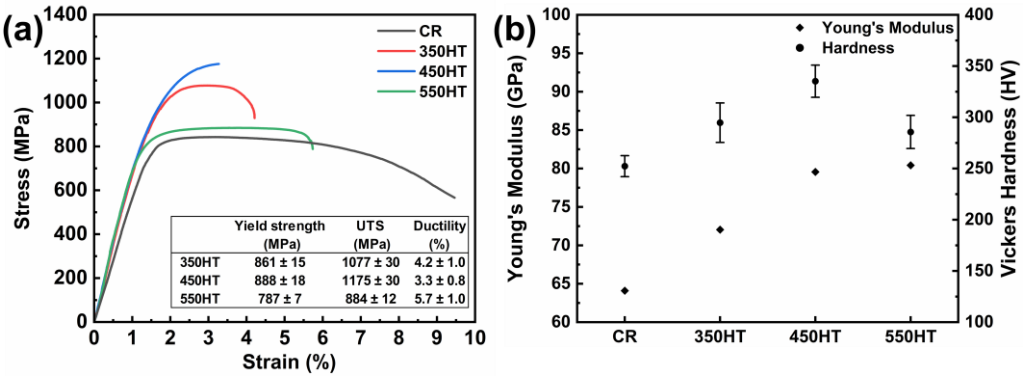

Fig. 6.8. (a) Tensile properties, (b) Young's modulus and Vickers hardness of the thermally cycled samples.

Fig. 6.8a shows the tensile properties of the heat-treated samples along with the reference CR sample. The yield strength of the heat-treated samples was seen to increase from CR to 350HT and subsequently to 450HT, but drastically drops when the cycle temperature was increased to 550 °C.

This trend was repeated inversely for the ductility, where ductility decreased from CR to 350HT while still maintaining a small plastic deformation region. Increasing cycle temperature to 450 °C saw further loss of ductility. The 450HT sample exhibited the lowest ductility among the three heat cycled samples while also being brittle in nature where no plastic deformation region was observed upon

reaching the ultimate tensile strength at the point of fracture. Ductility was then restored in the 550HT sample with a significant plastic deformation region before fracture. In Fig. 6.8b, the Vickers hardness was seen to follow the trend of yield strength, where the sample's hardness increases from 252.29 HV in the CR state to 294.75 and 335.21 for 350HT and 450HT, subsequently dropping to 285.67 for the 550HT state. The Young's modulus of the sample, however, saw a unidirectional increase from 64.1 GPa in the CR state to 72.0, 79.6, 80.4 GPa for the 350HT, 450HT and 550HT respectively.

6.3. Discussion

6.3.1. Phase transformation sequence in a cold-rolled Ti-22Nb alloy

Table 6.1. Table of A_s and A_f temperatures from literature for solution treated, water quenched Ti-Nb alloys around 22 at. %.

Composition (at. %)	A_s (°C)	A_f (°C)	Ref
22	190.39	232.68	[114]
22	187	210	[162]
22	~127	~205	[113]
22.47	~95	~180	[31]
22	134	195	This work

Upon observing the macroscale thermal strain of the CR sample throughout the heating process, it is clear that thermal strain exhibited lacked characteristic martensitic reversion points, A_s and A_f. Characteristic A_s and A_f points for solution treated, water quenched Ti-Nb alloys of similar composition to our study have been presented in Table 6.1. In these works, reverse martensitic transformation was often characterized by a steep contraction by dilatometry and/or an endothermic heat flow through DSC. Origin of the unilateral contraction in the isotropic WQ state stems from the discreet change in atomic volume from α" to β under constant Nb concentration that falls under first-order transformations (Fig. 6.9) [177-179]. The A_s and A_f temperatures measured through dilatometry in our WQ sample fell in line with other reported values. However, sudden contractions corresponding to A_s and A_f points were not observed in the RD and TD thermal strain in the CR

sample (Fig. 6.1). Instead, thermal strain response along both directions showed smooth gradual changes in gradient between 100-190 °C.

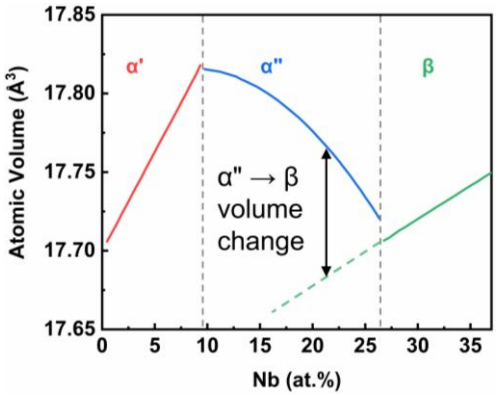

Fig. 6.9. The atomic volume of α/α', α" and β with respect to Nb concentration adopted from [178]

Analysis of the thermal strain through differential means was performed to investigate changes in strain equivalent to the start of reverse martensitic transformation. The second derivative of the macroscale strain response during heating ($\frac{d^2\varepsilon}{dT^2} = \frac{d\alpha_T}{dT}$) representing the rate of change of gradient is presented in Fig. 6.10, where ε is strain and α_T can be interpreted as the instantaneous CTE at any given temperature. A negative dip in $\frac{d\alpha_T}{dT}$ along the RD thermal strain (Fig. 6.10a) at around 110 °C indicates that contraction was accelerated, while a small change in $\frac{d\alpha_T}{dT}$ was observed at 180 °C along TD (Fig. 6.10b). This discrepancy made it difficult to ascertain if sudden rate of change in $\frac{d\alpha_T}{dT}$ along both directions in the CR sample was synonymous to the reverse martensitic transformation. However, the absence of a definitive temperature along RD and TD where a distinct change in strain happens does not equate to the absence of martensitic reversion. The permanent negative strain along RD incurred by the sample after one thermal cycle is associated with reverse martensitic transformation and was measured previously in Section 4.2.4. A small but measurable permanent negative strain was measured even after a cycle temperature of 150 °C, increasing with cycle temperature up to a maximum at 350 °C. Hence, we can ascertain that reverse martensitic transformation certainly occurred in the CR sample but lacks characteristic macroscale volumetric contractions.

The reverse martensitic transformation in CR was assumed to continuously increase up to 320 °C when contraction is at maximum before the thermal strain rebounds and increases with temperature. The orthorhombic unit cell at this stage would usually be described as having the most likeliness to the β unit cell. The shape of the α" unit cell is most commonly described in terms of its likeness to the β unit cell in terms of the edge ratios of the orthorhombic unit cell, $\frac{b_{\alpha"}}{a_{\alpha"}}$ and $\frac{c_{\alpha"}}{a_{\alpha"}}$. At these edge ratio limits, the $(020)_{\alpha"}$ position is seen to be closest to the $(011)_{\beta}$ peak in the diffractogram before merging into a single peak. However, we did not observe that a single β phase was achieved at any temperature and α" peaks were always distinguishable. The exact ratios of $\frac{b_{\alpha"}}{a_{\alpha"}}$ and $\frac{c_{\alpha"}}{a_{\alpha"}}$ were not calculated in our experiments because of insufficient peaks to determine all three lattice parameters of α" due to the widening of peaks from the cold-rolling process. Additionally, another set of considerations was the balancing between scan speed and scan range. While a slower scan speed would provide a more accurate diffraction pattern and a larger 2θ range would provide more discernible peaks, the difference in temperature between the start and end of the scan would be significant, thus affecting the accuracy of d-spacing calculated between the lower and higher 2θ peaks. Ultimately, focus was not placed on the characterization of lattice parameters and comparison of the ratios $\frac{b_{\alpha"}}{a_{\alpha"}}$ and $\frac{c_{\alpha"}}{a_{\alpha"}}$, but rather on the accuracy and peak shift of the $(020)_{\alpha"}$ peak. α" phase was retained within the CR sample for a larger temperature range in our study and the maximum trend of α" lattice parameters was achieved at 320 °C, around 100 °C higher than the reported WQ state. This temperature is higher than any A_f temperature reported in water quenched Ti-Nb alloys of this composition reported in Table 6.1. Although diffusion has been confirmed to occur at temperatures above 150 °C in Chapter 5 resulting in an increase in $(010)_{\alpha"}$ lattice spacing and translating to an increase in sample length along RD over long periods of time, the diffusion rates at these lower temperatures were insignificant in a single cycle heating scenario at the heating rate employed due to the slow diffusion rate of Nb. Discussions related to the reasons behind extended A_f temperature will take place in Section 6.3.2.

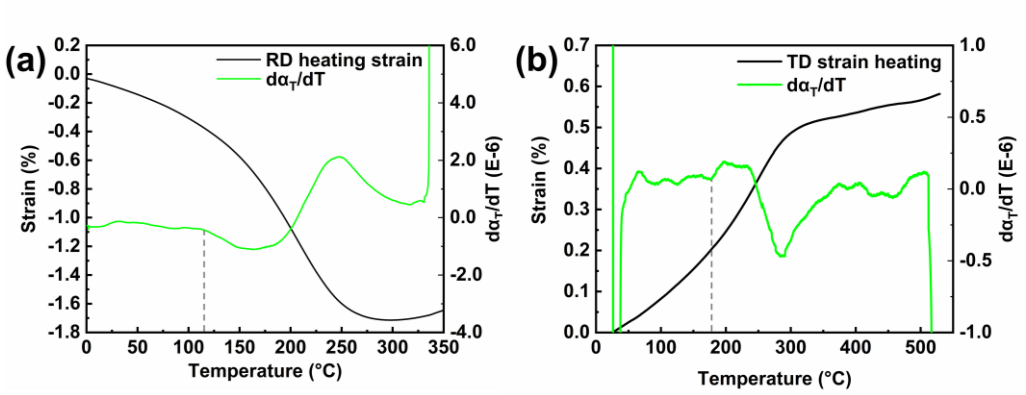

Fig. 6.10. Heating thermal strain and second derivative of the thermal strain up to 350 °C for (a) the RD and (b) TD directions.

The non-linearity of the macroscale thermal strain of the CR sample before reaching maximum contraction at 320 ℃ can be explained by the texture of the sample. Previously through TMA, SEM, and XRD results, the mean orientation along RD, ND and TD of the fully martensitic CR sample were revealed as: RD ∥ $\langle 010 \rangle_{\alpha''}$, ND ∥ $\langle 100 \rangle_{\alpha''}$ and TD ∥ $\langle 001 \rangle_{\alpha''}$ according to the lattice thermal expansion of the orthorhombic α" phase along the three principal directions of the CR sample [1-3, 94]. When comparing the macroscale strain of a CR sample along RD with the measured lattice thermal strain of $(020)_{\alpha''}$ from 0-300 °C (Fig. 6.11), both strain responses exhibit an increasingly negative gradient with heating and experiences a rapid positive increase in gradient before approaching zero gradient at 320 °C. Hence, it can be deduced that the striking similarity of the dynamic macroscale thermal strain response measured along RD was largely contributed by the trend of $(020)_{\alpha''}$ lattice thermal strain directly translated in a macro scale.

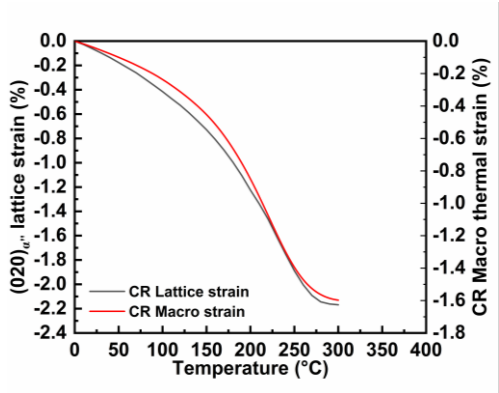

Fig. 6.11. Overlapped comparison showing the similarity between $(020)_{\alpha''}$ lattice strain and thermal strain along RD in CR sample from 0-300 °C.

The precipitation of α"$_{iso}$ from the β+α" mixture occurred with the rebound of thermal strain after reaching maximum negative strain at 320 °C. Rejection of Nb from α" to the surrounding β matrix resulted in the precipitation of α"$_{iso}$ and change of α" composition as reflected by the leftward 2θ shift of the $(020)_{\alpha''}$ peak, leading to an increase in strain along RD. Newly formed precipitates observed through EDX between 300-350 °C (Fig. 6.5) support the diffusional precipitation of α"$_{iso}$ from the β phase, which was formed through reverse martensitic transformation from athermal α" in the CR sample prior to heating. At the same temperature of around 320 °C, a similar increase in volume is observed in the macroscale strain of the WQ sample (Fig. 4.4) indicating that diffusion could also have occurred in the WQ sample at the same temperature. However, the WQ sample is isotropic, hence pointing toward an increase in atomic volume with decreasing Nb concentration. In contrast, the measured thermal strain in CR measures only the $(020)_{\alpha''}$ lattice spacing increase with decreasing Nb concentration.

The rejection of Nb and continuous precipitation of α" continued up to 450 °C in the 450HT sample. Previously observed ellipsoidal precipitates along grain boundaries in the 350HT sample (Fig. 6.5) had grown to resemble a thin layer of precipitate, and in some places had developed into large precipitates that are clearly lean in Nb under STEM mode (Fig. 6.6). Not revealed under dilatometry was the second diffusion that occurred around 450 °C that was clearly visible under in-situ XRD in (Fig. 6.2). An evident deviation of intensity was seen moving leftward from the $(011)_{\beta}$ peak which initially formed a second $(020)_{\alpha''}$ peak, labelled α"$_{rich}$. At this temperature, a weaker intensity could also be seen forming around 41° shifting leftward that ultimately forms $(011)_{\alpha}$. The product of this two-stage diffusion was exemplified in the ex-situ XRD pattern of 450HT (Fig. 6.3b) showing the co-existence of two $(020)_{\alpha''}$ peaks to the left of $(011)_{\beta}$. This ex-situ diffraction pattern was profile fitted and the comprising individual peaks were shown in Fig. 6.12. The two $(020)_{\alpha''}$ peaks were differentiated by their rich and lean Nb content and can be seen in a single diffraction pattern. The position of the Nb lean peaks were calculated using the same method as Fig. 5.15 by using the reported lattice parameters of Ti-Nb and change in lattice parameter per unit concentration by Kim and Miyazaki [42, 60, 61, 120, 136] and matches a Nb concentration of ~14 at.%. Differences in

morphology of Nb-lean and Nb-rich products of this staggered diffusion process can be seen between Fig. 6.5 at 350 °C, and Fig. 6.6a-b at 450 °C. Well-developed intersecting α''_{iso} structures were observed at 350 °C and 450 °C, while parallel structures on the onset of formation were observed only at 450 °C which will subsequently grow into the parallel spinodal decomposition structures at 550 °C (Fig. 6.7b). The staggered progression between the earliest forming α''_{iso} precipitates and the later forming precipitates can be seen as the result of the transformation kinetics at this heating rate combined with the sluggish rate of diffusion of Nb. Discussion of this staggered diffusion is continued in Section 6.3.3.

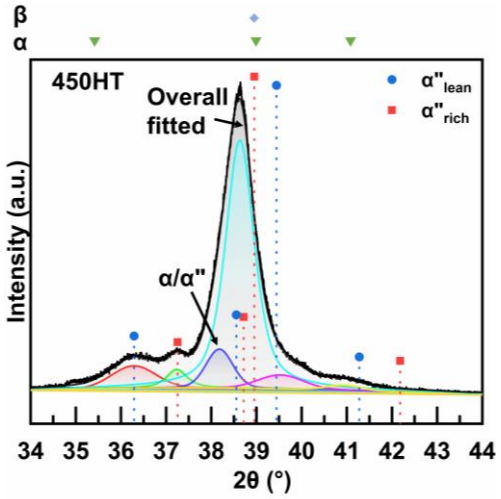

Fig. 6.12. Ex-situ XRD pattern of 450HT sample at RT with profile fitted peaks with calculated α, α" and β peak positions.

The diffusional rejection process of Nb in the lean and rich α" continued in parallel until ~500 °C where a decrease in gradient of macroscale strain is observed along RD and TD in the CR sample (Fig. 6.1). This volumetric shrinking was also seen manifesting in the isotropic WQ sample (Fig. 4.4) around 500 °C. At this point, the earliest forming α''_{iso} reaches the lower limit of Nb concentration at around 7.5% where the atomic volume is largest, and any further loss of Nb causes the atomic volume to decrease (Fig. 6.9). However, in the anisotropic CR sample, this decrease in macroscale strain does not directly relate to a decrease in atomic volume as it was previously established that the RD directly measures the $\langle 020 \rangle_{\alpha''}$ strain. Thus, strain measured macroscopically along RD should reflect the change in lattice direction along $\langle 020 \rangle_{\alpha''}$, assuming that Burgers orientation relationship is wholly

preserved. In in-situ heating studies of martensitic β-Ti alloys detailing the trend of α" lattice parameters undergoing martensitic decomposition, the lattice parameter $b_{\alpha''}$ of the α" phase increases to a maximum at the end of the martensitic decomposition process, and upon transformation to α at the end of the Nb rejection process, the lattice parameter $a_\alpha\sqrt{3}$ decreases before exhibiting regular PTE again. This follows the relationship: $b_{\alpha''} = a_\alpha\sqrt{3}$, as the principal direction a_α exhibits regular PTE [109, 110]. Thus, it could be reasoned that the decreasing parameter $a_\alpha\sqrt{3}$ on the onset of completing martensitic decomposition is due to the continuous rejection of Nb. This is coherent with studies on the α/α' phase that show that the lattice parameter a of the hexagonal α structure decreases with Nb content. Hence, it could be deduced that the decrease in macroscale strain from 500-550 °C was due to the continuous rejection of Nb at the onset of transformation from α" → α. This decrease in $a\sqrt{3}$ after reaching a maximum was not detected in our in-situ XRD scans from 500-550 °C, where two $(020)_\alpha$ peaks were on the onset of formation as seen in Fig. 6.13.

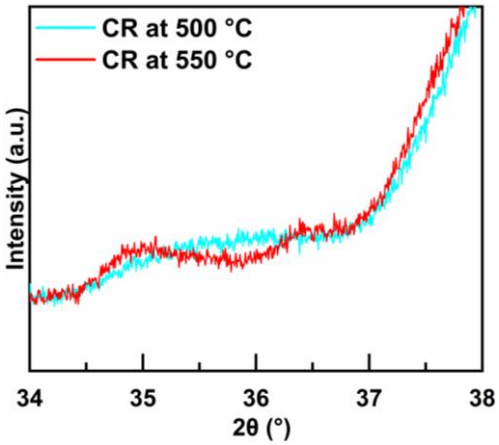

Fig. 6.13. In-situ XRD showing the onset of formation of dual α peaks between 500-550 °C.

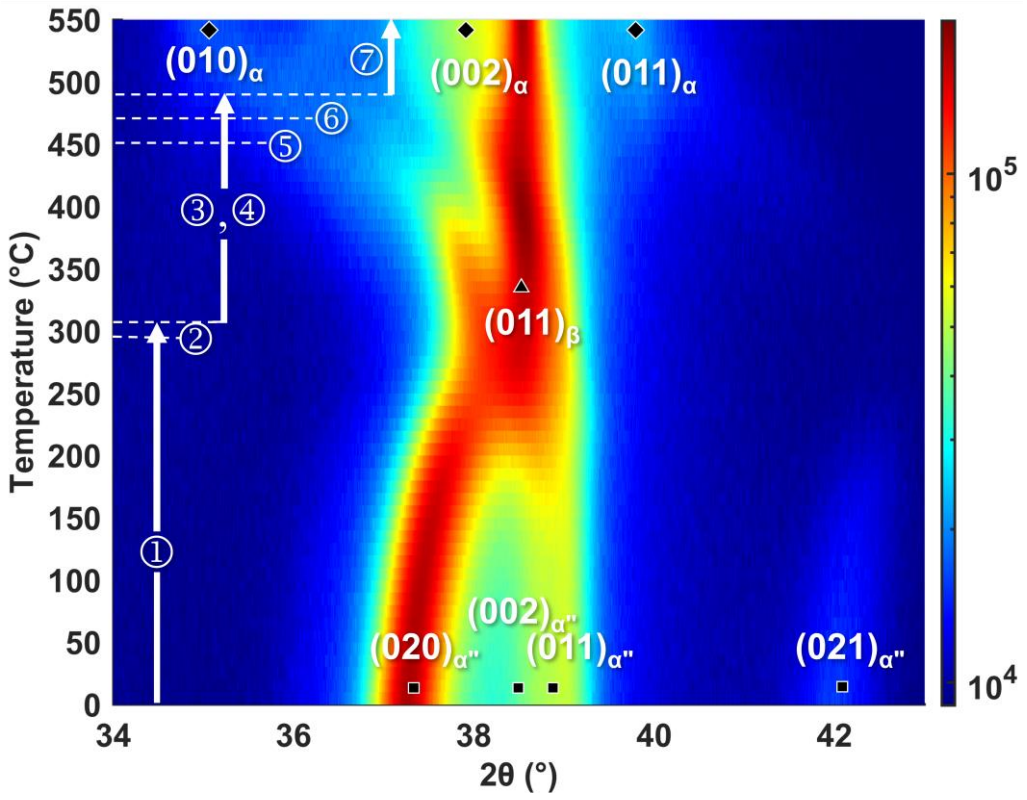

Fig. 6.14. In-situ XRD of the heating of CR sample from 0-550 °C, overlayed with sequence of phase transformations from Table 6.2.

Cooling of the sample from the respective maximum cycle temperatures of 350 °C, 450 °C and 550 °C presented a peculiar macroscale strain response. The initial sections of cooling from the maximum temperatures suggests that the diffusional process persists for a short period before exhibiting a pure thermal expansion response. In materials with regular thermal expansion, the thermal strain response upon cooling follows the path of heating assuming that no phase change to the material had occurred. Alternatively, excluding minor differences as a possibility of thermal hysteresis, major differences in heating and cooling thermal strain could arise from a change in phase constitution or composition. The cooling paths of the CR samples exhibited not only a change in magnitude of gradient from negative to zero in the 350 °C cycle, but even a change in sign of gradient in both the 450 °C cycle and most noticeably in the 550 °C cycle. Fig. 6.15 illustrates of the effects of diffusion during cooling on the path of thermal strain. If diffusion was not present during cooling, the cooling thermal strain would have followed the initial gradient upon cooling (shown as the green dotted line) with a lesser NTE gradient than initially exhibited by the CR sample due to diffusion that

had occurred during heating. Owing to continuous diffusion, the initial NTE gradient at the beginning of cooling was continually diminished until the driving force for diffusion was insufficient and diffusion was stopped. Coincidentally for the 350HT state, ZTE was achieved by achieving an opportune balance of temperature and time dwelled in the diffusion activated region. The effects of continuous precipitation during cooling can be seen in the comparison of the CR sample at high temperature and after the sample has been cooled (Fig. 6.3). The room temperature scans of 350HT and 450HT showed increased intensity of the α" peaks and lowered intensity of β compared to the high temperature scans. In the 550 °C cycle, a small increase in intensity was seen for the two $(011)_{\alpha}$ peaks and the same reduced intensity of β was observed.

The difference in nature of the segregated pair of Nb lean and rich peaks between the 450HT and 550HT conditions can be evidenced through the individual peak shifts. The two Nb lean and rich $(020)_{\alpha''}$ peaks in 450HT exhibited weak negative average CTE of -0.36 ppm/°C and -4.31 ppm/°C respectively between 0-100 °C. The pair of peaks in the 550HT sample displayed a shift of behaviour in the pair of peaks to exhibiting a weak positive average CTE of 5.23 ppm/°C and 1.42 ppm/°C respectively between 0-100 °C (Fig. 6.3d-e), indicating that these are now indeed Nb lean and rich $(010)_{\alpha}$ peaks and no longer NTE exhibiting α" peaks. Hence, the macroscale PTE exhibited by the 450HT sample was comprised of minor fractions of α" exhibiting weak NTE and a larger composition of β, resulting in a reduced PTE behaviour. Meanwhile, the 550HT exhibited a typical α+β thermal expansion behaviour. Although Nb lean zones in large grain boundary precipitates were clearly discerned under STEM for the 450HT (Fig. 6.6b-d), the existence of Nb lean precipitates with two different Nb concentrations could not be discerned under microscopy images in the 450HT and 550HT samples due to TEM limitations.

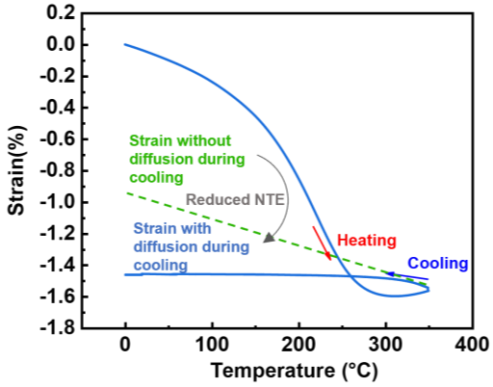

Fig. 6.15. Thermal strain along RD of a CR Ti-22Nb heated to 350 °C with the dotted line depicting the thermal strain during cooling without diffusion.

It is worthy to note that during the heating strain response of the isotropic WQ sample (Fig. 4.4), a volumetric contraction was observed around 250-290 °C. In contrast, this contraction was not seen in the RD and TD thermal strain in the CR sample. DSC experiments [31] have shown that this volumetric contraction is usually accompanied with an endothermic heat flow at around 300 °C for an alloy of this composition [31] evidencing the formation of ω_{iso} from β. TEM was not performed on the 350HT sample to confirm the existence of ω_{iso} but tensile tests on the 350HT showed greatly reduced ductility, supporting the precipitation of ω at this temperature. At a higher temperature of 450 °C, two morphologically distinct ω precipitates were imaged under TEM (Fig. 6.6e-f). The athermally formed ω_{ath} initially in the CR sample had grown to be larger coarser ellipsoidal precipitates while the isothermally formed ω_{iso} at higher temperatures were identified to be the globular precipitates. From the Ti-Nb phase diagram proposed by Zhang et al. [39], the temperature $T^{\beta/\omega}$ at which ω_{iso} was proposed to form from β in Ti-Nb of our composition was roughly around 300 °C. While in a more recently proposed phase diagram by Bönisch [40], this temperature lied more around 130 °C. The tensile tests of the 350HT sample and microstructural observations of ω_{iso} in the 450HT sample suggested that agreeance would lie with the phase diagram proposed by Zhang. This establishes that the influence of both the formation of β and ω_{iso} was not detectable in the RD and TD thermal strain. However, results presented in Chapter 5.3 evidencing the growth and precipitation of ω_{iso} at 150 °C and 250 °C ascertains that ω_{iso} can precipitate at temperatures lower than 300 °C. The discrepancies in these two proposed phase diagrams could lie in the data used to construct these phase diagrams, which

favour different temperature ranges. The phase diagram by Zhang et al. was constructed by optimizing high temperature (>800 K) phase diagram, while the phase diagram by Bönisch used the TiGen database from Yan et al. [76] which focuses on accuracy at lower temperatures. From here, we can summarize the transformation pathways of a CR Ti-22Nb alloy at a heating rate of 3 °C per minute in Table 6.2. The sequence of phase transformations is additionally overlaid in Fig. 6.14 on the in-situ heating XRD performed on the CR sample.

Table 6.2. Phase transformation sequence and occuring temperatures during heating in a CR Ti-22Nb sample.

Sequence	Temperature (°C)	Process
①	100 - 320	$\alpha'' \rightarrow \beta$
②	~300	$\beta \rightarrow \omega_{iso}$
③	320	$\beta \rightarrow \alpha''_{iso}$ (First forming)
④	320 - 490	(First forming) $\alpha''_{iso} \rightarrow \alpha''_{lean}$
⑤	450	$\beta \rightarrow \alpha''_{rich}$ (Later forming)
⑥	~485	$\omega_{iso} + \omega_{ath} \rightarrow \beta$
⑦	490 - 550	$\alpha''_{lean} + \alpha''_{rich} \rightarrow \alpha_{lean} + \alpha_{rich}$

6.3.2. Increased reverse martensitic transformation temperature range

The upper temperature limit of reverse martensitic transformation observed in the CR sample was discussed to be at around 320 °C while the reported A_f temperatures for a Ti-Nb alloy of this composition was around 180-232 °C. The reason for this extended A_f temperature could be due to the tensile stress imposed on the sample from the cold rolling process. The martensitic transformation strain required for $\beta \rightarrow \alpha''$ are described by the principal lattice strains [60, 178] in the orthorhombic reference frame as:

$$\lambda_1 = \frac{a_M^{ort} - a_A}{a_A} \tag{6.1}$$

$$\lambda_2 = \frac{c_M^{ort} - a_A}{a_A} \tag{6.2}$$

$$\lambda_3 = \frac{b_M^{ort} - a_A}{a_A} \tag{6.3}$$

Where the subscript *M* and *A* refer to martensite and austenite, and the subscripts *1*, *2*, *3* refer to principal *x*, *y*, *z* directions along the cubic unit cell. In developing the micromechanical theory for martensitic and reverse martensitic transformations for shape memory alloys, Lu and Weng [180] described the stress required for the forward martensitic transformation and the reverse martensitic transformations as equal in magnitude, hence Equations (6.1-(6.3 can be interpreted with the opposite sign for reverse martensitic transformation of α" → β. Subsequently, the martensitic transformation strain for Ti-Nb alloys was calculated to be largest in magnitude along the $[011]_\beta$ direction by Kim et al. [60], parallel to NTE direction of $[010]_{\alpha''}$. Thus, again applying the understanding from Lu and Weng [180], it is assumed that the contractional transformational strain is largest along RD and is subsequently opposed by the tensile stress induced by cold rolling acting along the same direction. This results in a wider temperature range where larger thermal strains are required to overcome the transformation strain needed for the martensite to austenite transformation.

From the appearance of the XRD pattern, the broadening of XRD peaks can be related to size of crystallites (also known as the size effect) or the inter/intragranular inhomogeneous strain where the lattice spacings of grains are affected [138] (known as the strain effect). This results in an expanded 2θ range where a range of lattice spacings satisfy Bragg's law for diffraction. Scherrer's equation (Equation (6.5) is widely used to estimate the size of crystallites from the obtained peak profile in XRD. The parameter factor θ_B is the angular distance of the FWHM. $B_{1/2}$ is the FWHM of the peak which can be dictated by other factors such as instrumental broadening and size effect. The effect of broadening due to crystallite size is only significant when the size effect broadening is more

significant than the instrumental broadening. Depending on the instrument, commonly recommended particle size limits are 0.5-1 microns where size effect broadening is significant. [138]

$$t = \frac{0.9\lambda}{B_{1/2}\cos\theta_B} \tag{6.4}$$

Characterization of the microstrain existing in the CR sample was attempted using the full-width-half-maximum (FWHM) of the profile fitted peaks from the XRD scan. Fig. 6.16a shows a diffractogram of the CR sample taken using a Mo target along ND to maximize the number of peaks reflected. The captured diffractogram was profile fitted over a wide angle. Blue vertical lines at the bottom of each section of the diffractogram indicates calculated α" peak positions of Ti-Nb. Areas b, c and d were enclosed and magnified in Fig. 6.16b-d for clarity. The FWHM of the profile fitted peaks displayed below the diffractogram in Fig. 6.16a showed an erratic and wide spread of FWHM values for the fitted peaks, indicating that a good fit required to describe the trend of FWHM was not achieved. Below the FWHM diagram of Fig. 6.16a is a Williamson-Hall plot that uses the calculated FWHM to estimate the broadening contributed by crystallite size and strain. A quadratic variant of the Williamson-Hall plot was selected with the assumption that broadening was largely contributed by strain and not the size effect. The gradient of the curve represents the micro strain, while the intercept determines the crystallite size. Again, the wide spread of FWHM resulted in a very unagreeable Chi square result, where a good fit is below ~0.1. This wide spread of FWHM resulted in a high uncertainty in the gradient and intercept calculated, as seen in the box in the bottom left indicating a 1% strain with a 1% uncertainty. Despite having good fit over a wide range, heavy broadening and peak overlapping resulted in the FWHM of overlapped peaks to be uncertain and unfit to be used in the Williamson-Hall plot. Alas, while the position of the $(020)_{\alpha''}$ could be confidently calculated due to its solitariness, the FWHM of the rest of the detectable peaks were unreliable and the estimation of microstrain within the sample was unable to be estimated to an acceptable degree.

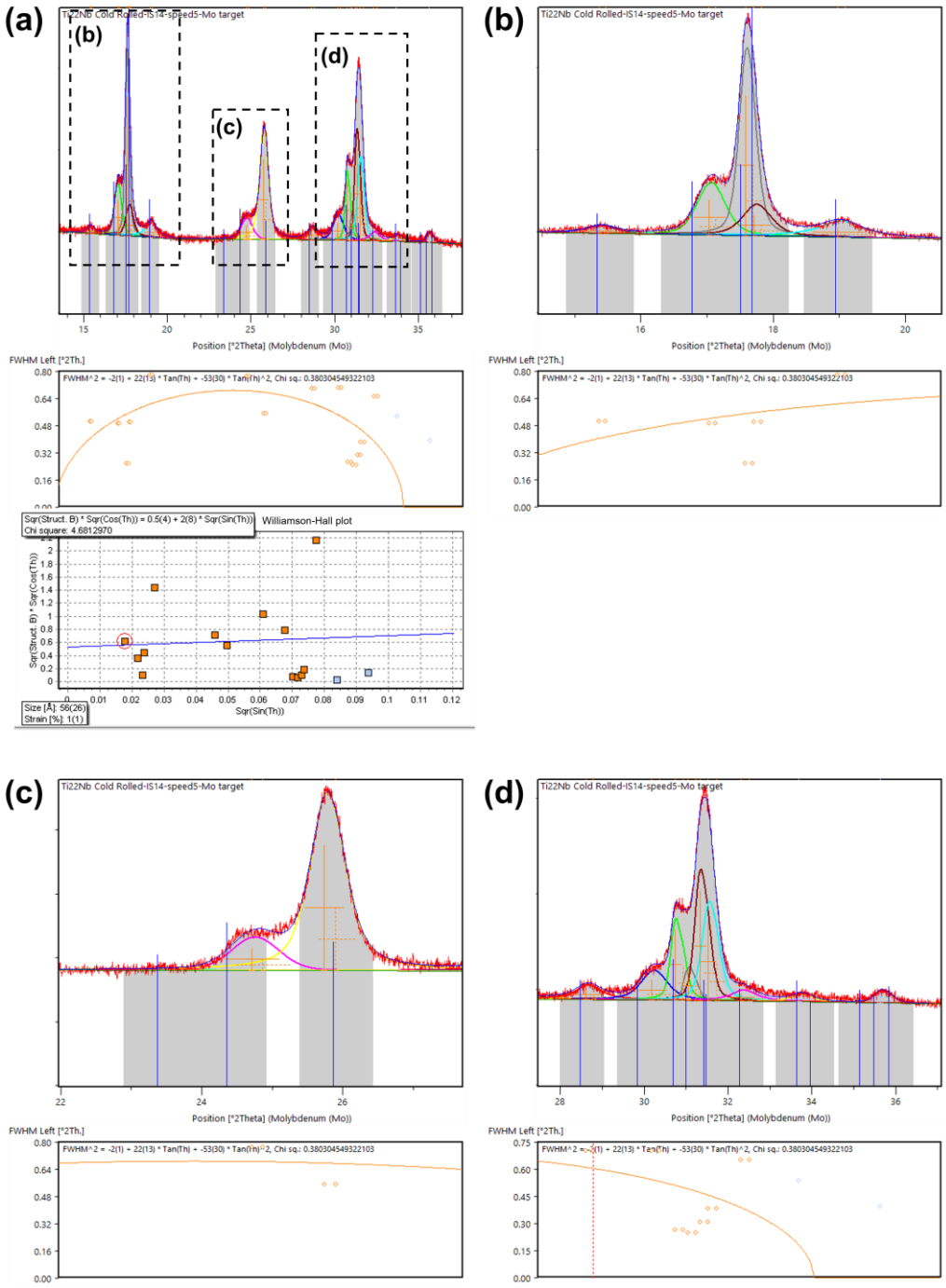

Fig. 6.16. (a) Wide angle ex-situ XRD pattern of a CR Ti-22Nb with individual profile fitted peaks. The middle figure below shows the trend line of the profile fitted FWHM of every individual peak. The bottom figure shows the Williamson-Hall plot in an attempt to calculate the residual stress within the sample. (b), (c), (d) shows the magnified areas in (a) with their calculated FWHM attached below.

6.3.3. Staggered diffusional process

The question remains on what led to the staggered temperature between the diffusion occurring first at ~320 °C and the staggered diffusion at ~450 °C. A key difference between these two diffusion stages

was that the first diffusion was undergone by α" that was initially present in the CR sample, while the second diffusion originated from the major β peak at ~450 °C. Temperature dependent diffusion in metals can be, in simple cases, described by the Arrhenius formula (Equation (6.5) by Pontau and Lazarus [181] and Mehrer [182]. Where D is the diffusion coefficient, D_0 is the frequency factor (also called pre-exponential factor) and ΔH is the activation enthalpy for diffusion, T is the absolute temperature and R is the gas constant.

$$D = D_0 \exp(-\frac{\Delta H}{RT}) \tag{6.5}$$

The activation enthalpy can then be described as:

$$\Delta H = -R\frac{\partial D}{\partial(1/T)} \tag{6.6}$$

D_0 and in (Equation (6.5) can be expanded to give:

$$D = f a^2 v_0 \exp\left[\frac{\Delta s_f + \Delta s_m}{R}\right] \exp[\frac{-\Delta H_f + \Delta H}{RT}] \tag{6.7}$$

The Gibbs free energy ($\Delta G = \Delta H - T\Delta s$) has been split into the entropy s and enthalpy H for the formation and migration contributions denoted by the f and m subscripts, the non-subscript f is the correlation factor that determines the random diffusion jumps, v_0 is the Debeye frequency. The diffusion coefficient in Ti-Nb alloys have been described as anomalous, which results in the plot of $\ln D$ vs $1/T$ to be non-linear and Equation (6.7 has to be represented with two separate coefficients of diffusion. However, that is only relevant in high temperatures in the pure β region and in low temperatures, the linear form still holds true. The term $\exp(-\frac{\Delta G_f}{RT})$ was described to be the relative concentration of defects, hence describing the important of defects in diffusion. However, parameter a^2 is the lattice parameter, which highlights that the difference in unit cell shape between α" and β could make a difference in the enthalpy required for diffusion.

The discussion earlier on the inhomogeneous tensile stress being the possible cause of the extension of the A_f temperature could also be interpreted as widening the range of free enthalpy (thus temperature) required to trigger diffusion. Effects of cold rolling on the temperature range of

transformations have been studied in a wide range of alloys through calorimetry. It is widely accepted that cold rolling can largely affect the temperature range of transformations of alloys. These transformation temperatures can shift or widen significantly depending on the alloy [183-185]. It is also noteworthy that Equation (6.5 only describes diffusion in simple cases, like self-diffusion within an element of metal. Cases where conditions like high angle grain boundaries exist can affect the diffusion activation energy. The mode of diffusion can depend on the movement of atoms around dislocations or grain boundaries. The size of the atoms involved along with defects and vacancies available in the alloy largely determine the diffusion mechanism and diffusion rate [182]. The creation of significantly more grain boundaries through cold rolling induced deformation is also a factor that could affect diffusion [186-188]. However, a comprehensive study on the possibility of the effects of cold rolling on the diffusion behaviour of the alloy is tricky and was not the main focus of this study.

6.3.4. Mechanical properties of heat-treated Ti-22Nb

The continuous precipitation strengthening through formation of ω_{iso} can be attributed to the increase in yield stress and Vickers hardness from CR to 350HT and 450HT. Progressively dense formation of ω_{iso} is made apparent in the impeded ductility of the 350HT sample, which progressively led to the brittle nature of the 450HT as seen in many similar β-Ti alloys [189-193]. The formation of ω_{iso} precipitates changes the plastic deformation of β-Ti alloys from ductile to a brittle nature due to progressive element partitioning which gives rise to self-hardening and transitioning of deformation mode from twinning to dislocation slip [190]. It can then be inferred that the restored ductility in the 550HT sample can be attributed to the loss of ω_{iso}, although it was observed that restored ductility is still less than the CR state. This is certainly the case when referencing the phase diagram from Zhang [39], where the predicted maximum temperature of stability for ω_{iso} was around 485 °C. Heating the CR sample above this temperature sees not only the ductility of the 550HT restored but also the lowering of yield strength and Young's modulus. It has been reported that isothermally formed ω particles play a role in the assisted precipitation of α particles by acting as nucleation sites. It is argued that the stress field induced by the complete collapse of the $<1\bar{1}1>_{\beta}$ from the formation of ω_{iso} provides nucleation sites for α. α matrices formed within β grains are known to contribute to the

strength of precipitation strengthened Ti alloys while grain boundary α (α_{GB}) are known to be deleterious for the alloy's ductility. Cracks have been reported to go through α_{GB} instead of through the grains with minimal resistance hence resulting in lower ductility compared to the CR state [160].

6.3.5. Performance of heat treated cold-rolled Ti-22Nb as a low thermal expansion material

The performance of the heat-treated Ti-22Nb alloys can be collectively evaluated by the mechanical property, represented by its Young's modulus, and its thermal expansion as shown in Fig. 6.17a. In the same figure, several common classes of alloys were presented alongside the reference and heat-treated Ti-22Nb alloys as reproduced from Ashby [163]. The heat-treated Ti-22Nb alloys can be seen as some of the lowest thermally expanding alloys. The stiffness, however, of all three heat-treated conditions lack in comparison to another common class of low thermal expansion alloy, Invar, or Fe-Ni alloys [124] even when considering the improvement in Young's modulus of 450HT and 550HT via the precipitation of ω_{iso}. One of the key strengths of Ti alloys lie in its light weight, hence, the specific modulus of the alloy, defined by $\frac{E}{\rho}$, where E is Young's modulus and ρ is density, was considered in Fig. 6.17b. Since density varies for every alloy depending on the type and amount of alloying element, an average density of commonly seen commercial alloys reported in [164] belonging to the same class was used to calculate the specific modulus from Fig. 6.17a. For our study, an experimentally obtained density value of 5890 (±100) kg/m^3 for Ti-22Nb was used to calculate the specific modulus. We see that Ti alloys provide exceptional strength to weight ratio while providing tailorable negative and low thermal expansion capabilities. This positions Ti alloys as a prime candidate for low thermal expansion applications where lightweight is prioritized over high stiffness.

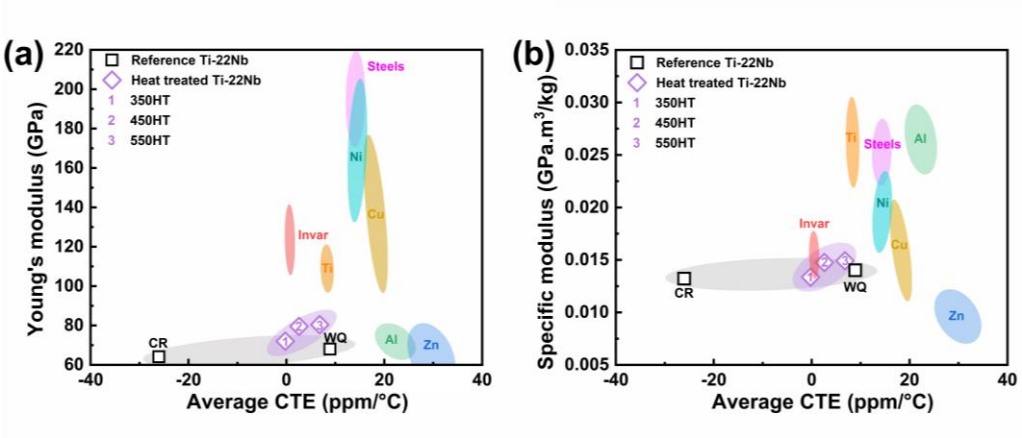

Fig. 6.17. (a) The Young's modulus and average CTE of WQ, CR and heat-treated Ti-22Nb samples in comparison to other commonly used commercial alloys adapted from [163]. (b) The specific modulus was calculated by using the average densities of commercial alloys from [164].

One of the highlights of the HT Ti-22Nb is the temperature range of stable linear thermal expansion. While the CR sample exhibited a strong non-linear thermal response within the NTE region below 320 °C, heat treatment linearized the thermal strain responses of the HT samples between 0-300 °C. The average CTEs measured in the eight heating-cooling thermal stability cycles proved that the obtained CTEs were relatively stable. The strain value fluctuations measured at 0 °C between every cycle indicated that there could be micro compositional fluctuations occurring in at temperatures near 300 °C, while the 450HT was stable between this temperature range. The linearization of the thermal strain comes from the stabilization of the constitution of phases within the alloy. Part of the alloy had undergone martensitic reversion and resulted in the stable austenitic β phase, while the rest of the alloy consists of Nb lean α" that underwent Nb rejection or precipitation, leading to decreased β stability and higher A_s temperatures. Of these two, the latter provided an anisotropic NTE phase of extended thermal stability, while the former provided a thermally stable PTE counterpart, both as a result of heat treatment. The long-term stability of these heat-treated samples in the span of 10, 100 or 1000 hours, however, have yet to be determined. This improvement in thermal stability elevates Ti-Nb alloys as an alternative low thermal expansion alloy to Invar, or Fe-Ni based alloys which are known to be the lowest thermal expansion alloys below 230 °C. However, for the binary composition that exhibits the lowest thermal expansion (Fe-36Ni), the non-linearity of its thermal expansion starts around 162 °C [164]. Both Fe-Ni and Ti-Nb alloys have tuneable CTEs through cold work, but while

the range of CTE achievable through cold work for Fe-Ni is rather narrow (0.3-1.4 ppm/°C) [164], the change in CTE that can be achieved by Ti-Nb alloys is available in a much wider range as demonstrated by Monroe [1] and our work in Chapter 4. One key difference between Fe-Ni and Ti-Nb, however, lies in isometric volume expansion of Fe-Ni versus the anisotropic thermal expansion of Ti-Nb. NTE in Ti-Nb is focused along the $\langle 010 \rangle_{\alpha''}$ (RD in this study), while $\langle 100 \rangle_{\alpha''}$ (ND) and $\langle 001 \rangle_{\alpha''}$ (TD) both exhibit PTE, as seen in Chapter 4. In fact, the $\langle 100 \rangle_{\alpha''}$ exhibits extremely large PTE that contributes to the overall volumetric PTE [2]. Hence, consideration must be taken to account for the anisotropic massive PTE during the use of near β martensitic Ti alloys for their unique thermal expansion property.

6.4. Summary

In this chapter, the mechanisms behind the evolution of NTE and mechanical properties in an anisotropic thermally expanding CR Ti-22Nb alloy from 0-550-0 °C were explored. The CR Ti-22Nb sample exhibited increasingly larger NTE along RD below 320 °C that directly correlates to the exhibition of lattice thermal expansion of the $(020)_{\alpha''}$ plane due to texturing effect from cold-rolling. The sample exhibited martensitic reversion across an extended temperature range that was hypothesised to have been due to the cold-rolling process. Diffusional rejection of Nb in martensite occurred rapidly above 320 °C resulting in a change from NTE to PTE of the $(020)_{\alpha''}$ plane, translating to a PTE macro strain behaviour along RD. Cooling down from 350 °C resulted in a composition of Nb lean α" and β which exhibited ZTE sample along RD. A staggered diffusion process which occurred at ~450 °C resulted in a secondary diffusion process of $\beta \rightarrow \alpha''_{rich}$, resulting in two compositionally different α" existing in a single sample. Cooling down from 450 °C resulted in further Nb depleted martensite and higher volume fraction of β, resulting in low PTE along RD. Further heating to 550 °C resulted in α+β alloy that exhibited a typical PTE. Long dwell time under favourable temperatures for ω_{iso} formation strengthened the alloy when thermally cycled to 350, 450 °C and cooled but at the expense of ductility. Heating to 550 °C resulted in the dissolution of ω_{iso}, restoration of ductility while retaining improvement in Young's modulus.

7. Conclusions and outlook

The goal of this work was to investigate and understand facets relating to the stability and performance of anisotropic NTE and the resulting mechanical properties in a CR Ti-22Nb. The main conclusions and possible outlooks for future studies based on the current findings are discussed.

7.1. Conclusions

- NTE behaviour of CR Ti-22Nb thermally cycled to temperatures well above the A_s temperature was previously unknown and has been characterized in this study. This finding allows for the prediction of thermal expansion behaviour from the fully martensitic state to the stable dual-phase state. NTE was retained in CR samples cycled to maximum cycle temperatures of 150, 250 °C. CR samples heated to maximum cycle temperatures of 350, 450, 550 °C displayed gradual loss of NTE to achieve ZTE, low PTE and conventional PTE respectively. The mechanisms behind the change in thermal expansion behaviour and the resulting mechanical properties were studied in this temperature range.
- Isothermal aging of CR Ti-22Nb at 150 °C and 250 °C showed increasing loss of NTE over the span of 10, 100, 1000 hours. The loss of NTE at both aging conditions was attributed to the diffusional rejection of Nb from α" to the surrounding β matrix. Additionally, isothermal precipitation of α" was observed in the 250 °C aged sample, but not in the 150 °C aged state. The decrease in NTE was measured after aging at 150 °C for 1000 hours, at only 23%. Comparatively, a drastic 98.8% loss in NTE was observed when the CR sample was aged at 250 °C for 1000 hours, allowing the sample to achieve ZTE. Long term thermal stability is a crucial property to uncover especially for a material that is to be employed for its thermal property. This allows for the prediction of changes to the alloy during its service life and enables timely maintenance and replacement before catastrophic failure occurs.
- A peculiar trend in ductility was observed in the 150 °C aged samples with increasing aging time. An initial substantial decrease in ductility was measured at 10h aging, followed by a substantial increase of ductility at 100h, and finally a decrease in ductility again at 1000h.

TEM and HRTEM revealed the dissolution of the initial athermal ω and the gradual development of isothermally precipitated nanoscale incommensurate ω to commensurate ω over the span of 1000 hours. Aging at 250 °C saw a continuous increase in elastic moduli but ductility decreased unidirectionally towards a brittle state owing to the growth of ω into large precipitates. This destruction-precipitation of ω has not been documented due to the long time commitment and difficult characterization of incommensurate precipitates. This finding strengthens our understanding of the Ti-Nb system.

- The phase transformations and mechanisms behind the change in CTE during the thermal cycling of a CR Ti-22Nb was characterized through dilatometry and in-situ XRD. It was shown that the macro thermal strain measured along RD was largely due to the direct translation of $(020)_{\alpha''}$ lattice thermal expansion into a macro scale. Rapid diffusional rejection of Nb occurred around 320 °C, resulting in rapid expansion along $\langle 020 \rangle_{\alpha''}$ and the RD. Cooling from 350 °C resulted in a delicate balance of phase constitution consisting just right amounts of α" and β to achieved ZTE in along RD. Heating to a higher maximum cycle temperature of 450 °C resulted in a staggered diffusion process that saw Nb lean and Nb rich α" XRD peaks coexist within the same sample. The outcome was an alloy that exhibited low PTE along RD. Further heating to 550 °C resulted in a conventional α+β alloy.
- Cold-rolling in the alloy was rationalized to have two effects on the cold-rolled Ti-22Nb alloy. Firstly, the martensitic reversion temperature range was extended due to the tensile stress acting against the direction of largest transformation strain. Secondly, the abnormal staggered diffusion process could have been due to cold-rolling affecting diffusion modes and free enthalpy for diffusion to occur.

7.2. Outlook

This work serves to pave the way towards manipulating the NTE of CR Ti-Nb through heat treatment and furthering our understanding of the metallurgy and phase transformations of Ti-Nb alloys. The large anisotropic NTE of Ti-Nb alloys combined with its lightweight proved to be an easily manipulable, lightweight material candidate to serve as counter strain solutions where dimension

control and light weight is key. Applications such as wearable technology, vehicles or telescopes could be fields where this attribute can be employed. However, gaps in our current understanding of influencing factors behind NTE of Ti-Nb alloys hinder the progress in manufacturing, application, or understanding the limits of the alloy. Below are the aspects that could be explored:

- **The effect of cold-working on the phase transformation of Ti-Nb.** It has been proven that the exhibition of anisotropic thermal expansion is highly dependent on the phase composition and preferred orientation of the material. Inducing texture via deformation reorientation is one of the most commonly used methods. The effect of deformation reorientation on the free enthalpy landscape [39, 40] could be clarified in terms of the interaction between the stresses involved with the transformation strains required [60] and verified through experimental means. This could also verify hypotheses regarding the effect of cold work on the transformation sequence mentioned in Section 6.3, especially the odd staggered diffusion process.
- **Understanding the time and diffusion rate dependency of products in the metastable Ti-Nb system.** Even with an accurate enthalpy landscape of the Ti-Nb system, the products of diffusion of the metastable phase are closely related to diffusion rate and time. As demonstrated, a CR Ti-Nb sample can be thermally processed to exhibit ZTE through isothermal aging at 250 °C for 1000 hours, or through thermal cycling to 350 °C at 3 °C/min. While low temperature aging can be less time sensitive and allow for more control over the final CTE obtained, thermal cycling to higher temperatures exhausts less time and energy. Previous studies on diffusion rate in Ti-Nb systems [42, 181, 194] only use (α+β) Ti alloys and does not include martensitic phases. Since diffusion rate could differ in martensite due to the enthalpy of martensite and the dependence on lattice parameters as described in Equation 6.4, values of diffusion coefficient for martensite should be reconsidered. Thorough study of the diffusion rate and time dependencies could help in optimizing the time and temperature required to achieve a desired final product CTE.

- **Exploration of ZTE in an additively manufactured Ti-Nb.** Li [80] and Bönisch [40] have shown that a ZTE plane in the unit cell reference frame exists. Through this work, we have demonstrated that the macroscale CTE measured in a highly textured sample is highly reflective of the lattice CTE. Hence, it could be possible to explore ZTE directions of highly textured Ti-Nb of a wide series of concentration through the use of additive manufacturing.

8. Reference

1. Monroe, J., et al., *Tailored thermal expansion alloys.* 2016. **102**: p. 333-341.
2. Bönisch, M., et al., *Giant thermal expansion and α-precipitation pathways in Ti-alloys.* Nature Communications, 2017. **8**(1): p. 1429 DOI: 10.1038/s41467-017-01578-1.
3. Gehring, D., et al., *In-situ investigation of anisotropic crystalline and bulk negative thermal expansion in titanium alloys.* 2021. **210**: p. 116847.
4. Wang, H., et al., *Nano-precipitation leading to linear zero thermal expansion over a wide temperature range in Ti22Nb.* 2021. **205**: p. 114222.
5. Wu, X., et al., *The mechanism of negative linear thermal expansion behavior of cold-rolled Ti-34Nb alloy.* 2021. **56**(8): p. 5190-5200.
6. Takenaka, K.J.S. and t.o.a. materials, *Negative thermal expansion materials: technological key for control of thermal expansion.* 2012.
7. Barrera, G.D., et al., *Negative thermal expansion.* 2005. **17**(4): p. R217.
8. Lind, C. *Two Decades of Negative Thermal Expansion Research: Where Do We Stand?* Materials, 2012. **5**, 1125-1154 DOI: 10.3390/ma5061125.
9. Miller, W., et al., *Negative thermal expansion: a review.* 2009. **44**(20): p. 5441-5451.
10. Takenaka, K., *Progress of Research in Negative Thermal Expansion Materials: Paradigm Shift in the Control of Thermal Expansion.* 2018. **6** DOI: 10.3389/fchem.2018.00267.
11. Zhao, Y.-Y., et al., *Giant Negative Thermal Expansion in Bonded MnCoGe-Based Compounds with Ni2In-Type Hexagonal Structure.* Journal of the American Chemical Society, 2015. **137**(5): p. 1746-1749 DOI: 10.1021/ja510693a.
12. Welsch, G., R. Boyer, and E. Collings, *Materials properties handbook: titanium alloys*. 1993: ASM international.
13. Banerjee, S. and P. Mukhopadhyay, *Phase transformations: examples from titanium and zirconium alloys*. 2010: Elsevier.
14. Banerjee, D. and J.J.A.M. Williams, *Perspectives on titanium science and technology.* 2013. **61**(3): p. 844-879.
15. Demakov, S., I. Semkina, and A. Yurovskikh. *Parameters Evolution of Orthorhombic Martensite Lattice Ti-Mo-Al Alloys Studied by in Situ T-XRD*. in *IOP Conference Series: Materials Science and Engineering*. 2018. IOP Publishing.
16. Takenaka, K., *Giant Negative Thermal Expansion Materials: Progress of Research and Future Prospects.* MATERIALS TRANSACTIONS, 2024. **65**(3): p. 243-252 DOI: 10.2320/matertrans.MT-Y2023008.
17. Yamai, I. and T. Ota, *Grain Size-Microcracking Relation for NaZr2(PO4)3 Family Ceramics.* Journal of the American Ceramic Society, 1993. **76**(2): p. 487-491 DOI: https://doi.org/10.1111/j.1151-2916.1993.tb03811.x.
18. Ohya, Y., Z.-e. Nakagawa, and K. Hamano, *Grain-Boundary Microcracking Due to Thermal Expansion Anisotropy in Aluminum Titanate Ceramics.* Journal of the American Ceramic Society, 1987. **70**(8): p. C - 184-C - 186 DOI: https://doi.org/10.1111/j.1151-2916.1987.tb05720.x.

19. Kuszyk, J.A. and R.C. Bradt, *Influence of Grain Size on Effects of Thermal Expansion Anisotropy in MgTi2O5.* Journal of the American Ceramic Society, 1973. **56**(8): p. 420-423 DOI: https://doi.org/10.1111/j.1151-2916.1973.tb12714.x.

20. Benavente, R., et al., *Effect of sintering technology in β-eucryptite ceramics: Influence on fatigue life and effect of microcracks.* Materials Science and Engineering: A, 2016. **651**: p. 668-674 DOI: https://doi.org/10.1016/j.msea.2015.11.013.

21. Takenaka, K., et al., *Colossal negative thermal expansion in reduced layered ruthenate.* Nature Communications, 2017. **8**(1): p. 14102 DOI: 10.1038/ncomms14102.

22. Zhou, C., et al., *Fully-dense Mn3Zn0.7Ge0.3N /Al composites with zero thermal expansion behavior around room temperature.* Materialia, 2019. **6**: p. 100289 DOI: https://doi.org/10.1016/j.mtla.2019.100289.

23. Takenaka, K., et al., *Fabrication of Metal Matrix Composite Containing Manganese Nitride Showing Giant Negative Thermal Expansion by Compressive Torsion Processing.* MATERIALS TRANSACTIONS, 2021. **62**(5): p. 590-595 DOI: 10.2320/matertrans.MT-M2020363.

24. Kadowaki, Y., et al., *Structural phase transition and giant negative thermal expansion in pyrophosphate Zn2–xMgxP2O7.* Applied Physics Letters, 2021. **119**(20): p. 201906 DOI: 10.1063/5.0073761.

25. Son, M.-A., et al., *Structural origin of negative thermal expansion of cordierite honeycomb ceramics and crystal phase evolution with sintering temperature.* Journal of the European Ceramic Society, 2019. **39**(7): p. 2484-2492 DOI: https://doi.org/10.1016/j.jeurceramsoc.2019.02.017.

26. Hashimoto, T., et al., *Thermal conductivity of negative-thermal-expansion oxide, Zr1−xYxW2O8 (x=0.00, 0.01)—temperature dependence and effect of structural phase transition.* Solid State Communications, 2004. **131**(3): p. 217-221 DOI: https://doi.org/10.1016/j.ssc.2004.05.001.

27. Gepreel, M.A. *New Ti-alloy with negative and zero thermal expansion coefficients*. in *Key Engineering Materials*. 2012. Trans Tech Publ.

28. Wu, X., et al., *Study on the anomalous thermal expansion behavior of cold-rolled Ti-34 Nb alloy and its novel tailoring strategy.* Materials Today Communications, 2022. **31**: p. 103670 DOI: https://doi.org/10.1016/j.mtcomm.2022.103670.

29. Bönisch, M., *Structural properties, deformation behavior and thermal stability of martensitic Ti-Nb alloys*. 2016.

30. Bönisch, M., et al., *Thermal stability and phase transformations of martensitic Ti–Nb alloys.* 2013.

31. Bönisch, M., et al., *Thermal stability and latent heat of Nb–rich martensitic Ti-Nb alloys.* 2017. **697**: p. 300-309.

32. Jaffee, R.I., *Titanium Metallurgy in the U.S.S.R.: Hydrogen in Titanium. By V. A. Livanov, A. A. Bukhanova, and B. A. Kolachev. Israel Program for Scientific Translations, Jerusalem; Davey, New York, 1965. 208 pp., $10.25.; Phase Diagrams of Titanium Alloys. By E. K. Molchanova. Israel Program for Scientific Translations, Jerusalem; Davey, New York, 1965. 318 pp., $15.25.* Science, 1966. **152**(3726): p. 1233-1234 DOI: 10.1126/science.152.3726.1233.

33. Cotton, J.D., et al., *State of the art in beta titanium alloys for airframe applications.* 2015. **67**(6): p. 1281-1303.

34. Murray, J.L., *The Ti–Zr (Titanium-Zirconium) system.* Bulletin of Alloy Phase Diagrams, 1981. **2**(2): p. 197-201 DOI: 10.1007/BF02881478.

35. Moffat, D.L. and U.R. Kattner, *The stable and metastable Ti-Nb phase diagrams.* Metallurgical Transactions A, 1988. **19**(10): p. 2389-2397 DOI: 10.1007/BF02645466.

36. Murray, J.L., *The Cr−Ti (chromium-titanium) system.* Bulletin of Alloy Phase Diagrams, 1981. **2**(2): p. 174-181 DOI: 10.1007/BF02881474.

37. Murray, J.L., *Calculation of the titanium-aluminum phase diagram.* Metallurgical Transactions A, 1988. **19**(2): p. 243-247 DOI: 10.1007/BF02652532.

38. Okamoto, H., *N-Ti (Nitrogen-Titanium).* Journal of Phase Equilibria and Diffusion, 2013. **34**(2): p. 151-152 DOI: 10.1007/s11669-012-0153-6.

39. Zhang, Y., H. Liu, and Z. Jin, *Thermodynamic assessment of the Nb-Ti system.* Calphad, 2001. **25**(2): p. 305-317 DOI: https://doi.org/10.1016/S0364-5916(01)00051-7.

40. Bönisch, M., M. Stoica, and M. Calin, *Routes to control diffusive pathways and thermal expansion in Ti-alloys.* Scientific Reports, 2020. **10**(1): p. 3045 DOI: 10.1038/s41598-020-60038-x.

41. Ronami, G., et al., *Determination of the phase boundaries in Ti systems with V, Nb, and Mo by the diffusion-layer method.* J. Moscow. Univ. Phys., 1970. **25**: p. 55-57.

42. Moffat, D.L., *Phase transformations in the titanium-niobium binary alloy system*. 1985, The University of Wisconsin-Madison.

43. Kolli, R.P. and A. Devaraj, *A Review of Metastable Beta Titanium Alloys.* Metals, 2018. **8**(7) DOI: 10.3390/met8070506.

44. Hickman, B.S., *The formation of omega phase in titanium and zirconium alloys: A review.* Journal of Materials Science, 1969. **4**(6): p. 554-563 DOI: 10.1007/BF00550217.

45. Ballor, J., et al., *A review of the metastable omega phase in beta titanium alloys: the phase transformation mechanisms and its effect on mechanical properties.* International Materials Reviews, 2023. **68**(1): p. 26-45 DOI: 10.1080/09506608.2022.2036401.

46. Bönisch, M., et al., *Factors influencing the elastic moduli, reversible strains and hysteresis loops in martensitic Ti–Nb alloys.* Materials Science and Engineering: C, 2015. **48**: p. 511-520 DOI: https://doi.org/10.1016/j.msec.2014.12.048.

47. Fedotov, S.J.T.s. and technology, *Peculiarities of changes in elastic properties of titanium martensite.* 1973: p. 871-881.

48. Chou, K. and E.A. Marquis, *Oxygen effects on ω and α phase transformations in a metastable β Ti–Nb alloy.* Acta Materialia, 2019. **181**: p. 367-376 DOI: https://doi.org/10.1016/j.actamat.2019.09.049.

49. Niinomi, M., et al., *Influence of oxygen on omega phase stability in the Ti-29Nb-13Ta-4.6Zr alloy.* Scripta Materialia, 2016. **123**: p. 144-148 DOI: https://doi.org/10.1016/j.scriptamat.2016.06.027.

50. Tahara, M., et al., *Role of oxygen atoms in α″ martensite of Ti-20at.% Nb alloy.* Scripta Materialia, 2016. **112**: p. 15-18 DOI: https://doi.org/10.1016/j.scriptamat.2015.08.033.

51. Tahara, M., et al., *Lattice modulation and superelasticity in oxygen-added β-Ti alloys.* Acta Materialia, 2011. **59**(16): p. 6208-6218 DOI: https://doi.org/10.1016/j.actamat.2011.06.015.

52. Sass, S.L., *The ω phase in a Zr-25 at.% Ti alloy.* Acta Metallurgica, 1969. **17**(7): p. 813-820 DOI: https://doi.org/10.1016/0001-6160(69)90100-X.

53. Burgers, W.G., *On the process of transition of the cubic-body-centered modification into the hexagonal-close-packed modification of zirconium.* Physica, 1934. **1**(7): p. 561-586 DOI: https://doi.org/10.1016/S0031-8914(34)80244-3.

54. Rudy, E., *Ternary phase equilibria in transition metal-boron-carbon-silicon systems: part V. Compendium of phase diagram data*. 1969: Air Force Materials Laboratory USA.

55. Pearson, W.B., *A handbook of lattice spacings and structures of metals and alloys Vol. 2*. 1. ed ed. 1967, Oxford [u.a.]: Pergamon Press Oxford [u.a.].

56. Lu, Z.-W., D. Singh, and H. Krakauer, *Equilibrium properties of hcp titanium and zirconium.* Physical Review B, 1987. **36**(14): p. 7335-7341 DOI: 10.1103/PhysRevB.36.7335.

57. Roberge, R., *Lattice parameter of niobium between 4. 2 and 300K.* J. Less-Common Met.;(Switzerland), 1975. **40**(1).

58. Straumanis, M.E. and S. Zyszczynski, *Lattice parameters, thermal expansion coefficients and densities of Nb, and of solid solutions Nb–O and Nb–N–O and their defect structure.* Journal of Applied Crystallography, 1970. **3**(1): p. 1-6 DOI: https://doi.org/10.1107/S002188987000554X.

59. Barns, R.L., *Niobium: Lattice Parameter and Density.* Journal of Applied Physics, 2003. **39**(8): p. 4044-4045 DOI: 10.1063/1.1656912.

60. Kim, H., et al., *Martensitic transformation, shape memory effect and superelasticity of Ti–Nb binary alloys.* 2006. **54**(9): p. 2419-2429.

61. Bönisch, M., et al., *Composition-dependent magnitude of atomic shuffles in Ti–Nb martensites.* 2014. **47**(4): p. 1374-1379.

62. Demakov, S., et al., *A general model for the crystal structure of orthorhombic martensite in Ti alloys.* Acta Crystallographica Section B, 2021. **77**(5): p. 749-762 DOI: doi:10.1107/S2052520621007976.

63. Dobromyslov, A.V. and V.A. Elkin, *Martensitic transformation and metastable β-phase in binary titanium alloys with d-metals of 4–6 periods.* Scripta Materialia, 2001. **44**(6): p. 905-910 DOI: https://doi.org/10.1016/S1359-6462(00)00694-1.

64. Chai, Y.W., et al., *Self-accommodation in Ti–Nb shape memory alloys.* Acta Materialia, 2009. **57**(14): p. 4054-4064 DOI: https://doi.org/10.1016/j.actamat.2009.04.051.

65. Sun, B., et al., *Study on the deformation mechanism of the martensitic Ti–16Nb high temperature shape memory alloy.* Materials Science and Engineering: A, 2019. **742**: p. 590-596 DOI: https://doi.org/10.1016/j.msea.2018.07.051.

66. Banerjee, S., R. Tewari, and G.K. Dey, *Omega phase transformation – morphologies and mechanisms.* 2006. **97**(7): p. 963-977 DOI: doi:10.1515/ijmr-2006-0154.

67. Sikka, S.K., Y.K. Vohra, and R. Chidambaram, *Omega phase in materials.* Progress in Materials Science, 1982. **27**(3): p. 245-310 DOI: https://doi.org/10.1016/0079-6425(82)90002-0.

68. De Fontaine, D., N.E. Paton, and J.C. Williams, *The omega phase transformation in titanium alloys as an example of displacement controlled reactions.* Acta Metallurgica, 1971. **19**(11): p. 1153-1162 DOI: https://doi.org/10.1016/0001-6160(71)90047-2.

69. Devaraj, A., et al., *Three-dimensional morphology and composition of omega precipitates in a binary titanium–molybdenum alloy.* Scripta Materialia, 2009. **61**(7): p. 701-704 DOI: https://doi.org/10.1016/j.scriptamat.2009.06.006.

70. Devaraj, A., et al., *Experimental evidence of concurrent compositional and structural instabilities leading to ω precipitation in titanium–molybdenum alloys.* Acta Materialia, 2012. **60**(2): p. 596-609 DOI: https://doi.org/10.1016/j.actamat.2011.10.008.

71. Nag, S., et al., *Novel Mixed-Mode Phase Transition Involving a Composition-Dependent Displacive Component.* Physical Review Letters, 2011. **106**(24): p. 245701 DOI: 10.1103/PhysRevLett.106.245701.

72. Porter, D.A., K.E. Easterling, and M.Y. Sherif, *Phase transformations in metals and alloys*. Third edition ed. 2009, Boca Raton, FL: CRC Press Boca Raton, FL.

73. Jepson, K., A.R. Brown, and J. Gray, *EFFECT OF COOLING RATE ON THE BETA TRANSFORMATION IN TITANIUM--NIOBIUM AND TITANIUM--ALUMINIUM ALLOYS*. 1970, Royal Aircraft Establishment, Farnborough, Eng.

74. Bellen, P., K.H. Kumar, and P.J.I.J.o.M.R. Wollants, *Thermodynamic assessment of the Ni-Ti phase diagram.* 1996. **87**(12): p. 972-978.

75. Murray, J.L., *The Nb−Ti (Niobium-Titanium) system.* Bulletin of Alloy Phase Diagrams, 1981. **2**(1): p. 55-61 DOI: 10.1007/BF02873704.

76. Yan, J.-Y. and G.B. Olson, *Computational thermodynamics and kinetics of displacive transformations in titanium-based alloys.* Journal of Alloys and Compounds, 2016. **673**: p. 441-454 DOI: https://doi.org/10.1016/j.jallcom.2016.02.251.

77. Barriobero-Vila, P., et al., *Tracking the α" martensite decomposition during continuous heating of a Ti-6Al-6V-2Sn alloy.* Acta Materialia, 2017. **135**: p. 132-143 DOI: https://doi.org/10.1016/j.actamat.2017.06.018.

78. Ivasishin, O.M., et al., *Aging response of coarse- and fine-grained β titanium alloys.* Materials Science and Engineering: A, 2005. **405**(1): p. 296-305 DOI: https://doi.org/10.1016/j.msea.2005.06.027.

79. Ren, X., et al., *A comparative study of elastic constants of Ti–Ni-based alloys prior to martensitic transformation.* Materials Science and Engineering: A, 2001. **312**(1): p. 196-206 DOI: https://doi.org/10.1016/S0921-5093(00)01876-1.

80. Li, Q., Y. Onuki, and Q. Sun, *Tailoring thermal expansion of shape memory alloys through designed reorientation deformation.* Acta Materialia, 2021. **218**: p. 117201 DOI: https://doi.org/10.1016/j.actamat.2021.117201.

81. Ortín, J. and A. Planes, *Thermodynamic analysis of thermal measurements in thermoelastic martensitic transformations.* Acta Metallurgica, 1988. **36**(8): p. 1873-1889 DOI: https://doi.org/10.1016/0001-6160(88)90291-X.

82. Niessen, F. and E. Pereloma, *A Review of In Situ Observations of Deformation-Induced β ↔ α" Martensite Transformations in Metastable β Ti Alloys.* Advanced Engineering Materials, 2022. **24**(8): p. 2200281 DOI: https://doi.org/10.1002/adem.202200281.

83. Kolli, R.P., W.J. Joost, and S. Ankem, *Phase Stability and Stress-Induced Transformations in Beta Titanium Alloys.* JOM, 2015. **67**(6): p. 1273-1280 DOI: 10.1007/s11837-015-1411-y.

84. Li, C., et al., *Tuning the stress induced martensitic formation in titanium alloys by alloy design.* Journal of Materials Science, 2012. **47**(9): p. 4093-4100 DOI: 10.1007/s10853-012-6263-z.

85. Duerig, T.W., et al., *Formation and reversion of stress induced martensite in Ti-10V-2Fe-3Al.* Acta Metallurgica, 1982. **30**(12): p. 2161-2172 DOI: https://doi.org/10.1016/0001-6160(82)90137-7.

86. Davis, R., H.M. Flower, and D.R.F. West, *Martensitic transformations in Ti-Mo alloys.* Journal of Materials Science, 1979. **14**(3): p. 712-722 DOI: 10.1007/BF00772735.

87. Davis, R., H.M. Flower, and D.R.F. West, *The decomposition of Ti-Mo alloy martensites by nucleation and growth and spinodal mechanisms.* Acta Metallurgica, 1979. **27**(6): p. 1041-1052 DOI: https://doi.org/10.1016/0001-6160(79)90192-5.

88. Aeby-Gautier, E., et al., *Microstructural formation in Ti alloys: In-situ characterization of phase transformation kinetics.* JOM, 2007. **59**(1): p. 54-58 DOI: 10.1007/s11837-007-0011-x.

89. Settefrati, A., et al., *Low Temperature Transformations in β-Metastable Ti 5553 Titanium Alloy.* Materials Science Forum, 2013. **738-739**: p. 97-102 DOI: 10.4028/www.scientific.net/MSF.738-739.97.

90. Aeby-Gautier, E., et al., *Isothermal α″ formation in β metastable titanium alloys.* Journal of Alloys and Compounds, 2013. **577**: p. S439-S443 DOI: https://doi.org/10.1016/j.jallcom.2012.02.046.

91. Barriobero-Vila, P., et al., *Phase transformation kinetics during continuous heating of a β-quenched Ti–10V–2Fe–3Al alloy.* Journal of Materials Science, 2015. **50**(3): p. 1412-1426 DOI: 10.1007/s10853-014-8701-6.

92. Barriobero-Vila, P., et al., *Influence of phase transformation kinetics on the formation of α in a β-quenched Ti–5Al–5Mo–5V–3Cr–1Zr alloy.* Acta Materialia, 2015. **95**: p. 90-101 DOI: https://doi.org/10.1016/j.actamat.2015.05.008.

93. Ivasishin, O.M., et al., *Precipitation and recrystallization behavior of beta titanium alloys during continuous heat treatment.* Metallurgical and Materials Transactions A, 2003. **34**(1): p. 147-158 DOI: 10.1007/s11661-003-0216-8.

94. Gehring, D., J.A. Monroe, and I.J.S.M. Karaman, *Effects of composition on the mechanical properties and negative thermal expansion in martensitic TiNb alloys.* 2020. **178**: p. 351-355.

95. Khromova, L.P., et al., *Martensitic transformations, thermal expansion and mechanical properties of titanium-niobium alloys.* 2003. **112**: p. 1051-1054 DOI: 10.1051/jp4:20031062.

96. Kainuma, R., et al., *Invar-type effect induced by cold-rolling deformation in shape memory alloys.* 2002. **80**(23): p. 4348-4350.

97. Nakai, M., et al., *Anomalous Thermal Expansion of Cold-Rolled Ti-Nb-Ta-Zr Alloy.* MATERIALS TRANSACTIONS, 2009. **advpub**: p. 0901130641-0901130641 DOI: 10.2320/matertrans.MRP2008380.

98. Kuramoto, S., et al., *Elastic properties of Gum Metal.* Materials Science and Engineering: A, 2006. **442**(1): p. 454-457 DOI: https://doi.org/10.1016/j.msea.2005.12.089.

99. Saito, T., et al. *Multi Functional Titanium Alloy''GUM METAL''*. in *Materials Science Forum*. 2003. Trans Tech Publ.

100. Kim, H.Y., et al., *Nanodomain structure and its effect on abnormal thermal expansion behavior of a Ti–23Nb–2Zr–0.7Ta–1.2O alloy.* Acta Materialia, 2013. **61**(13): p. 4874-4886 DOI: https://doi.org/10.1016/j.actamat.2013.04.060.

101. Wang, Y., et al., *Strain glass transition in a multifunctional β-type Ti alloy.* Scientific Reports, 2014. **4**(1): p. 3995 DOI: 10.1038/srep03995.

102. Yang, Y., et al., *Stress-introduced α″ martensite and twinning in a multifunctional titanium alloy.* Scripta Materialia, 2008. **58**(1): p. 9-12 DOI: https://doi.org/10.1016/j.scriptamat.2007.09.010.

103. D'yakonova, N.B., I.V. Lyasotskii, and Y.L. Rodionov, *Orthorhombic martensite and the ω phase in quenched and deformed titanium alloys with 20–24 at % Nb.* Russian Metallurgy (Metally), 2007. **2007**(1): p. 51-58 DOI: 10.1134/S0036029507010107.

104. Gong, D.L., et al., *Tuning thermal expansion by a continuing atomic rearrangement mechanism in a multifunctional titanium alloy.* Journal of Materials Science & Technology, 2021. **80**: p. 234-243 DOI: https://doi.org/10.1016/j.jmst.2020.11.053.

105. Demakov, S., Y. Oleneva, and O.J.K.E. Oleneva, *The Influence of Molybdenum Equivalent on the Anisotropy of Thermal Expansion of Titanium Martensite Lattice.* 2019: p. 288–292-288–292.

106. Elmer, J.W., et al., *In situ observations of lattice expansion and transformation rates of α and β phases in Ti–6Al–4V.* Materials Science and Engineering: A, 2005. **391**(1): p. 104-113 DOI: https://doi.org/10.1016/j.msea.2004.08.084.

107. Souvatzis, P., O. Eriksson, and M.I. Katsnelson, *Anomalous Thermal Expansion in $\ensuremath{\alpha}$-Titanium.* Physical Review Letters, 2007. **99**(1): p. 015901 DOI: 10.1103/PhysRevLett.99.015901.

108. Zháňal, P., et al., *Transformation Pathway upon Heating of Metastable β Titanium Alloy Ti-15Mo Investigated by Neutron Diffraction.* Materials, 2019. **12**(21) DOI: 10.3390/ma12213570.

109. Pawar, R.R. and V.T. Deshpande, *The anisotropy of the thermal expansion of [alpha]-titanium.* Acta Crystallographica Section A, 1968. **24**(2): p. 316-317 DOI: doi:10.1107/S0567739468000525.

110. Spreadborough, J. and J.W. Christian, *The Measurement of the Lattice Expansions and Debye Temperatures of Titanium and Silver by X-ray Methods.* Proceedings of the Physical Society, 1959. **74**(5): p. 609-615 DOI: 10.1088/0370-1328/74/5/314.

111. Senkov, O.N., et al., *Effect of temperature and hydrogen concentration on the lattice parameter of beta titanium.* Materials Research Bulletin, 2001. **36**(7): p. 1431-1440 DOI: https://doi.org/10.1016/S0025-5408(01)00604-3.

112. Lopes, E.S.N., et al., *Effects of double aging heat treatment on the microstructure, Vickers hardness and elastic modulus of Ti–Nb alloys.* Materials Characterization, 2011. **62**(7): p. 673-680 DOI: https://doi.org/10.1016/j.matchar.2011.04.015.

113. Al-Zain, Y., et al., *Shape memory properties of Ti–Nb–Mo biomedical alloys.* Acta Materialia, 2010. **58**(12): p. 4212-4223 DOI: https://doi.org/10.1016/j.actamat.2010.04.013.

114. Nyayadhish, A., B. Maji, and M. Krishnan, *Martensitic Transformation, Omega Transformation and Pseudoelasticity in Aged Ti-24 at% Nb Alloy.* Proceedings of the International Conference on Martensitic Transformations, ICOMAT-08, 2009: p. 493-497 DOI: 10.1002/9781118803592.ch71.

115. Mantani, Y., M.J.M.S. Tajima, and E. A, *Phase transformation of quenched α ″martensite by aging in Ti–Nb alloys.* 2006. **438**: p. 315-319.

116. Guo, Y., et al., *On the mechanical properties of TiNb based alloys.* Journal of Alloys and Compounds, 2013. **571**: p. 25-30 DOI: https://doi.org/10.1016/j.jallcom.2013.03.192.

117. Settefrati, A., et al., *Precipitation in a near Beta Titanium Alloy on Ageing: Influence of Heating Rate and Chemical Composition of the Beta-Metastable Phase.* Solid State Phenomena, 2011. **172-174**: p. 760-765 DOI: 10.4028/www.scientific.net/SSP.172-174.760.

118. Zeng, G.-j., et al., *Detailed investigation on microstructure and strengthening contribution of Al-xCu-1.3Li-X alloy sheets.* Materials Characterization, 2023. **205**: p. 113278 DOI: https://doi.org/10.1016/j.matchar.2023.113278.

119. Liu, Y., et al., *Effect of Thermal Exposure on the Microstructure and Mechanical Properties of 2A97 Al-Li Alloy.* Journal of Materials Engineering and Performance, 2024 DOI: 10.1007/s11665-024-09707-w.

120. Brown, A.R.G., et al., *The Titanium–Niobium System.* Nature, 1964. **201**(4922): p. 914-915 DOI: 10.1038/201914a0.

121. Miyazaki, S. and H. Kim, *Basic characteristics of titanium–nickel (Ti–Ni)-based and titanium–niobium (Ti–Nb)-based alloys*, in *Shape Memory and Superelastic Alloys*. 2011, Elsevier. p. 15-42.

122. Hayama, A.O.F., et al., *Crystallographic texture evolution in Ti–35Nb alloy deformed by cold rolling.* Materials & Design, 2014. **60**: p. 653-660 DOI: https://doi.org/10.1016/j.matdes.2014.04.024.

123. Abdel-Hady, M. and M.J.S.M. Morinaga, *Controlling the thermal expansion of Ti alloys.* 2009. **61**(8): p. 825-827.

124. Touloukian, Y.S., et al., *Thermophysical properties of matter - the TPRC data series. Volume 12. Thermal expansion metallic elements and alloys. (Reannouncement). Data book.* 1975.

125. Tang, B., et al., *The ω phase transformation during the low temperature aging and low rate heating process of metastable β titanium alloys.* Materials Chemistry and Physics, 2020. **239**: p. 122125 DOI: https://doi.org/10.1016/j.matchemphys.2019.122125.

126. Sun, F., et al., *Strengthening strategy for a ductile metastable β-titanium alloy using low-temperature aging.* Materials Research Letters, 2017. **5**(8): p. 547-553 DOI: 10.1080/21663831.2017.1350211.

127. Zhao, X., et al., *Beta type Ti–Mo alloys with changeable Young's modulus for spinal fixation applications.* Acta Biomaterialia, 2012. **8**(5): p. 1990-1997 DOI: https://doi.org/10.1016/j.actbio.2012.02.004.

128. Sun, F., et al., *Investigation of early stage deformation mechanisms in a metastable β titanium alloy showing combined twinning-induced plasticity and transformation-induced plasticity effects.* Acta Materialia, 2013. **61**(17): p. 6406-6417 DOI: https://doi.org/10.1016/j.actamat.2013.07.019.

129. Champness, P.E. *Electron Diffraction in the Transmission Electron Microscope*. 2004.

130. Williams, D. and C. Carter, *Transmission Electron Microscopy: A Textbook for Materials Science*. Vol. III. 2009.

131. Li, T., et al., *New insights into the phase transformations to isothermal ω and ω-assisted α in near β-Ti alloys.* Acta Materialia, 2016. **106**: p. 353-366 DOI: https://doi.org/10.1016/j.actamat.2015.12.046.

132. Jones, N.G., et al., *β Phase decomposition in Ti–5Al–5Mo–5V–3Cr.* Acta Materialia, 2009. **57**(13): p. 3830-3839 DOI: https://doi.org/10.1016/j.actamat.2009.04.031.

133. Buenconsejo, P.J.S., et al., *Shape memory behavior of Ti–Ta and its potential as a high-temperature shape memory alloy.* Acta Materialia, 2009. **57**(4): p. 1068-1077 DOI: https://doi.org/10.1016/j.actamat.2008.10.041.

134. Liu, H., et al., *Athermal and deformation-induced ω-phase transformations in biomedical beta-type alloy Ti–9Cr–0.2O.* Acta Materialia, 2016. **106**: p. 162-170 DOI: https://doi.org/10.1016/j.actamat.2016.01.008.

135. Fultz, B. and J. Howe, *Transmission Electron Microscopy and Diffractometry of Materials*. 2002.

136. Kim, H.Y. and S. Miyazaki, *Martensitic Transformation and Superelastic Properties of Ti-Nb Base Alloys.* MATERIALS TRANSACTIONS, 2015. **56**(5): p. 625-634 DOI: 10.2320/matertrans.M2014454.

137. Elmay, W., et al., *Texture evolution of orthorhombic α″ titanium alloy investigated by in situ X-ray diffraction.* Materials Science and Engineering: A, 2017. **679**: p. 504-510 DOI: https://doi.org/10.1016/j.msea.2016.10.072.

138. Waseda, Y., E. Matsubara, and K. Shinoda, *X-Ray Diffraction Crystallography*. 2011.

139. Pilz, S., et al., *Influence of isothermal omega precipitation aging on deformation mechanisms and mechanical properties of a β-type Ti-Nb alloy.* Journal of Alloys and Compounds, 2023. **930**: p. 167309 DOI: https://doi.org/10.1016/j.jallcom.2022.167309.

140. Wang, W., et al., *Role of omega phase evolution in plastic deformation of twinning-induced plasticity β Ti–12V–2Fe–1Al alloy.* Materials & Design, 2020. **186**: p. 108282 DOI: https://doi.org/10.1016/j.matdes.2019.108282.

141. Song, B., et al., *Tuning the strength and ductility of near β titanium alloy Ti-5321 by ω and O′ intermediate phases via low-temperature aging.* Materials Science and Engineering: A, 2022. **855**: p. 143919 DOI: https://doi.org/10.1016/j.msea.2022.143919.

142. Prima, F., et al., *ω Precipitation in a Beta Metastable Titanium Alloy, Resistometric Study.* Materials Transactions, JIM, 2000. **41**(8): p. 1092-1097 DOI: 10.2320/matertrans1989.41.1092.

143. Prima, F., et al., *Control of omega phase volume fraction precipitated in a beta titanium alloy: Development of an experimental method.* Journal of Materials Science Letters, 2000. **19**(24): p. 2219-2221 DOI: 10.1023/A:1006708420478.

144. Qian, B., et al., *Mechanisms underlying enhanced strength-ductility combinations in TRIP/TWIP Ti-12Mo alloy engineered via isothermal omega precipitation.* Acta Materialia, 2023. **245**: p. 118619 DOI: https://doi.org/10.1016/j.actamat.2022.118619.

145. Li, S., M.-s. Choi, and T.-h. Nam, *Role of fine nano-scaled isothermal omega phase on the mechanical and superelastic properties of a high Zr-containing Ti–Zr–Nb–Sn shape memory alloy.* Materials Science and Engineering: A, 2020. **782**: p. 139278 DOI: https://doi.org/10.1016/j.msea.2020.139278.

146. Ren, L., et al., *Simultaneously enhanced strength and ductility in a metastable β-Ti alloy by stress-induced hierarchical twin structure.* Scripta Materialia, 2020. **184**: p. 6-11 DOI: https://doi.org/10.1016/j.scriptamat.2020.03.039.

147. Morinaga, M., et al., *Theoretical design of beta-type titanium alloys.* 1993: p. 217-224.

148. Morinaga, M., et al. *Theoretical design of titanium alloys*. in *Sixth World Conference on Titanium. III*. 1988.

149. Bignon, M., et al., *Modelling martensitic transformation in titanium alloys: The influence of temperature and deformation.* 2019. **7**: p. 100382.

150. Sinkler, W. and D.E. Luzzi, *An electron diffraction investigation of the diffuse ω structure in quenched Ti-3d transition metal alloys.* Acta Metallurgica et Materialia, 1994. **42**(4): p. 1249-1260 DOI: https://doi.org/10.1016/0956-7151(94)90141-4.

151. Hanada, S., H. Matsumoto, and S. Watanabe, *Mechanical compatibility of titanium implants in hard tissues.* International Congress Series, 2005. **1284**: p. 239-247 DOI: https://doi.org/10.1016/j.ics.2005.06.084.

152. Hanada, S., et al., *Composition dependence of Young's modulus in beta titanium binary alloys.* Materials Science Forum, 2003. **426-432**(4): p. 3103-3108 DOI: 10.4028/www.scientific.net/msf.426-432.3103.

153. Cho, K., et al., *Improvement in mechanical strength of low-cost β-type Ti–Mn alloys fabricated by metal injection molding through cold rolling.* Journal of Alloys and Compounds, 2016. **664**: p. 272-283 DOI: https://doi.org/10.1016/j.jallcom.2015.12.200.

154. Hanada, S. and O. Izumi, *Deformation behaviour of retained β phase inβ-eutectoid Ti-Cr alloys.* Journal of Materials Science, 1986. **21**(12): p. 4131-4139 DOI: 10.1007/BF01106518.

155. Sikka, S.K., Y.K. Vohra, and R. Chidambaram, *β-ω transformation under pressure ans stacking soliton model for diffuse omega phase in Ti V alloys.* Solid State Communications, 1982. **42**(3): p. 205-207 DOI: https://doi.org/10.1016/0038-1098(82)91005-5.

156. Dey, G.K., et al., *Formation of a shock deformation induced ω phase in Zr 20 Nb alloy.* Acta Materialia, 2004. **52**(18): p. 5243-5254 DOI: https://doi.org/10.1016/j.actamat.2004.07.008.

157. Shao, G. and P. Tsakiropoulos, *Prediction of ω phase formation in Ti–Al–X alloys.* Materials Science and Engineering: A, 2002. **329-331**: p. 914-919 DOI: https://doi.org/10.1016/S0921-5093(01)01576-3.

158. Salloom, R., et al., *First principles computation of composition dependent elastic constants of omega in titanium alloys: implications on mechanical behavior.* Scientific Reports, 2021. **11**(1): p. 12005 DOI: 10.1038/s41598-021-91594-5.

159. de Mello, M.G., et al., *Influence of heating rate and aging temperature on omega and alpha phase precipitation in Ti35Nb alloy.* Materials Characterization, 2018. **145**: p. 268-276 DOI: https://doi.org/10.1016/j.matchar.2018.08.035.

160. Zhang, F., et al., *Enhanced mechanical properties in metastable β titanium alloy via ω-assisted nucleation.* Materials Science and Engineering: A, 2022. **858**: p. 144082 DOI: https://doi.org/10.1016/j.msea.2022.144082.

161. Ohmori, Y., et al., *Effects of ω-phase precipitation on β→α, α′′ transformations in a metastable β titanium alloy.* Materials Science and Engineering: A, 2001. **312**(1): p. 182-188 DOI: https://doi.org/10.1016/S0921-5093(00)01891-8.

162. Mantani, Y. and M. Tajima, *Phase transformation of quenched α″ martensite by aging in Ti–Nb alloys.* Materials Science and Engineering: A, 2006. **438-440**: p. 315-319 DOI: https://doi.org/10.1016/j.msea.2006.02.180.

163. Ashby, M.F., *Overview No. 80: On the engineering properties of materials.* Acta Metallurgica, 1989. **37**(5): p. 1273-1293 DOI: https://doi.org/10.1016/0001-6160(89)90158-2.

164. Committee, A.H., *Properties and Selection: Nonferrous Alloys and Special-Purpose Materials*. 1990: ASM International.

165. Chen, F., et al., *Isothermal kinetics of β↔α transformation in Ti-55531 alloy influenced by phase composition and microstructure.* Materials & Design, 2017. **130**: p. 302-316 DOI: https://doi.org/10.1016/j.matdes.2017.05.078.

166. Hua, K., et al., *Phase precipitation behavior during isothermal deformation in β-quenched near beta titanium alloy Ti-7333.* Journal of Alloys and Compounds, 2016. **671**: p. 381-388 DOI: https://doi.org/10.1016/j.jallcom.2016.02.102.

167. Furuhara, T., et al., *Crystallography of grain boundary α precipitates in a β titanium alloy.* Metallurgical and Materials Transactions A, 1996. **27**(6): p. 1635-1646 DOI: 10.1007/BF02649821.

168. Su, J., et al., *Revealing the decomposition mechanisms of dislocations and metastable α' phase and their effects on mechanical properties in a Ti-6Al-4V alloy.* Journal of Materials Science & Technology, 2022. **107**: p. 136-148 DOI: https://doi.org/10.1016/j.jmst.2021.07.048.

169. Wang, Y., et al., *Formation and characteristics of bilamellar microstructure in Ti6242S titanium alloy under dual heat treatment.* Materials Characterization, 2022. **187**: p. 111835 DOI: https://doi.org/10.1016/j.matchar.2022.111835.

170. Zhang, Q., et al., *Texture and microstructure characterization in laser additive manufactured Ti–6Al–2Zr–2Sn–3Mo–1.5Cr–2Nb titanium alloy.* Materials & Design, 2015. **88**: p. 550-557 DOI: https://doi.org/10.1016/j.matdes.2015.09.053.

171. Huang, Q., et al., *Specific heat treatment of selective laser melted Ti–6Al–4V for biomedical applications.* Frontiers of Materials Science, 2015. **9**(4): p. 373-381 DOI: 10.1007/s11706-015-0315-7.

172. Liu, H., et al., *Enhancing the mechanical properties of electron beam welded TC17 titanium alloy joint by post-weld heat treatment.* Journal of Alloys and Compounds, 2019. **810**: p. 151937 DOI: https://doi.org/10.1016/j.jallcom.2019.151937.

173. Sun, Z., et al., *Morphology evolution and growth mechanism of the secondary Widmanstatten α phase in the TA15 Ti-alloy.* Materials Characterization, 2016. **118**: p. 167-174 DOI: https://doi.org/10.1016/j.matchar.2016.05.020.

174. Chen, W., et al., *Effect of prestrain on microstructure and mechanical behavior of aged Ti–10V–2Fe–3Al alloy.* Journal of Materials Research, 2009. **24**(9): p. 2899-2908 DOI: 10.1557/jmr.2009.0332.

175. Miranda, M.G.M., et al., *Phase separation in ${\mathrm{Cu}}_{90}{\mathrm{Co}}_{10}$ high-magnetoresistance materials.* Physical Review B, 2003. **68**(1): p. 014434 DOI: 10.1103/PhysRevB.68.014434.

176. Vidyasagar, A., S. Krödel, and D.M. Kochmann, *Microstructural patterns with tunable mechanical anisotropy obtained by simulating anisotropic spinodal decomposition.* 2018. **474**(2218): p. 20180535 DOI: doi:10.1098/rspa.2018.0535.

177. Thoemmes, A., et al., *Microstructure and lattice parameters of suction-cast Ti–Nb alloys in a wide range of Nb concentrations.* Materials Science and Engineering: A, 2021. **818**: p. 141378 DOI: https://doi.org/10.1016/j.msea.2021.141378.

178. Bönisch, M., et al., *Tailoring the Bain strain of martensitic transformations in TiNb alloys by controlling the Nb content.* 2016. **85**: p. 190-202.

179. Yan, J.-Y. and G.J.C. Olson, *Molar volumes of bcc, hcp, and orthorhombic Ti-base solid solutions at room temperature.* 2016. **52**: p. 152-158.

180. Lu, Z.K. and G.J. Weng, *Martensitic transformation and stress-strain relations of shape-memory alloys.* Journal of the Mechanics and Physics of Solids, 1997. **45**(11): p. 1905-1928 DOI: https://doi.org/10.1016/S0022-5096(97)00022-7.

181. Pontau, A.E. and D. Lazarus, *Diffusion of titanium and niobium in bcc Ti-Nb alloys.* Physical Review B, 1979. **19**(8): p. 4027-4037 DOI: 10.1103/PhysRevB.19.4027.

182. Mehrer, H. *Diffusion in solids : fundamentals, methods, materials, diffusion-controlled processes*. 2007.

183. Lin, H.C. and S.K. Wu, *Determination of heat of transformation in a cold-rolled martensitic tini alloy.* Metallurgical Transactions A, 1993. **24**(2): p. 293-299 DOI: 10.1007/BF02657316.

184. Niranjani, V.L., K.C. Hari Kumar, and V. Subramanya Sarma, *Development of high strength Al–Mg–Si AA6061 alloy through cold rolling and ageing.* Materials Science and Engineering: A, 2009. **515**(1): p. 169-174 DOI: https://doi.org/10.1016/j.msea.2009.03.077.

185. Li, L., et al., *Microstructure evolution during cold rolling in a nanocrystalline Ni–Fe alloy determined by synchrotron X-ray diffraction.* Acta Materialia, 2009. **57**(17): p. 4988-5000 DOI: https://doi.org/10.1016/j.actamat.2009.07.002.

186. Vlach, M., et al., *Phase transformations in isochronally annealed mould-cast and cold-rolled Al–Sc–Zr-based alloy.* Journal of Alloys and Compounds, 2010. **492**(1): p. 143-148 DOI: https://doi.org/10.1016/j.jallcom.2009.11.126.

187. Mei, Y., et al., *Effects of cold rolling on the precipitation kinetics and the morphology evolution of intermediate phases in Inconel 718 alloy.* Journal of Alloys and Compounds, 2015. **649**: p. 949-960 DOI: https://doi.org/10.1016/j.jallcom.2015.07.149.

188. Wu, Y.-p., et al., *Precipitation kinetics of 2519A aluminum alloy based on aging curves and DSC analysis.* Transactions of Nonferrous Metals Society of China, 2014. **24**(10): p. 3076-3083 DOI: https://doi.org/10.1016/S1003-6326(14)63445-2.

189. Koul, M.K. and J.F. Breedis, *Omega phase embrittlement in aged Ti-V.* Metallurgical Transactions, 1970. **1**(5): p. 1451-1452 DOI: 10.1007/BF02900269.

190. Chen, W., et al., *Origin of the ductile-to-brittle transition of metastable β-titanium alloys: Self-hardening of ω-precipitates.* Acta Materialia, 2019. **170**: p. 187-204 DOI: https://doi.org/10.1016/j.actamat.2019.03.034.

191. Williams, J.C., B.S. Hickman, and H.L. Marcus, *The effect of omega phase on the mechanical properties of titanium alloys.* Metallurgical Transactions, 1971. **2**(7): p. 1913-1919 DOI: 10.1007/BF02913423.

192. Lin, D.J., J.H. Chern Lin, and C.P. Ju, *Effect of omega phase on deformation behavior of Ti–7.5Mo–xFe alloys.* Materials Chemistry and Physics, 2002. **76**(2): p. 191-197 DOI: https://doi.org/10.1016/S0254-0584(01)00511-9.

193. Bowen, A.W., *Omega phase embrittlement in aged Ti-15%Mo.* Scripta Metallurgica, 1971. **5**(8): p. 709-715 DOI: https://doi.org/10.1016/0036-9748(71)90258-4.

194. Gibbs, G.B., D. Graham, and D.H. Tomlin, *Diffusion in titanium and titanium—niobium alloys.* The Philosophical Magazine: A Journal of Theoretical Experimental and Applied Physics, 1963. **8**(92): p. 1269-1282 DOI: 10.1080/14786436308207292.